# A Combined Optical Current and Temperature Sensor for Remote Monitoring of Sub-sea Electrical Plant

**Deborah Reilly**

**BEng**

Submitted for the Degree

of

Master of Philosophy

Institute for Energy and Environment

Department of Electronic and Electrical Engineering

University of Strathclyde

Glasgow G1 1XW

UK

October 2010

## Abstract

At present, within the oil and gas industry, significant efforts are being made to offset declining production levels from depleted offshore reservoirs by exploiting satellite fields. Due to the characteristics of many sub-sea fields, reserves are located many kilometres from existing infrastructure in water depths exceeding 1,000 metres. It is envisaged that extended step-out Electrical Submersible Pump (ESP) systems will be commissioned to aid this process and that it will be feasible to consider schemes in the region of tens of kilometres.

At these distances, new technical problems are emerging due to adverse electrical and mechanical operating conditions, which may cause equipment deterioration and increased maintenance with unexpected downtime and production disturbances. An on-line optical monitoring system would enable critical performance data to be acquired in real time, and optically transmitted to a novel interrogation system where model-based predictive monitoring can be carried out to eliminate unscheduled downtime, minimise costs and optimise ESP lifetime.

The research work presented in this thesis is related specifically to the design, construction and experimental evaluation of a novel optical current sensor (OCS), developed to form part of a remotely interrogated, fibre optic based, condition monitoring system comprising current, voltage and temperature sensors.

This thesis describes one possible OCS solution capable of measuring both ac current and temperature using a single fibre Bragg grating (FBG). The device consists of a magnetically biased magnetostrictive alloy bonded to an FBG. The magnetic field generated by the current in a specially designed coil produces internal strains in the magnetostrictive alloy which can be detected by the FBG. The temperature at the sensing point is determined through averaging of the sensor output signal. A prototype sensor has been constructed capable of measuring ac current up to approximately 1 A (zero-to-peak) while simultaneously measuring temperature up to 70°C.

# Contents

## List of Figures

## Glossary of Terms

| | |
|---|---|
| A | Ampere |
| ac | Alternating Current |
| AFC | Antiferromagnetically-coupled |
| CT | Current Transformer |
| DAC | Data Acquisition Card |
| dc | Direct Current |
| Dy | Dysprosium |
| EDFA | Erbium Doped Fibre Amplifier |
| EFPI | Extrinsic Fabry Perot Interferometer |
| EMI | Electromagnetic Interference |
| ESP | Electrical Submersible Pump |
| FBG | Fibre Bragg Grating |
| FC/APC | Fibre Connecter / Angle Polished Contact |
| Fe | Iron |
| FORC | First-order reversal curve analysis |
| FP-TF | Fabry–Perot Tunable Filter |
| GA | Generic algorithms |
| Ho | Holmium |
| LED | Light Emitting Diode |
| NOL | Naval Ordinance Laboratory |
| OCS | Optical Current Sensor |
| Oe | Oersted |
| PC | Personal Computer |
| PCI | Peripheral Component Interconnect |
| ppm | Parts per Million |
| PSO | Particle swarm optimisation |
| PVC | Polyvinylchloride |
| PXI | PCI eXtentions for Instrumentation |
| RF | Radio Frequency |
| RMS | Root Mean Square |

| | |
|---|---|
| SFS | Super Fluorescent Source |
| SWG | Standard Wire Gauge |
| Tb | Terbium |
| TEC | Thermo-Electric Cooler |
| UV | Ultra Violet |
| V | Volt |
| WDM | Wavelength Division Multiplexing |
| YIG | Yttrium Iron Garnet |

## Acknowledgements

I would like to give special thanks to Professor James McDonald for providing me with the opportunity to work in such a great research group and for his support throughout my time in the group.

My thanks and appreciation go to my supervisor Dr Pawel Niewczas for his guidance during my research and for his patience during the time it took me to complete my research and write this thesis.

I would like to show my gratitude to the other members of the Advanced Sensors Team, Dr Grzegorz Fusiek, Dr Lukasz Dziuda and especially Dr Andrew Willshire, my dear friend Drew. It was a pleasure working with you.

My thanks go to the many colleagues in the Institute for Energy and Environment who helped and encouraged me. I am grateful to have met several life-long friends during my time within the group, in particular Gordon Jahn and his wife Jacquie for inviting me to many great chilli parties.

I would like to convey my thanks to Robin Cochrane and the other members of the workshop for their assistance during the build of the prototype sensor components.

I would like to thank my husband and best friend Ernest van Pomeren, for all his support while I was writing this thesis.

I owe my deepest gratitude to my Mother Catherine Reilly for her constant support and encouragement throughout my whole life. This thesis is dedicated to you.

Ultimately, I thank God for the many wonderful blessings and opportunities that He has provided me with throughout my life.

# 1 Introduction

As main offshore reservoirs become depleted, operators are increasingly considering the exploitation of satellite fields within the vicinity of existing oil platforms. Production rates and well down times are key factors used to determine the economic feasibility of continued operation in marginal offshore subsea fields. As production rates decline, it becomes necessary to explore reliable artificial lift systems as a means to create additional production and maintain well viability. Therefore the production from these satellite fields is critically dependent upon ESPs at large step-out distances. ESPs of 15 km step-out have already been commissioned and it is envisaged that it will be feasible to consider schemes in the region of 30 km [1].

The projected use of higher rated ESPs over longer distances has presented designers with a number of potential problems that do not exist to the same extent with schemes in current use. Capital investment and maintenance costs significantly increase with ESP rating and extended step-out distances. As a result, the need to monitor electrical plant remotely, over several tens of kilometres, has emerged as operators of downhole ESPs and other electrical sub-sea systems for oil extraction, seek to apply improved methods of control to maximise production and reduce plant failure rates.

In order to monitor the ongoing state of the plant, as well as anticipate and manage anomalous operating conditions, operators require the capability to monitor, measure and analyse key attributes, to control sub-sea processes.

In particular, it would be desirable to measure voltage and current waveforms at the ESP motor terminals to determine the following principal phenomenon:

- Phase voltage and current integrals
- Power factor
- Current and voltage harmonic levels.

This information can then be used by the motor controller to make appropriate corrections to improve the power quality at the motor terminals and extend its life.

This research was conducted as part of a Scottish Enterprise Proof of Concept project. The technical challenge was to develop a novel, distributed optical measurement system containing current, voltage and temperature sensors. The measurement system was required to be suitable for integration onto ESPs, allowing critical performance data to be acquired and optically transmitted to an interrogation system where model-based, predictive monitoring can be conducted.

The collection of such information would enable operators to make proactive operational decisions based on factual analysis of validated data. In many cases, enabling operators to monitor plant and schedule maintenance to prevent unexpected failures and thus unplanned downtime.

This thesis explains in detail the work carried out to design and build a prototype optical current sensor as part of the Proof of Concept project. The work has focused on one possible sensor solution, with attention given to the requirement for it to form part of a monitoring system comprising three current sensors, three voltage sensors and two temperature sensors. Consideration was also given to its intend location within an ESP.

## 1.1 Motivation for Research

A fundamental requirement for safe and efficient operation of ESPs is the collection of performance data and in particular the measurement of electric current and temperature. Whereby enhancing the controllability of the system by optimising the operation through the supply of real time data, providing advanced warning of thermal and electrical failures and to continually supply real time condition monitoring data.

Current measurement plays an important role in the protection and control of electrical systems and is required in numerous industries. The availability of current and temperature data in this application would enable operators to monitor ESPs and to schedule shutdown of the pumps when required, in order to prevent unplanned downtimes or even ESP failure.

The conventional method of current measurement is by the instrument current transformer (CT) using copper wire windings and an iron core. Although accurate and reliable in most cases, there are many disadvantages associated with the conventional CT. These include the following:

- They are bulky and heavy; in fact those used for current measurement in high voltage applications can weigh as much as 2,000 kg due to the added insulation.
- These are prone to electromagnetic interference.
- Many applications require smaller and lighter transducers.
- Difficult to implement when current measurement over extended distances is required, especially in sub-sea applications.

Sensors used for downhole monitoring applications in the oil and gas industry are subjected to extremely hostile environments. Conventional current monitoring methods are not always appropriate for use in such harsh operating conditions, specifically due to the difficulty in transmitting the signal from the sensor back to the surface, heat and Electromagnetic Interference (EMI). To date, the industry has relied largely on "wireline" retrievable sensors that are lowered into the well to make measurements of key parameters. Such wireline monitoring provides a "snapshot" of the well/reservoir, and is usually repeated months or years apart [2].

Although fibre optic links are possible, and are now routinely integrated with "umbilical" power cables, they require electrically powered optoelectronic transmitters. This requirement presents a difficult technological problem, especially for electrical plant operating in downhole conditions.

Alterative methods of measuring current have been widely researched over the years and a promising alternative to conventional CTs involves the use of optical fibre based sensors. Optical fibre technology can now be found in a variety of applications, including sensing and measuring. They offer many advantages over the conventional CT, which make them particularly well suited for use in electrical current measurement for application within the oil and gas industry.

## 1.2 Research Context

Due to declining production levels from depleted offshore reservoirs, new generation ESPs are being used to extract the maximum available oil from satellite fields. This has resulted in increasing step-out lengths of ESP systems.

These ESP systems consist of a number of components that turn a staged series of centrifugal pumps to increase the pressure of the well fluid thus pushing it to the surface. The energy required to turn the pump is obtained from a medium voltage, typically 3 – 5 kV, alternating current source to drive a specially designed motor capable of operating at high temperature of up to 150ºC and high pressure of up to 5,000 psi (34 MPa), from deep wells of up to 12,000 feet (3.7 km) deep. These ESPs typically have power ratings in the range of 7.5 kW – 560 kW with some of the more demanding sites having higher energy requirements of up to 750 kW [3].

As these distances increase it is becoming more and more difficult to obtain real time performance data from the pumps for monitoring purposes, resulting in unscheduled downtime and even unpredicted ESP failure. The repair and replacement of such failures including sea transportation, equipment recovery and refit can be extremely costly, not to mention the lost production time.

The introduction of improved or novel monitoring techniques, tailored to the industry's needs, would enable performance data to be collected and facilitate planned downtimes in order to prolong ESP life time and prevent expensive unexpected failures.

## 1.3 Research Considerations

Although the purpose of this research was to demonstrate the sensor concept, where possible consideration was given to its intended location on an ESP. The following points were taken into consideration during the design and development of the prototype sensor:

- ESPs operate in salt water and other corrosive fluids so the sensor package will need to withstand highly corrosive environments.
- The operating temperature of ESPs can reach 150ºC due to the down well conditions, so the sensor must be capable of operating in high temperature environments. Temperature compensation may be required.
- Even in the relatively shallow depths of the North Sea, around 300 feet (95 metres) average [4], the pressure at the seabed is high. Pressure in the ocean increases by one atmosphere (14.7 psi) every 33 feet (10 metres) of descent [5]. Therefore pressure compensation may also be required.
- The current ratings for ESPs are normally between 100 and 1000 A ac. It was decided to build a prototype sensor to experimentally demonstrate the measurement of scaled down current in the laboratory.
- Space is restricted on ESPs. Therefore the sensor should be lightweight, compact and minimally invasive.
- The sensor will ideally be of simple construction to enable mass production of sensors with similar characteristics.
- The distance between the sensor and the measuring equipment can be up to 25 kilometres due to the distance between ESPs and the oil platforms. This may cause attenuation problems, and slight effects from time delay.

## 1.4 Principle Research Contributions

In terms of the novelty of the research undertaken, the main contribution include:

- The laboratory demonstration of an optical sensor capable of simultaneously measuring alternating current and temperature at the sensor head, using a single FBG.
- The development of a novel sensor packaging concept; enabling investigation of the effects of prestress on the sensor output characteristics.

## 1.5 Thesis Outline

The remainder of this thesis has been divided into ten principle chapters:

Chapter 2 provides a background to the research that has been undertaken; it briefly discusses optical fibre sensors and the measurands they have proven to measure and briefly reviews previous research into optical currents sensors.

Potential sensor solutions are discussed in chapter 3 along with the proposed sensor technology.

Chapter 4 concentrates on FBGs: their fabrication, operation, advantages and disadvantages.

In Chapter 5, an overview of magnetostriction and magnetostrictive materials is provided with emphasis on the specific material used in the sensor construction.

Chapter 6 gives an overview of hysteresis and other sensor nonlinearites. Possible solutions to these anomalies are also proposed and methods of correcting the sensor output are suggested.

Chapter 7 presents the sensor design along with details of the fabrication process and discusses the advantages and limitations of the system.

Chapter 8 is concerned with prestress and its effect on the sensor. A possible prestress housing design is also proposed.

Chapter 9 details the experimental set-up including details of the interrogation system and experimental coil design

Chapter 10 reports on the extensive experimental work carried out during the development of the prototype optical current sensor. Work carried out on the proposed signal processing method is also discussed.

Finally, in chapter eleven, conclusions are drawn from the work presented and future work is detailed.

## 1.6 Associated Publications

The following publications have arisen from the research detailed in this thesis:

- Reilly, D., Willshire, A.J., Fusiek, G., Niewczas, P., and McDonald, J. R., "A Fibre Bragg Grating Based Sensor for Simultaneous AC Current and Temperature Measurement", IEEE Sensors Conference 2005, Austria.
- Reilly, D., Willshire, A.J., Fusiek, G., Niewczas, P., and McDonald, J. R., "A Fibre Bragg Grating Based Sensor for Simultaneous AC Current and Temeperature Measurements, IEEE Sensors Journal, November 2006.

## 1.7 Chapter References


[1] "Development of an On-Line Optical Monitoring System for Subsea Electrical Submersible Pumps", Internal Report, Advanced Sensors Team, Institute for Energy and Environment, University of Strathclyde.

[2] Kersey, A.D., "Optical Fiber Sensors for Permanent Downwell Monitoring Applications in the Oil and Gas Industry", IEICE Transactions on Electronics, Vol. E83-C, No.3, March 2000, pp.400-404.

[3] Takacs, G., "Electrical Submersible Pumps Manual: Design, Operations, and Maintenance," Gulf Professional Publishing, 2009.

[4] Oilfield Publications Limited, "The North Sea Field Development Guide," 7th Edition, PennWell Books, 2000.

[5] Naval Meteorology and Oceanography Command Website - www.navmetoccom.navy.mil/pao/Educate/OceanTalk2/indexseawater.htm

# 2 Background and Related Work

The aim of this chapter is to provide a brief overview of available optical fibre sensor technologies and the measurands they have been proven to measure, describing their advantages over conventional sensors.

For greater detail, the reader is directed to references [1 - 5].

## 2.1 Optical Fibre Sensors

Following the advent of the Laser and the development of optical fibres, optical fibre sensors have been the subject of considerable research and development activity. Optical fibre sensors are based on the interaction of the measurand of interest with light in the sensor. This occurs in such a way that modification of one of the properties of the optical signal occurs in proportion to the measurand.

Past research has resulted in the design and realisation of optical fibre sensors for the measurement of a wide range of measurands including: temperature, strain, vibration, humidity, viscosity, linear and angular position, rotation, acceleration, electric- and magnetic-fields, pressure, chemical measurements and a host of other sensor applications [4].

The use of optical fibre sensors in remote sub-sea applications can potentially overcome the difficulty in obtaining accurate data for use in condition monitoring of ESPs. They offer a number of advantages over conventional sensor technologies. These include:

- Electromagnetic immunity. Spurious electromagnetic fields from, for example, electrical plant or radio frequency (RF) communications do not affect the propagation of light in the fibre and therefore do not affect the quality of the measurand data.

- Unprecedented speed and bandwidth, due to the fibre optic transmission medium.

- An intrinsically safe mode of operation. Some environments are unsuitable for the deployment of electrical sensor technology. As silica is an insulator there is no risk of sparking from an optical fibre sensor. Especially in areas where electrical discharges could be hazardous. Tracking, and erosion, however, can arise as a result of prolonged exposure to the combined action of strong electrical fields with dust, moisture and other external contaminants.

- Chemically inert nature. Silica does not oxidise or otherwise corrode except in the most caustic environments.

- Low power requirements.

- Ability to be multiplexed. Many intrinsic and extrinsic sensors may be multiplexed, offering the possibility of a large number of sensors being supported by a single optical fibre [5].

- Small size and lightweight. Some optical fibre sensors (e.g., FBGs) are constructed within the fibre itself. Other Extrinsic Fabry Perot Interferometers (EFPIs) are formed using a capillary tube or similar. The dimensions of these sensors are greater than the dimensions of the fibre, yet they are still reasonably small and light.

- Ability to interface with a wide range of measurands.

- Increased dynamic range and resolution when compared to conventional sensing technologies.

There are also a number of disadvantages associated with optical sensors. These include:

- Susceptibility to physical damage especially during construction and installation.

- Sensitivity to external influences including, pressure, vibration and bending.

## 2.2 Optical Sensing Techniques

Optical fibre sensors can be loosely divided into two groups, intrinsic or all fibre sensors and extrinsic or hybrid fibre optic sensors. In intrinsic sensors the fibre itself, or a portion of the fibre, is the sensor and the light beam propagating through the optical fibre is changed (modulated) by the effects of the measurand, either directly or indirectly. Extrinsic sensors, however, use the optical fibre to transmit the optical signal between the sensor head and the processor unit, in some cases the input optical fibre also acts as the output fibre, with the transducer being external to the fibre.

Optical fibre sensors can be further categorised into the techniques upon which they are based. Since light is characterised by intensity (amplitude), polarisation, phase and frequency, these are the four principle means by which a change in measurand can be encoded by an optical sensor [6]:

- Intensity based sensors depend on the measurand affecting the magnitude of the optical signal. Data is gathered by relating changes in the monitored intensity to the measurand. The main disadvantage in using these types of sensors is that fluctuations in the source intensity or changes in system attenuation, such as fibre bending, could be wrongly seen as changes in the measurand.

- Polarisation based sensors alter the polarisation state of the light. In such sensors data is inferred by comparing the initial polarisation state to that of the returned light. However, these sensors require the use of bulk optic components (polarisers and analysers) in order to create the initial polarisation state, and to analyse the returned light. These components are particularly susceptible to vibration and temperature extremes and are therefore not suitable for use in hostile environments.

- The phase of the light returning from a sensor can be influenced by the measurand. This change can be measured using interferometric demodulation techniques, with respect to a reference signal and related back to the measurand. However, phase changes of more than $2\pi$ radians have been found to be ambiguous unless the fringes are counted. Also, if an interruption was to occur in the signal, an accurate measurement might not be possible until the system was recalibrated. Recent literature [7 - 9] reports on a potential method of overcoming this effect.

- Wavelength encoded sensors operate through the measurand altering the spectrum of light returned from the sensor. By analysing changes in this spectrum it is possible to obtain measurand data. These types of sensors are immune to optical signal attenuation modulation and source fluctuations. In addition, the risk of recalibration being required is minimal if the sensors are correctly specified. For these reasons, it was elected to use wavelength-encoded sensors exclusively in the development of the optical current sensor.

Regardless of which method of modulation is utilised, detection is essentially based on intensity variations of the light returning from the sensor.

This chapter is not intended to be a comprehensive description of optical fibre sensors due to the very wide range of possible devices. These can be found in many textbooks [1, 2, 3, 5] available on these subjects.

## 2.3 Optical Current Sensors

An optical current sensor can, in general, be defined as consisting of an optical sensing element which measures the integral of the magnetic field along a closed (or nearly closed) optical loop around the current to be measured, and an optical fibre link which connects the sensing element with an optoelectronic control and processing unit, which is used to launch a light beam into the optical fibre and detect and decode the modulated optical signal, collected from the fibre [6].

Depending on the current sensing mechanisms involved and the sensing material used, optical current sensors (OCSs) may be categorised into four main groups [10]:

- OCSs employing optical fibres as their sensing element
- OCSs using bulk glass to sense the current
- OCSs using electro-optic hybrid sensing devices
- OCSs using magnetic field sensing devices

In recent years, considerable effort has been devoted to the exploitation of different types of optical current sensing mechanisms such as Faraday effect and magnetostriction. Research has also been conducted into the improvement of various materials utilised in these sensors including optical fibres, bulk-glass and yttrium iron garnet (YIG). These developments have aided in the implementation of high performance OCSs, which can be used to replace the CT.

Historically, most have been based on the Faraday magneto-optic effect. In such sensors, classified as polarimetric sensors, magnetically induced changes in the polarisation of light are analysed in order to derive the current. Polarimetric sensors based upon Faraday rotation have been described in the literature [11]. These devices are not suitable for this application as they are bulky and vulnerable to external influences, such as vibration and temperature variations, which are especially exacerbated when extended length fibre leads are used.

Several sensor designs based upon an FBG bonded to a piece of magnetostrictive material have been reported on [12], [13]. This method has numerous advantages over the polarimetric sensors, including smaller size, insensitivity to source intensity fluctuations and greater multiplexing potential. However, these devices also require temperature compensation. This can be achieved using a separate FBG isolated from the current sensing element, which can be used to provide a reference. A method using an additional piece of non-magnetostrictive sensing material with a similar coefficient of thermal expansion has also been demonstrated with two FBGs [12] as

well as a method using a single FBG [13]. The principle disadvantage in using a second FBG is the additional cost and bandwidth requirements. The method of [13] requires a split in the FBG spectrum to be measured, which for small currents might be difficult to discern.

## 2.4 Chapter References


[1] Culshaw, B., Dakin, J., "Optical Fiber Sensors," Vol. 3, Artech House, 1996.

[2] Grattan, K.T.V., Meggitt, B.T., "Optical Fiber Sensor Technology," Vol. 2, Chapman & Hall, 1998.

[3] Keiser, G., "Optical Fiber Communications", Second Edition, 1991, McGraw-Hill.

[4] Udd, E., "Review Article: An overview of fibre-optic sensors", Review of Scientific Instruments, Vol. 66, No. 8, August 1995, American Institute of Physics, pp4015-4030.

[5] Kersey, A. D., "In Fiber Optic Sensors: An Introduction for Engineers and Scientists", edited by E. Udd (Wiley, New York, 1991).

[6] Niewczas, P., "Implementation of a Faraday Effect Based Optical Current Transducer using Digital Signal Processing Techniques", PhD Thesis, University of Strathclyde, Department of Electronic and Electrical Engineering, June 2000.

[7] Todd, M.D., Johnson, G.A., Chang, C.C., "Passive, light intensity-independent interferometric method for fibre Bragg grating interrogation," Electronic Letters, Vol. 35, No. 22, October 1999, pp.1970-1971.

[8] Todd, M.D., Johnson, G.A., Althouse, B.L., "A novel Bragg grating sensor interrogation system utilizing a scanning filter, a Mach-Zehnder interferometer and a 3 x 3 coupler," Measurement Science and Technology, Vol. 12, No. 7, Institute of Physics Publishing, 2001, pp771-777.

[9] Todd, M.D., Seaver, M., Bucholtz, F.,"Improved, operationally-passive interferometric demodulation method using 3 x 3 coupler," Electronic Letters, Vol. 38, No.15, July 2002, pp.784-786.

[10] Ning, Y. N., Wang, Z. P., Palmer, A. W., Grattan, K. T. V., and Jackson, D. A., "Review Article: Recent Progress in Optical Current Sensing Techniques", Review of Scientific Instruments, Vol. 66, No. 5, American Institute of Physics, 1995, pp3097-3111.

[11] Madden, W.I., Michie, W.C., Cruden, A., Niewczas, P., McDonald, J.R., Andonovic, I., "Temperature Compensation for Optical Current Sensors," Optical Engineering, Vol. 38, Issue 10, October 1999, pp.1699-2374.

[12] Mora, J., Diez, A., Cruz, J.L., Andres, M.V., "A Magnetostrictive Sensor Interrogated by Fiber Gratings for DC-Current and Temperature Discrimination," IEEE Photonics Technology Letters, Vol.12, Issue 12, December 2000, pp.1680-1682.

[13] Chiang, K.S., Kancheti, R., Rastogi, V., "Temperature-Compensated Fiber Bragg Grating Based Magnetostrictive Sensor for dc and ac Currents," Optical Engineering, Vol. 42, Issue 7, July 2003, pp1906-1909.

# 3 Potential Sensor Solutions

This chapter will provide a basic overview of the two main sensor solutions that were considered for remote current measurement in this application and the proposed sensor technology will be selected.

## 3.1 Fibre Optic Current Sensors Based on the Faraday Effect

For almost a century it has been normal practice to provide a current measurement signal isolated from high voltage by measuring the magnetic field associated with the current. The current is given by the integral of the field around a closed path enclosing the current carrying conductor. The spatial distribution of the magnetic field depends on the location of the return path of the current, and can be affected by other nearby circuits. However, provided the integration is carried out over a closed path, the actual shape of the path is immaterial [1], [2]. Ampere's Law can be written:

$$I = \oint Hdl \tag{1}$$

where:

I is the current;

H is the magnetic field;

dl is the path element.

While it is not the only way to convert current into an optical effect, the Faraday effect or magneto-optic effect is used in most optical sensors.

If the linearly polarised light passes through a material that preserves the phase but couples energy between the two linearly polarised orthogonal components, it will still be linearly polarised when it emerges. The plane of polarisation will have rotated. This property is known as optical activity [1], [2].

The Faraday effect is a modulated optical activity: a rotation of the plane of polarisation of linearly polarised light through a magnetic field through the material. The magnitude of this effect is expressed by the Verdet constant. An optical current transducer based on this effect functions by passing linearly polarised light through a magneto-optic material. The plane of polarisation of linearly polarised light is rotated in proportion to the field and the path length [1], [2]. This can be expressed by:

$$\theta = \mu V \int_0^L H dL = \text{VBL} \tag{2}$$

where:

θ is the rotation of the polarisation azimuth;

μ is the relative permeability;

V is the Verdet constant;

B is the magnetic induction;

H and *dl* are the components in the direction of propagation.

In practise, the Verdet constant varies with wavelength, and is temperature dependent. These effects must be quantified and compensated for in a practical OCS [1], [2].

The Faraday effect is non-reciprocal. If the plane polarised light is rotated through an angle θ in one passage through the medium, then returning the light in the reverse direction will result in a further θ rotation, so that on a double passage the total rotation will be 2θ rather than zero as is the case of optical activity. This property could potentially be utilised to implement vibration compensation [1].

The linearly polarised light is obtained by passing the arbitrarily oriented light through a polariser. The measurement is made by examining the linearly polarised light emerging from the sensor by means of a second polariser (termed an analyser).

If there is an angle α between the transmission axes of the polariser and the analyser, the light power $P_{det}$ at the detector is given in terms of the input power $P_{in}$ by

$$P_{\det} = P_{in}(\cos\alpha)^2 = \frac{1}{2}P_{in}(1+\cos(2\alpha)) \quad (3)$$

assuming there is no insertion loss. The representative optical arrangement is shown in Figure 3-1.

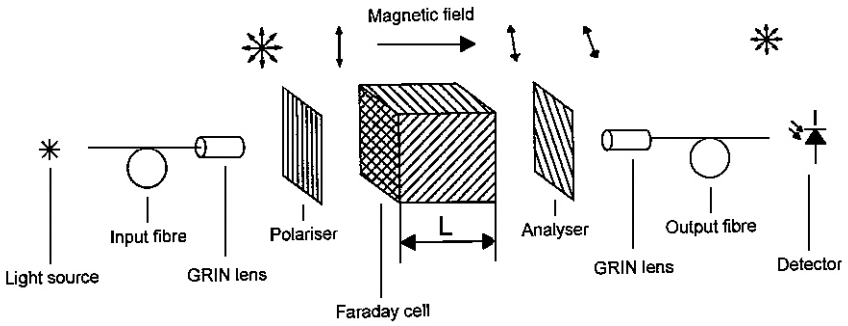


**Figure 3-1: Typical arrangement of optical components and polarisation components in a Faraday sensor.**

Typically, the polariser and analyser are arranged at an angle α of 45˚ in order to maximise the sensitivity of the OCS response and ensure that it operates within the linear region of the sensor response characteristic as shown in Figure 3-2. The OCS maximum dynamic range is defined by the two extremes of the angle θ. Maximum optical power will be received at the photodetector input when θ = -45˚, and the minimum optical power will be received when θ = +45˚. The minimum received optical power is determined by the extinction ratio of the polarisers used in the particular design of the sensor, and in this discussion is assumed as zero [2], [3].

Assuming that the rotation θ can change at maximum between -45˚ and 45˚, and that the measured current is in a sinusoidal form, θ can be expressed as a sinusoidal function directly proportional to the modulation factor k:

$$\theta(t) = \frac{\pi}{4}k\sin(\omega t) \quad (4)$$

where, ω is the angular frequency and $k \in (0,1)$.

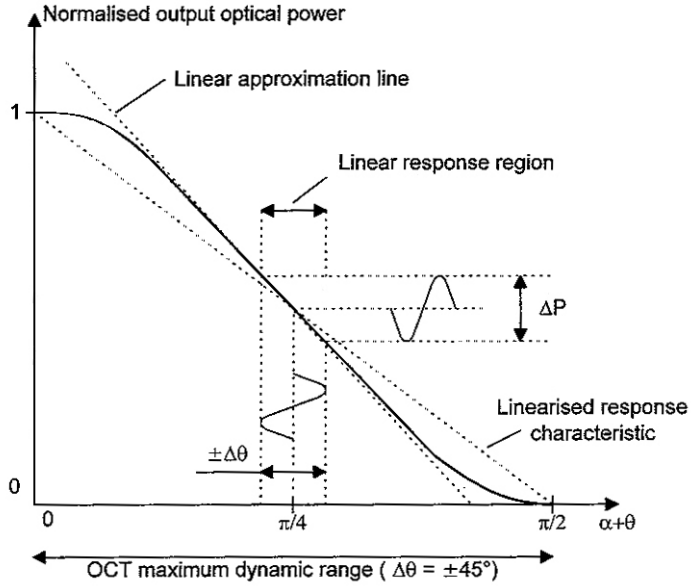


**Figure 3-2: Explanation of the sensor linear response region**

With no applied field, the optical power input to the detector is only half the input power. If the rotation is small, the change in detector output is practically a linear function of the field. From equation (3), where α is replaced by (45˚+θ(t)), the optical power at the detector is given by

$$P_{\det}(t) = \frac{1}{2} P_{in}\left(1 - \sin\left(2\theta(t)\right)\right) \tag{5}$$

assuming there is no birefringence. The detector signal will thus consist of a steady dc level, and a superimposed ac component that represents the modulation due to the Faraday effect. The ac component is given by

$$P_{ac}(t) = \frac{1}{2} P_{in} \sin 2\theta(t) \tag{6}$$

and the dc component is simply

$$P_{dc} = \frac{1}{2} P_{in} \tag{7}$$

While the ac part of the signal contains information about the current, it cannot be used alone to represent the measurement. This is because a change in the optical attenuation or light source power would appear to have the same effect as a change in modulation. The output can be normalised by computing the ratio of the ac to the dc component.

$$\frac{P_{ac}}{P_{dc}} = 2\theta(t) = AI(t) \tag{8}$$

Where I(t) represents the current being measured, and A is a constant depending on design. The value thus obtained is independent of the value of optical power, $P_{in}$ [1], [2].

The configuration shown in Figure 3-3 [1] is referred to as a witness sensor due to the sensor's close proximity to a conductor. Using this configuration the magnetic field at a point near the conductor can be sensed.

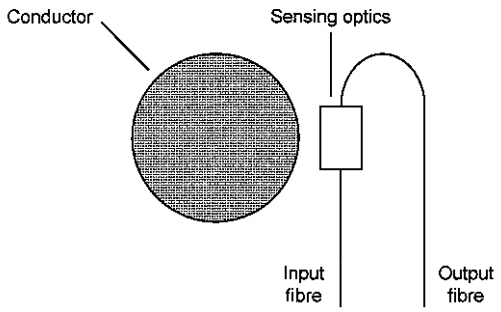


**Figure 3-3: Witness sensor configuration for Faraday effect based sensors**

Another possibility is to place the sensing element in a flux concentrator, which amplifies the magnetic field passing through the Faraday cell [4], [5], [6]. In this approach, a magnetic circuit surrounds the conductor; the field inside the magnetic core is measured optically in an air gap, as shown in Figure 3-4 [1].

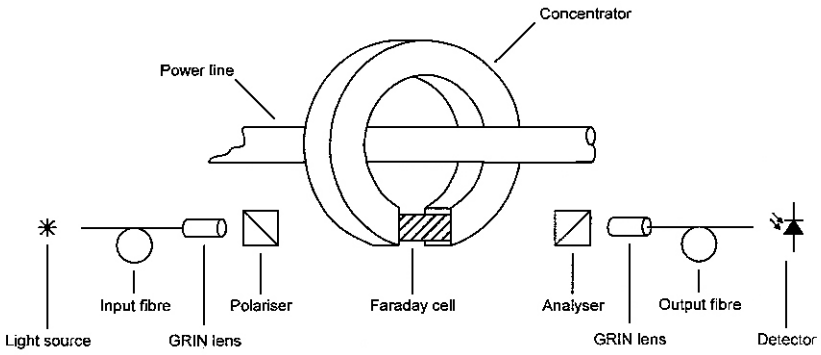


**Figure 3-4: Magnetic concentrator with optical measurement**

## 3.2 Fibre Optic Current Sensors Based on the Magnetostrictive Effect

A different phenomenon to the magneto-optic effect can be employed to perform indirect current measurement, namely: the magnetostrictive effect. Magnetostrictive materials exhibit strain in the presence of an applied external magnetic field.

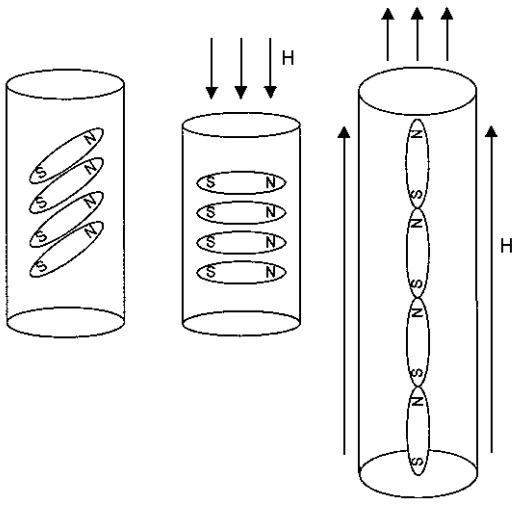


**Figure 3-5: Explanation of the magnetostrictive effect**

This phenomenon has been used previously in magnetostrictive fibre optic sensors that effectively measure strain induced by a magnetic field [7], [8], [9]. Usually, an optical fibre which forms a sensing arm of a Mach-Zehnder interferometer is wound on a magnetostrictive tube which surrounds a conductor. The tube and hence the fibre are stretched due to the magnetic field, and by measuring the optical path difference, the measurement of magnetic field is realised. This solution cannot be directly employed in the present application since the optical path would exceed several times the coherence length of the optical power source, and so the interference condition at the detector side would not be valid.

However, strain can be measured using FBG or Extrinsic Fabry-Perot Interferometric (EFPI) sensors mounted onto, or embedded into a piece of magnetostrictive material.

The FBG is a relatively new type of fibre optic sensor. It is generally classed as an interferometer. FBGs are relatively simple sensing elements which can be photo-inscribed into a silica fibre and have all the advantages normally attributed to fibre sensors. In addition the devices have an inherent self-referencing capability and are easily multiplexed in a series fashion along a single fibre. Grating-based sensors are effective for a variety of applications; in particular the area of distributed embedded sensing in materials for creating “smart structures” is of primary interest. Gratings may also prove to be useful as the optical sensing element in a range of other fibre sensor configurations; grating-based chemical sensors, pressure sensors, and accelerometers are examples [10].

The basic principle of operation of an FBG-based sensor system lies in the monitoring of the shift in wavelength of the returned “Bragg” signal, as a function of the measurand (e.g., strain, temperature). The Bragg wavelength is related to the refractive index of material and the grating pitch.

Sensor systems involving such gratings usually work by injecting light from a spectrally broadband source into the fibre, with the result that the grating reflects a

narrow spectral component at the Bragg wavelength, or in transmission this component is missing from the observed spectrum. This is diagrammatically represented in Figure 3-6.

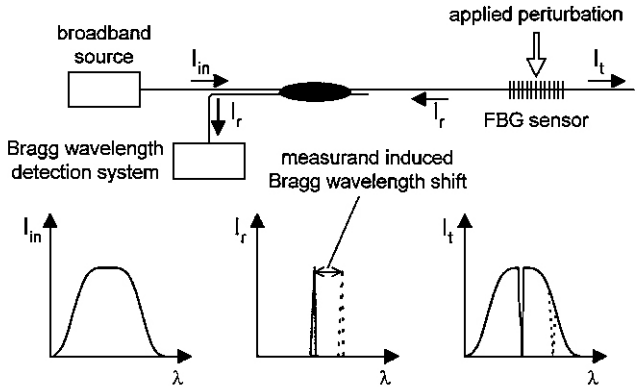


**Figure 3-6: Basic Bragg grating sensor system with transmittive or reflective detection options**

Bragg grating sensors are well suited to quasi-distributed point measurement of strain or temperature at known positions in an optical fibre network, for example. The operation of the sensor is straight forward; the strain response occurs as a result of both the physical elongation of the sensor (and the corresponding change in the grating pitch) and the change in fibre index due to photoelastic effects. The inherent thermal expansion of the fibre material and the temperature dependence of the refractive index cause the response to the temperature change, to give a change in the wavelength associated with the grating that has thus been perturbed.

A particular advantage of the use of FBGs in sensing applications is the in-built self-referencing capability, where by encoding directly in wavelength terms (an absolute parameter), this gives an output which does not depend directly on the total light intensity or losses in the connecting fibres and couplers, or the source power used. As discussed earlier, the wavelength-encoded nature of the output facilitates wavelength division multiplexing (WDM) where several sensors are connected in series and by allowing each sensor to be assigned to a different element of the

wideband available source spectrum. Strain, temperature, or potentially other measurands can thus be determined by knowledge of that part of the wavelength spectrum associated with a particular spatial location. The upper limit to the number of gratings which can be addressed in this way depends on the source bandwidth, the operational wavelength bandwidth required for each grating element and the sensitivity of the signal processing [10].

FBGs operating around 1550 nm are commercially available at approximately £300 per high temperature (up to 350˚C) grating. FBG sensors can be interrogated using commercially available instruments (Micron Optics FBG IS) or using Fabry-Perot Scanning Filters with custom-built interrogation electronics.

A further solution that can be employed to build a magnetic field or current sensor is Fabry-Perot Interferometry. A wire made of magnetostrictive material, such as nickel, can be used as a sensing part of the transducer shown in Figure 3-7. Changes in the length of the magnetostrictive element due to the magnetic field cause changes in the cavity length and hence the spectral detail of the reflected light [11].

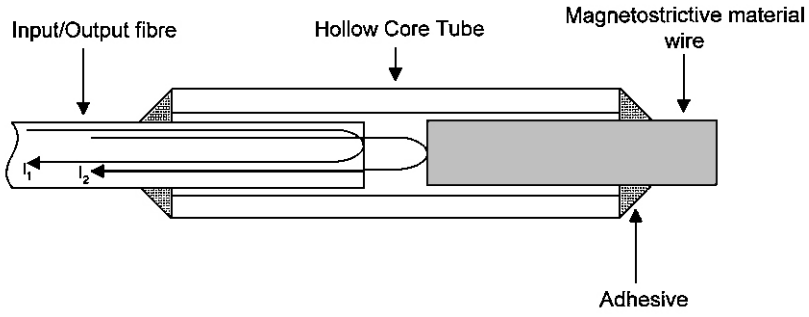


**Figure 3-7: EPFI sensor with magnetostrictive element**

The configuration shown in Figure 3-8 demonstrates how a magnetostrictive effect based OCS could be used as a witness sensor (point sensor).

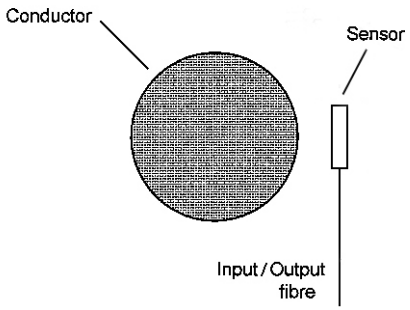


**Figure 3-8: Witness sensor configuration for magnetostrictive effect based OCS**

## 3.3 Proposed Sensor Technology

For the reasons discussed within this chapter and the previous chapter, the best sensing technique for this application is wavelength encoded sensing. There are a variety of types of wavelength encoded optical sensors. The most popular are Fibre Optic EFPI sensors and FBG sensors both of which were briefly discussed in the previous section.

EFPI sensors have been successfully shown to measure temperature, mechanical vibration, acoustic waves and magnetic fields. A number of sensor configurations have been reported in the literature [12], although these devices are bulky and require compensation for vibration and temperature. They are also more difficult to multiplex than FBGs because of the nature of the reflected signal.

FBG based sensors offer numerous advantages over EFPI sensors, including the potential to produce a more compact sensor design, insensitivity to source intensity fluctuations and greater multiplexing possibilities.

FBGs were chosen as the preferred sensing medium in the course of this research and will be discussed further in the next chapter.

## 3.4 Chapter References


[1] Dziuda, L., Fusiek, G., "Development of an On-line Optical Monitoring System for Subsea Electrical Submersible Pumps – Potential Technical Solutions," Internal Report, Centre for Electrical Power Engineering, SE/ESP/TR/2002-001.

[2] Niewczas, P., "Implementation of a Faraday Effect Based Optical Current Transducer using Digital Signal Processing Techniques", PhD Thesis, University of Strathclyde, Department of Electronic and Electrical Engineering, June 2000.

[3] Kirkham, H., Weikel, S.,"Optical Current Transducers For Power Systems: A Review", IEEE Transactions on Power Delivery, Vol. 9, No. 4, October 1994, pp.1778-1788.

[4] Deeter, M.N., "Fiber-optic Faraday-effect magnetic-field sensor based on flux concentrators," Applied Optics, Vol. 35, Issue 1, 1996, pp.154-157.

[5] Li, G., Kong, M.G., Jones, G.R., Spencer, J.W., "Sensitivity Improvement of an Optical Current Sensor with Enhanced Faraday Rotation," Journal of Lightwave Technology, Vol. 15, No. 12, December 1997, pp2246-2252.

[6] Guerrero, H., Pérez del Real, R., Fernández de Caleya, R., Rosa, G., "Magnetic field biasing in Faraday effect sensors," Applied Physics Letters, Vol. 74, Issue 24, 1999, pp.3702-3705.

[7] Jarzynski, J., Cole, J. H., Bucaro, J. A., Davis, C.M., "Magnetic field Sensitivity of an optical fiber with magnetostrictive jacket," Applied Optics, Vol. 19, Issue 22, 1980, pp.3746-3748.

[8] Bibby, Y.W., Larson, D.C., Tyagi, S., Bobb, L.C., "Fiber Optic Magnetic Field Sensors Using Metallic-Glass-Coated Optical Fibers," 8th Optical Fiber Sensors Conference, 1992, pp.161-164.

[9] Koo, K.P., Sigel, G.H., "Characteristics of fiber-optic magnetic-field sensors employing metallic glasses," Optical Letters, Vol. 7, Issue 7, 1982, pp334-336.

[10] Grattan, K.T.V., T. Sun, T., "Fibre optic sensor technology: an overview", Sensors and Actuators Vol. 82, No. 1, May 2000, pp.40-61.

[11] Ki Dong Oh, J. Ranade, V. Arya, A. Wang, R.O. Claus, “Optical fiber Fabry-Perot Interferometric Sensor for Magnetic Field Measurement”, IEEE Photonics Technology Letters, Vol.9, Issue 6, June 1997, pp.797-799.

[12] Yoshino, T., Kurosaw, K., Itoh, K., Ose, T., “Fiber-Optic Fabry Perot Interferometric Sensor,” IEEE Journal of Quantum Electronics, Vol. QE-18, October 1982, pp.1624-1633.

# 4 Fibre Bragg Gratings

FBGs are spectrally encoded optical fibre sensors. The first in-fibre Bragg grating was demonstrated by Hill *et al* in 1978 at the Canadian Communications Research Centre, Ottowa [1]. Bragg gratings, written into optical fibre, have had a significant impact on optical fibre communications systems and optical fibre sensors since the late 1980s.

FBGs consist of periodic modulations in the refractive index of the core of an optical fibre as illustrated in Figure 4-1. The modulations induced in the fibre result in a series of partially reflecting planes at periodic intervals throughout the sensing region. The length of this region is typically 1-20 mm, and the grating reflectivity can approach ~100% [2].

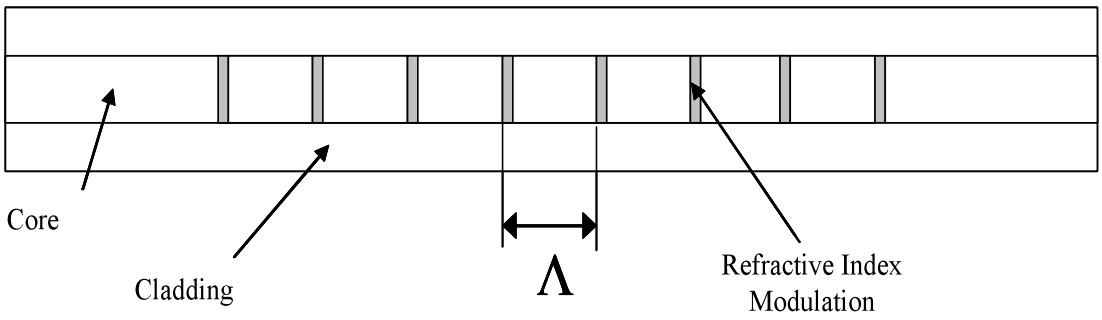


**Figure 4-1: Fibre Bragg grating schematic diagram**

## 4.1 Fabrication of the Fibre Bragg Grating

FBGs are constructed by introducing a periodic modulation to the refractive index of a segment of the core of a germanium-doped single-mode optical fibre. The most commonly used method of conducting this process is by photo inscribing the silica fibre. When doped with germanium, silica fibre becomes photosensitive to ultraviolet light, and it is due to this effect that ultraviolet lasers can be used to inscribe the gratings. Exposing the fibre core to a spatial pattern of ultraviolet light in the region of 244-248 nm creates an interference pattern, holographically inducing the refractive

modulation in the grating as illustrated in Figure 4-2. It is the coherence of the lasers that creates such an accurate interference pattern [3].

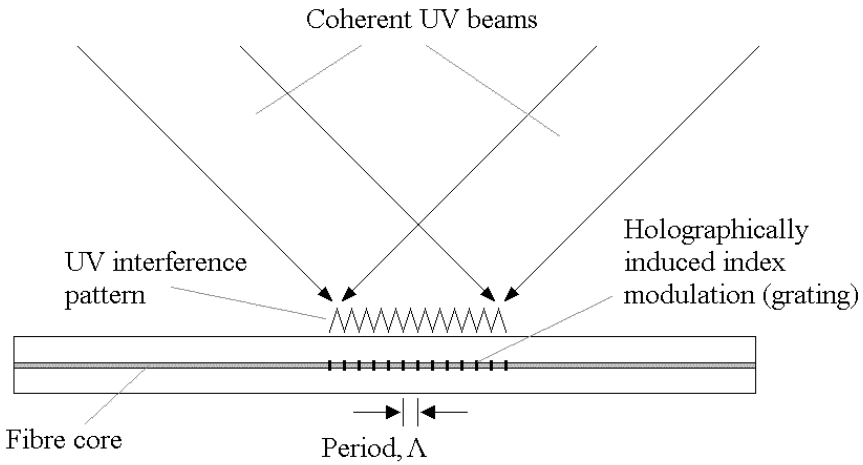


**Figure 4-2: Fibre Bragg grating fabrication**

Alternatively one UV laser can be used with a phase mask to create the same modulation in the fibre core's refractive index [4].

## 4.2 Operation of Fibre Bragg Grating Sensors

As discussed briefly in section 3.2, when an FBG is illuminated by a broadband light source, the reflections from each of the modulations interfere with each other. The interference is destructive unless each beam is in phase with all of the others. This condition occurs at only one wavelength, known as the Bragg wavelength. The Bragg wavelength, $\lambda_B$, for a particular grating is given by

$$\lambda_B = 2 \cdot n \cdot \Lambda \tag{9}$$

where $\Lambda$ is the period of the index modulation (sometimes referred to as the grating pitch) and $n$ is the refractive index of the fibre core.

In order to provide a high range-to-resolution factor, FBGs require a relatively broadband source linewidth and high input power. High bandwidth is necessary if large wavelength shifts induced by the measurand are to be measured. A high-resolution wavelength-shift detection system is desirable in order to provide the maximum possible accuracy. The method used for interrogation of the FBG sensor designed in this research will be described in Chapter 9.

The main sensing applications for FBGs are strain and temperature, although they can be used to indirectly measure other parameters. The strain response arises due to both the physical elongation of the FBG (and hence, an increase in the grating pitch) and the change in fibre index due to the photoelastic effect. The thermal response arises primarily from the temperature dependence of the refractive index, although thermal expansion also plays a part. The shift in Bragg wavelength with changes in strain (ε) and temperature (T) can be expressed using

$$\Delta\lambda_B = 2 \cdot n \cdot \Lambda \cdot \left( \left\{ 1 - \left( \frac{n^2}{2} \right) \cdot \left[ P_{12} - \nu \cdot \left( P_{11} + P_{12} \right) \right] \right\} \cdot \varepsilon + \left[ \alpha + \frac{\left( \frac{dn}{dT} \right)}{n} \right] \cdot \Delta T \right) \tag{10}$$

where ε is the applied strain, $P_{i,j}$ are the Pockel's coefficients of the stress-optic tensor, ν is Poisson's ratio, α is the coefficient of thermal expansion of the fibre and ΔT is the temperature change. The measured strain response at a constant temperature is found to be

$$\frac{1}{\lambda_B} \cdot \frac{\delta\lambda_B}{\delta\varepsilon} = 0.78 \times 10^{-6} \, \mu\varepsilon^{-1} \tag{11}$$

while the measured temperature response at constant strain is

$$\frac{1}{\lambda_B} \cdot \frac{\delta \lambda_B}{\delta T} = 6.67 \times 10^{-6} \, ^{o} C^{-1} \tag{12}$$

Therefore, at 1550 nm, a 1 pm change in Bragg wavelength is approximately equal to a 0.8 με change in strain or a 0.1ºC change in temperature [5].

Figure 4-3 shows the change in the reflection spectrum of an FBG due to strain. The applied compressive strain was approximately 1900 με (microstrain), while the applied tensile strain was approximately 2200 με [6].

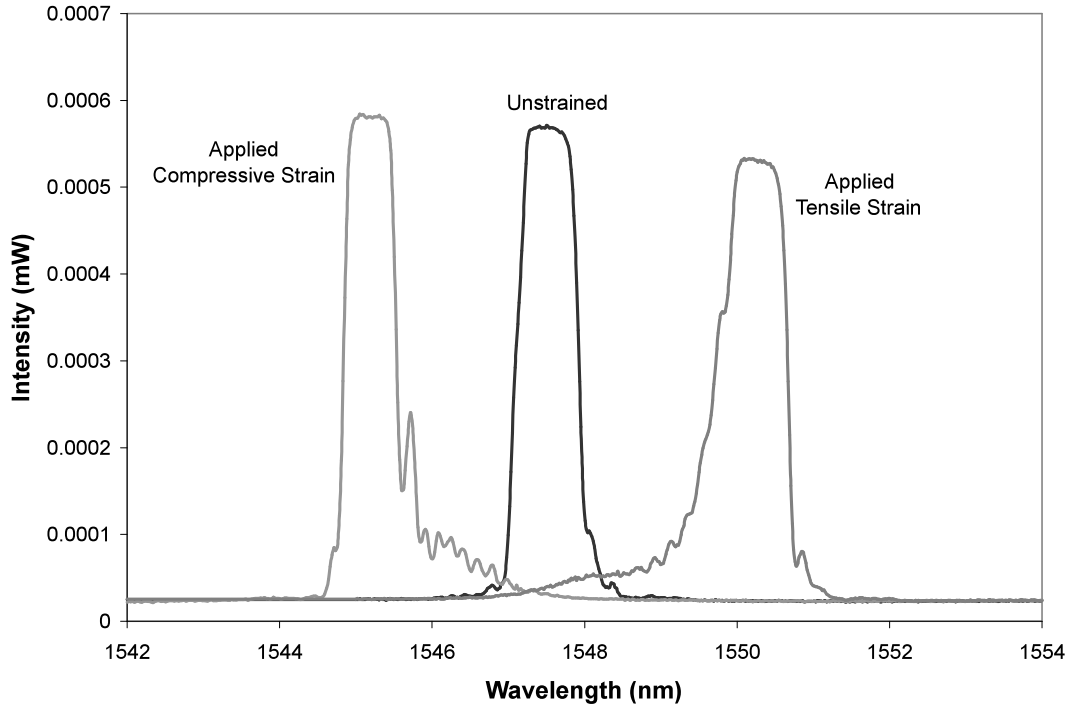


**Figure 4-3: Change in Bragg grating response with applied strain**

This demonstrates that with the use of a single FBG, it is impossible to distinguish between the change in wavelength due to strain and that due to a change in

temperature. Therefore when measuring either parameter it is necessary to provide a means of compensation for the other effect. Therefore, when measuring strain, a second FBG is often used as a method of providing a temperature reference. This would be located in the same thermal environment as the first, but would be isolated from the strain being measured. By subtracting the wavelength shift seen in the isolated FBG from the wavelength shift of the strained FBG, the effects of temperature variation can be negated.

Three distinct types of Bragg grating have been identified [7]. They are classified as Type I, Type II and Type IIA (sometimes known as Type III), referring to the different methods by which the gratings are written into the fibre [8]. The main practical difference between the grating types is seen in their thermal stability. Type I gratings are relatively stable at moderate temperatures, but reflectivity starts to decrease following prolonged exposure to higher temperatures (200-300ºC). Type IIA gratings have considerably better thermal stability, with no noticeable drop in reflectivity until around 450ºC. At temperatures of 600ºC and above, both Type I and Type IIA gratings are quickly erased from the fibre. Type II gratings can survive these temperatures, but their optical quality is poor, with considerable scattering losses. Type I gratings were used exclusively during the research reported in this thesis.

There have been several recent developments in Bragg grating types including chemical composition gratings and Bragg stacks. These sensors can survive temperatures in excess of 900 ºC compared to a limit of around 500 ºC for UV-written Bragg gratings. For greater detail, the reader is directed to references [9] and [10].

## 4.3 Advantages and Disadvantages of FBG Based Sensors

FBGs [2], [5] have become one of the most widely used and commercially successful types of fibre optic sensor as they have a number of distinct advantages over other types:

- They can give an absolute measurement that is insensitive to fluctuations in the intensity of the illuminating source, as the information is normally obtained by detecting the wavelength shift induced by the measurand.

- They can be written directly into the fibre without changing the fibre diameter. This makes them compatible with a wide range of applications where small sensors are favourable.

- They can be mass-produced at low cost.

- They can be easily multiplexed using wavelength division multiplexing (WDM) such that several sensors can be addressed with one optical fibre, making quasi-distributed point sensing feasible in practice [11]. Because each grating occupies only a small section of the available spectrum, multiple gratings can be connected in series. Each sensor is immediately identifiable by its own assigned wavelength, allowing distributed, absolute measurements to be readily obtained.

Although in many ways an ideal candidate for use in the current sensor in this application, FBGs have some drawbacks in that they are sensitive to influences other than the measurand. These influences include vibration, pressure, temperature and strains induced by other factors. For the purposes of current measurement, the FBG reading must be decoupled from these parameters that can potentially influence the reading.

## 4.4 Interrogation of FBG Sensors

Wavelength-encoded sensors like FBGs operate by changing the spectrum of the light incident upon them such that the change can be related to the measurand. An interrogation system must therefore be capable of analysing a broad spectrum of light and detecting these changes. Since photodiodes are wavelength-insensitive, some method of discriminating wavelength and recording the power level at that wavelength must be used.

When illuminated by a broadband source, the characteristics of which can be seen in Figure 4-4 (a), FBGs reflects a narrow portion of the spectrum at a wavelength determined by the grating pitch and the refractive index of the fibre (Figure 4-4 (b)). Changes in strain are detected through a change in grating pitch. Temperature changes are measured primarily through a change in refractive index with temperature, although thermal expansion of the grating also has an effect.

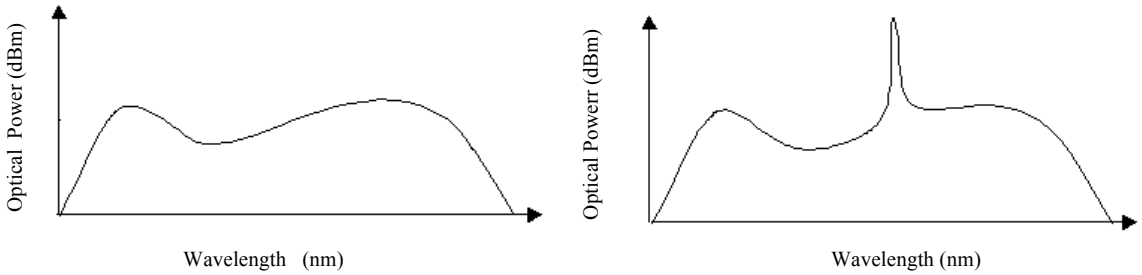


**Figure 4-4: (a) Characteristic of the broadband light source (b) Reflected signal from an FBG**

The interrogation of wavelength-encoded optical fibre sensors using scanning filters has been demonstrated by many researchers [2], [12], [13], [14]. Figure 4-5 shows a typical set-up. Light from a broadband source enters a scanning spectral filter, a device which allows only a narrow bandwidth of light to pass through it. The position of the filter in the spectrum is controllable so the whole source spectrum can be swept using simple control circuitry. The light passes through a fused coupler to the sensor, which reflects a proportion of the light back through the coupler to a photodetector, which measures the light intensity. The position of the filter provides a wavelength reference for the intensity at each point. Once the filter has swept across the whole spectrum, the spectrum can be reconstructed and the sensor response analysed. This method normally has a high resolution and a large operational range, though these are both dependent on the filter design.

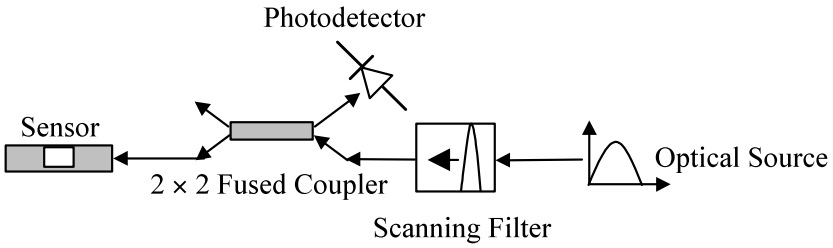


**Figure 4-5: Typical FBG interrogation set-up**

Precision Measurement of the FBG wavelength shift induced by the measurand is crucial for achieving good sensor performance. The general requirements for an ideal interrogation method are as follows:

- High resolution with large measurement range: typically a wavelength-shift detection resolution ranging from sub-picometre to a few picometres is required for most applications: the range to resolution is within $10^3$:1-$10^5$:1.
- Cost effective: the cost of an interrogation system should be competitive with conventional optical or electrical sensors.
- Compatible with multiplexing: the interrogation scheme should be able to cope with multiplexing topologies making the whole sensing system cost effective.

FBG sensors can be interrogated using commercially available instruments such as Micron Optics Fibre Bragg Grating Interrogation System (FBG-IS) or using Fabry-Perot Scanning Filters with custom-built interrogation electronics. Both of these methods were used during the experimental stage of this project and will be discussed in a later section.

## 4.5 Chapter References


[1] Hill, O.K., Fuji, Y., Johnson, D.C., Kawasaki, B.S., "Photosensitivity in Optical Fibre Waveguides: Application to Refection Filter Fabrication", Applied Physics Letters, Vol. 32, Issue 10, 1978, pp. 647-649.

[2] Rao, Y.J., "In-fibre Bragg Grating Sensors," Measurement Science Technology, Vol. 8, 1997, pp. 355-375.

[3] Grattan, K.T.V., Sun, T., "Fiber Optic Sensor Technology: An Overview", Sensors and Actuators A: Physical, Vol. 82, No.1, May 2000, pp40-61.

[4] Hill, K.O., Meltz, G., "Fiber Bragg Grating Technology Fundamentals and Overview", Journal of Lightwave Technology, Vol. 15, No. 8, August 1997, pp. 1263-1276.

[5] Kersey, A.D., Davis, M.A., Patrick, H.J., LeBlanc, M., Koo, K.P., "Fiber Grating Sensors", Journal of Lightwave Technology, Vol. 15, No. 8, August 1997.

[6] Willshire, A.J., "Robust Optical Sensor System for Aero-Engine Monitoring," PhD Thesis, University of Strathclyde, Department of Electronic and Electrical Engineering, 2004.

[7] Culshaw, B., Dakin, J., "Optical Fiber Sensors," Vol. 3, Artech House, 1996.

[8] Grattan, K.T.V., Meggitt, B.T., "Optical Fiber Sensor Technology," Vol. 2, Chapman & Hall, 1998.

[9] Fokine, M., "Formation of Thermally Stable Chemical Composition Gratings in Optical Fibers," Journal of the Optical Society of America B, Vol. 19, Issue 8, August 2002, pp.1759-1765.

[10] Luo, F., Hernandez-Cordero, J., Morse, T., "Multiplexed Fiber-Optic Bragg Stack Sensors (FOBSS) for Elevated Temperatures", IEEE Photonics Technology Letters, Vol. 13, Issue 5, May 2001, pp514-516.

[11] Dakin, J.P., Volanthen, M., "Distributed and Multiplexed Fibre Grating Sensors Including Discussion of Problem Areas," IEICE Trans. Electron., Vol. E83-C, No. 3, March 2000, pp.391-399.

[12] Kersey, A.D., "Interrogation and Multiplexing Techniques for Fiber Bragg Grating Sensors", SPIE, Vol. 2071, pp.30-48.

[13] Xu, M. G., Geiger, H., Archambault, J. L., Reekie, L., Dakin, J.P., "Novel Interrogation System for Fibre Bragg Grating Sensors Using an Acousto-Optic Tunable Filter," Electronic Letters, Vol. 30, No.13, 1994, pp.1085-1087.

[14] Johnson, G.A., Todd, M.D., Althouse, B.L., Chang, C.C., "Fibre Bragg Grating Interrogation and Multiplexing with a 3 x 3 Coupler and Scanning Filter," Journal of Lightwave Technology, Vol. 18, No.8, August 2000, pp1101-1105.

# 5 Magnetostriction and Magnetostrictive Materials Overview

In previous chapters optical sensing techniques were discussed. Chapter 4 focused on FBGs and their ability to measure strain and temperature, as this forms part of the sensing technique chosen by the author for use in the prototype sensor design. In this chapter a brief overview of magnetostriction and magnetostrictive materials is given. Thought will be given to how the strain exhibited by magnetostrictive materials in the presence of a magnetic field could potentially be measured by an FBG in order to indirectly measure current.

## 5.1 Magnetostriction

The study of magnetostriction began in 1842 when James P. Joule first observed that a sample of iron changes its length when magnetised with a magnetic field. Magnetostriction, λ, is a property that causes a fractional change of length as a result of a change in magnetisation in certain ferromagnetic materials [1].

$$\lambda = \frac{\Delta l}{l} \tag{13}$$

Magnetostriction occurs as a result of the rotation of small magnetic domains present in magnetostrictive materials and can be brought about by the application of magnetic fields, heat or stresses. Magnetic domains are small volumes in which all magnetic moments lie parallel [2]. The regions separating magnetic domains are called domain walls where the magnetisation rotates coherently from the direction in one domain to that in the next domain. As these domains rotate they produce internal strains in the material causing it to expand in the direction of the applied magnetic field, shown in Figure 5-1. Increasing the field results in more domains rotating to become aligned in the direction of the applied field. Saturation occurs when nearly all of the domains are aligned in the direction of the field as depicted in Figure 5-1 (b) and (c).

Referring again to Figure 5-1, if the magnetostriction is positive, the material sample elongates irrespective of the direction of the magnetic domains, and the diameter is reduced such that the volume remains constant. If the magnetostriction is negative, the material length decreases and the diameter increases.

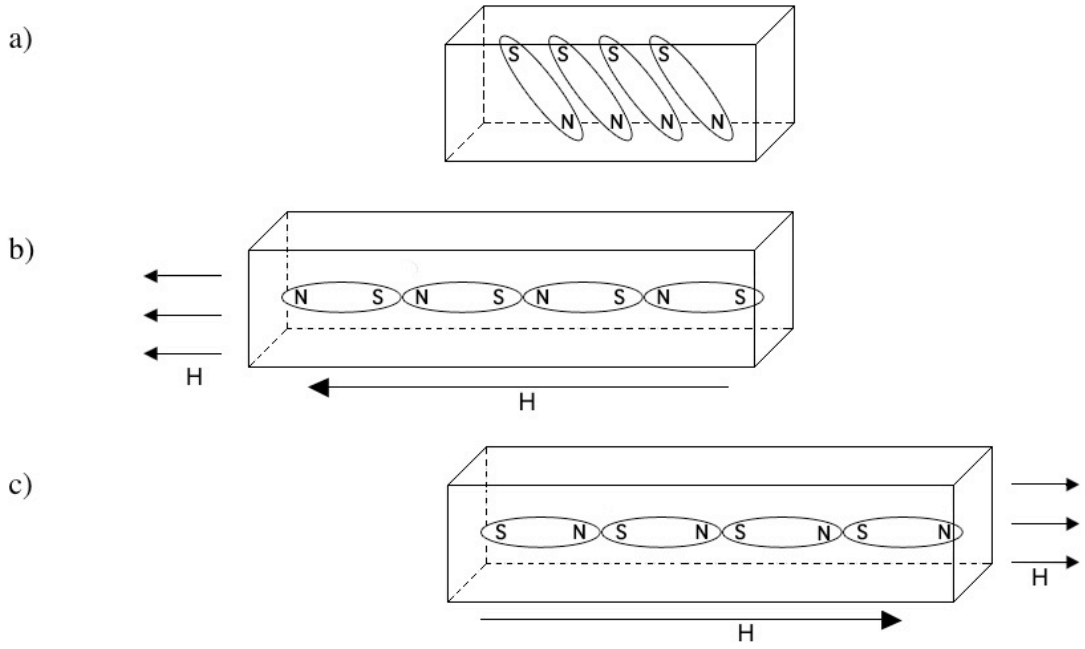


**Figure 5-1: Material response to an applied magnetic field**

The illustrations of domains are conceptual only and are not meant to give an accurate scale of the size or shape of the domains.

The Joule effect or Joule magnetostriction, as discussed in this section, is only one of many physical effects of magnetostriction: others such as the Villari effect, ΔE effect, Wiedemann effect and magnetovolume effect can all be observed. However it is Joule magnetostriction that is of primary interest in the design of the prototype sensor in this research. For great detail on these effects the reader is directed towards [1], [4].

## 5.2 Magnetostrictive Materials

Magnetostrictive materials are ferromagnetic materials, and can be broadly defined as materials that undergo a change in dimension due to a change in magnetisation state. All magnetic materials exhibit varying degrees of magnetostriction, however only some materials exhibit sufficient magnetostriction for practical use.

There is a wide range of traditional magnetostrictive materials on the market, but relatively few 'giant' magnetostrictive materials. The difference between traditional magnetostrictive materials as opposed to 'giant' magnetostrictive materials is the amount of strain per unit volume of the material. Giant magnetostrictive materials are materials that undergo large amount of strain for a given applied magnetic field. One such material in the giant magnetostriction category is Terfenol-D.

Magnetostriction involves a bi-directional energy exchange between magnetic and elastic states. It is an inherent property of magnetostrictive materials that does not decay with time [2]. In fact, it has unlimited cycle life with microsecond response time [3]. However, all magnetostrictive materials have a maximum temperature above which their magnetic properties disappear. This temperature is known as the Curie temperature and varies from material to material. While subjected to temperatures in excess of the Curie temperature magnetostrictive materials loose their magnetic properties. While they do not produce strain above their respective curie temperatures, strain performance fully recovers upon cooling [4].

Of the wide range of magnetostrictive materials that are commercially available Terfenol-D has one of the highest Curie temperatures at 380ºC. With the general operating temperature of an ESP being approximately 150ºC [5], [6], if such a material was utilised in the sensor design, the operating temperature of the sensor should not exceed the Curie temperature of the magnetostrictive material, ensuring that it does not loose its magnetostrictive properties during normal operation.

The general stoichiometry (chemical composition) of the Terfenol-D alloy is $Tb_xDy_{1-x}Fe_y$. The composition normally used is x = 0.30 and y = 1.92. It was

discovered by a group of Navy scientists led by A. E. Clark in the 1970's and has been commercially available since the late 1980s. Its name represents the composition of the material and the original name of the Naval Laboratory in which it was discovered (Ter: terbium, Fe: iron, nol: Naval Ordnance Laboratory and D: dysprosium) [7].

Terfenol-D exhibits the greatest magnetostriction of any commercially available magnetostrictive materials and is one of the most commonly used materials in actuator applications. It is said to produce strains in excess of 1000 x $10^{-6}$ ppm. These large strains are the direct consequence of a strong magnetoelastic coupling arising from the dependency of magnetic moment orientation with interatomic spacing.

In this research the prototype sensor design utilises the Joule magnetostrictive effect. The magnetostrictive material used to construct the sensor for this research was not Terfonol-D, because of its high retail price. The material used however, is a $Tb_xDy_{1-x}Fe_y$ magnetostrictive alloy with a similar stoichiometry to that of Terfenol-D. It is grown as a solid-state crystal from elemental forms of Terbium, Iron and Dysprosium and is also capable of producing giant magnetostriction at moderate magnetisation levels at room temperature [8]. It exhibits similar properties to Terfenol-D as shown in Table 1 [3], [8].

While the valve of each of the physical properties is not precisely the same for both of the materials, they are fairly similar. They both have very similar values for Young's modulus, coefficient of thermal expansion, resistivity, relative permability and coupling factor. Although their tensile and compressive strengths vary somewhat, the yield strength of both materials is much greater in compression than in tension. The sensor material may even have a higher Curie temperature than Terfenol-D.

| Physical Properties | | Terfenol-D [3] | Sensor Material [8] |
|---|---|---|---|
| **Mechanical:** | Young's Modulus: | 25 – 35 GPa | 26 ~ 35 GPa |
| | Sound Speed: | 1640 ~ 1940 m/s | 1720 ~ 2300 m/s |
| | Tensile Strength: | 28 MPa | >20 MPa |
| | Compressive Strength: | 700 MPa | >500 MPa |
| | | | |
| **Thermal:** | Coefficient of Thermal Expansion: | 12 ppm/°C | 10 ~12 ppm/°C |
| | Specific Heat: | 0.35 kJ/kg -K | 0.35 kJ/kg -K |
| | | | |
| **Electrical:** | Resistivity: | 58 x 10-8 Ω.m | 60 x 10-8 Ω.m |
| | Curie Temperature | 380°C | 380 ~ 420°C |
| | | | |
| **Magnetostrictive:** | Strain Production: | 800 ~ 1200 ppm | 1000 ~ 1300 ppm |
| | | | |
| **Magnetomechanical:** | Relative Permeability: | 3 ~ 10 | 5 ~10 |
| | Coupling Factor: | 0.75 | 0.70 ~ 0.75 |

**Table 1: Properties for Terfenol-D and material used in sensor design**

The magnetostrictive strain as a function of the applied magnetic field graph for the sensor material is shown in Figure 5-2. This graph was provided by the material manufacturer [8].

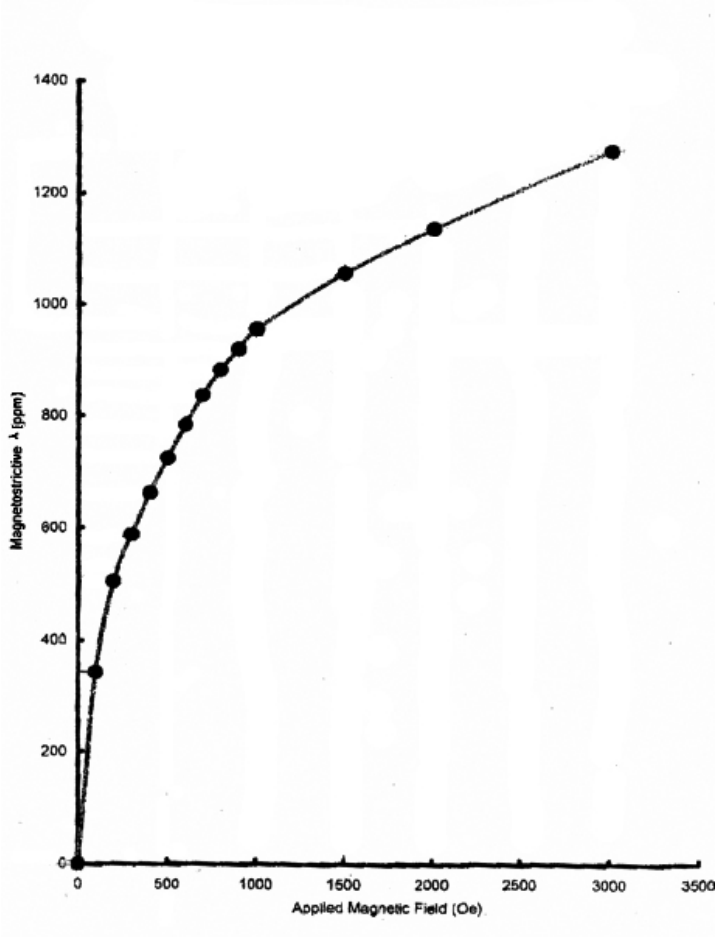


**Figure 5-2: Magnetostrictive strain as a function of applied magnetic field**

Figure 5-2 illustrates that the magnetostrictive strain (magnetostriction) exhibited by the material is not directly proportional to the applied magnetic field. In addition to this nonlinearity, the material also exhibits hysteresis or magnetic lag. This will be covered in more detail in the following chapter.

## 5.3 Chapter References


[1] David Jiles, "Introduction to Magnetism and Magnetic Materials," Chapman and Hall.

[2] Terfenol-D Section of the Department of Material Science and Engineering at Iowa State University website - http://www.iastate.edu/~terfenol/

[3] Terfenol-D Data Sheet, ETREMA Products Inc., USA, 2002 - www.etrema-usa.com.

[4] Jakubovics, J.P., "Magnetism and Magnetic Materials," Second Edition, The The Institute of Materials, Book 573.

[5] Dziuda, L., Fusiek, G., "Development of an On-Line Optical Monitoring System for Subsea Electrical Submersible Pumps - Potential Technical Solutions," Internal Report No. SE/ESP/TR/2002-001.

[6] Takacs, G., "Electrical Submersible Pumps Manual: Design, Operations, and Maintenance," Gulf Professional Publishing, 2009.

[7] Dr John L. Butler, "Application Manual for the Design of ETREMA TERFENAL – D® Magnetostrictive Transducers, ETREMA Products, Inc."

[8] Mateck Website - www.mateck.de

# 6 Magnetic Hysteresis and Other Sensor Nonlinearities

The excellent performance of magnetostrictive materials is sometimes obscured by the hysteresis and nonlinear effects which are intrinsic to magnetostriction. These inherent material characteristics along with other unwanted effects arising from the use of the optical fibre and the method in which the sensor was constructed will be discussed within this chapter. Possible methods of reducing these effects and improving the output signal from the sensor will also be reviewed.

Since the sensor is known to suffer from these undesirable effects, some form of signal processing is necessary to enable the ac current and temperature values to be more accurately determined from the sensor's optical output signal. Some possible methods of achieving this will also be explored.

## 6.1 Magnetic Hysteresis

Hysteresis is an inherent property of magnetostrictive materials. In $Tb_xDy_{1-x}Fe_y$ alloys the ratio of terbium and dysprosium influences two key properties: hysteresis and magnetostriction. Magnetostriction increases with terbium content, but so does hysteresis. Dysprosium is included in the material in order to raise the Curie temperature above room temperature. However, its inclusion reduces the magnetostriction and increases hysteresis [1].

A study of the hysteresis in a material is useful in determining several material properties as well as in gaining a more in depth understanding of the physical behaviour of the material as is discussed in [2].

When a ferromagnetic material is magnetised, some of the domains are driven beyond the point at which the changes are reversible. When the imposed field intensity is decreased to zero, the material retains some degree of magnetisation [2]. If the coil current that produces the imposed field is slowly cycled between maximum values in either direction, the corresponding values trace out a closed curve which is

called a "hysteresis loop". A typical sigmoid-shaped hysteresis loop, more commonly referred to as B/H curve, is shown in Figure 6-1.

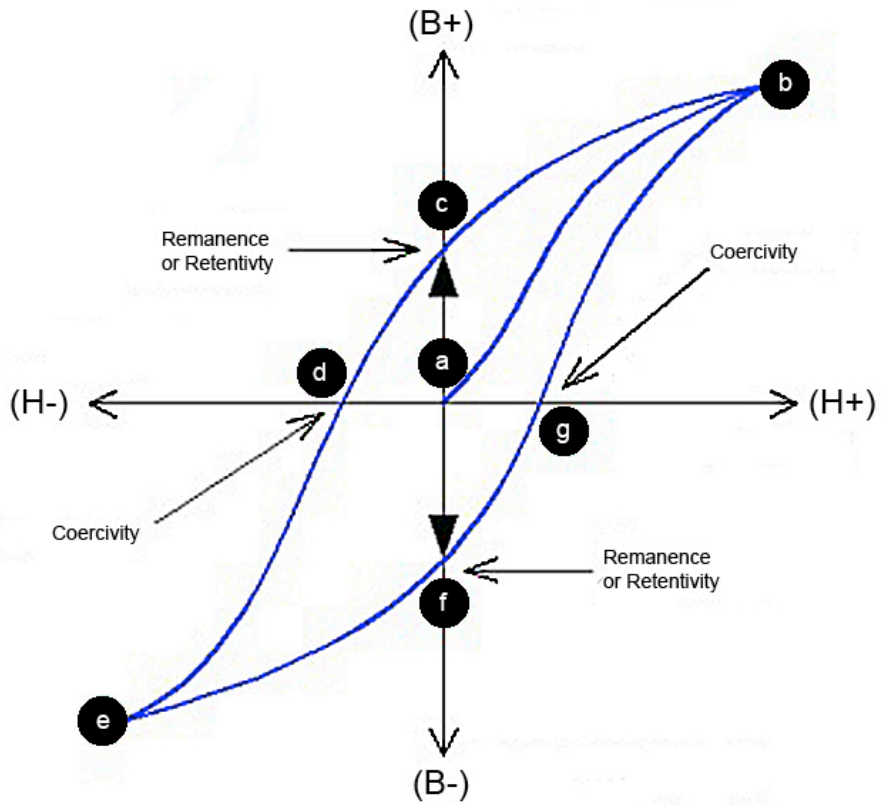


**Figure 6-1: A typical hysteresis loop for a magnetostrictive material**

Magnetic hysteresis loops plot the magnetic induction or flux density, B, of the material for various field strengths, H, and are the most common way of representing the bulk magnetic properties of the material. The magnetisation, M, can be calculated at any point on the curve using the formula [3]:

$$M = \frac{B}{\mu_o} - H \tag{14}$$

where $\mu_o$ is the permeability of free space ($4\pi \times 10^{-7}$ $Hm^{-1}$)

On application of a magnetic field to a previously demagnetised sample of magnetostrictive material, its magnetisation will gradually increase from point a where both H and B are zero. Starting from point a, if H is increased indefinitely the magnetisation will increase until eventually saturation is achieved at b. This value is called the saturation magnetisation, $M_o$ and is the upper limit of the magnetisation that can be reached. It represents a condition where all magnetic domains within the material are aligned in the direction of the magnetic field H. Thus further increases in magnetic field will not increase the flux density. The curve a-b is known as the initial magnetisation curve.

When the magnetic field H is removed or reduced back to zero, B does not retrace the curve b-a. Instead it decreases more slowly, and when H reaches zero, the magnetisation of the material will not relax back to zero (point c). This value of remaining magnetisation is referred to as the *remenance* or *retentivity*. In order to decrease B further it is necessary to apply a reverse magnetic field in order to return the magnetisation to zero (point d). This required field strength is known as the *coercivity* and is equivalent to half of the width of the loop across the H axis. After passing through point d the magnetisation continues to decrease until eventually, B reaches saturation in the opposite direction at point e. If H is increased again, B follows the curve from e through f and g back to b again. If H is continually changed between large values in opposite directions, B will vary repeatedly along the closed loop b-c-d-e-f-g-b.

### 6.1.1 Causes of Magnetic Hysteresis

Many factors contribute towards magnetic hysteresis. Some of the main factors will be discussed briefly within this section.

One mechanism which gives rise to hysteresis is caused by magnetocrystalline anisotropy. This means that properties of certain materials, known as anisotropic materials, depend on the direction of the applied magnetic field. All solids are anisotropic to some degree. In anisotropic solids certain crystallographic axes are

favoured by the magnetic domains which will prefer to lie along these directions as this leads to a lower energy. This results in discontinuous and irreversible rotation of the magnetic domains, which leads to a kind of switching action known as Barkhausen discontinuities.

In anisotropic solids certain crystallographic axes are favoured by the magnetic domains which will prefer to lie along these directions. This results from the existence of two or more minima in the free energy of magnetic crystals, between which the magnetisation may jump during magnetisation by an external field [4]. These jumps occur at zero applied fields between minima which are equivalent by symmetry, but jumping can also take place between finite fields between inequivalent minima. The reader is directed towards [5 - 7] for greater details on this subject.

Another cause of hysteresis in magnetostrictive materials is the presence of defects in the material. It has been shown in the literature that defects are unavoidable; in the case of magnetostrictive materials they are indirectly incorporated in the material to attain the desired stoichiometry. In the case of $Tb_xDy_{1-x}Fe_y$ magnetostrictive alloys, the incorporation of Dysprosium has the desired effect of increasing the Curie temperature, but its inclusion introduces what is referred to as 'magnetic inclusions' [2]. These are areas in the matrix material, in this case iron, that contain second phase materials which have different magnetic properties to that of the matrix material. In this case the second phase materials are terbium and dysprosium.

These 'magnetic inclusions' introduce pinning sites in the material which impede magnetic domain rotation and wall motion. When domain walls intersect with these pinning sites the result is a reduction in energy and if the walls remain pinned at these sites the motion becomes irreversible. This theory, called the inclusion theory of domain-wall pinning, was suggested by Kersten and leads to phenomena such as Barkhausen discontinuities [2]. These pinning sites can also be caused by cracks, pores and voids in the material. The reader is directed towards [2] for further information on this topic.

Magnetic hysteresis is a complex phenomenon, and is not yet fully understood. It is the subject of much research in the fields of mathematics, physics and engineering. While greater understanding of the phenomenon would be useful in gaining a more in-depth comprehension of the physical behaviour of the material and thus enable more detailed characterisation of the sensor, deeper research into this area was found to go beyond the boundaries of this thesis.

## 6.2 Other Sensor Nonlinearities

The relationship between magnetostriction or magnetostrictive strain, and applied magnetic field is nonlinear for $Tb_xDy_{1-x}Fe_y$ magnetostrictive alloys as previously shown in Figure 5-2. At lower applied magnetic fields, a greater strain is produced for a given applied magnetic field. As the material approaches saturation, it is less sensitive to increases in applied magnetic field. Once material saturation is reached there will be no increase in magnetostriction for a given increase in applied magnetic field.

Furthermore, if an applied magnetic field, H is continually changed between large values in opposite directions, the magnetostrictive strain exhibited by the material will always be positive. The resultant effect in the material sample can be seen in Figure 5-1. Where b) and c) shows the material response to large negative and positive magnetic fields. As can be seen when either a positive or negative magnetic fields are applied, the material elongates, until it reaches saturation.

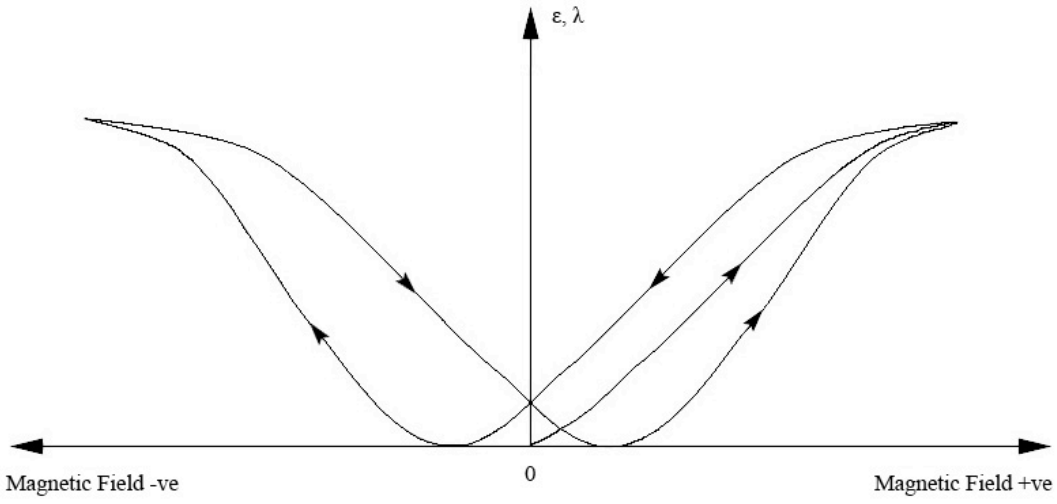


**Figure 6-2: Magnetostrictive characteristic**

This effect is illustrated in the curve plotting magnetostriction (strain) of the material for various field strengths, H shown in Figure 6-2. This type of curve is often referred to as a "butterfly" curve and shows the response of an unbiased magnetostrictive material sample. The operating or quiescent point is located at zero. When starting at this point, the application of an ac current results in a positive expansion for both positive and negative cycle of a current oscillation since the curve is a mirror image at the zero point. Therefore, the application of a 50 Hz coil current would result in a 100 Hz response from the sensor. This will be discussed further in the next section. The line originating at 0 and increasing to the saturation point is associated with initial magnetisation curve a-b shown in Figure 6-1.

## 6.3 Magnetic Bias

As touched on in the previous section, if the material was used in its natural (unbiased) state to measure ac currents, the resulting reading would have been detected at double the input frequency and there would be no way of distinguishing between positive and negative magnetic fields and thus currents. This is illustrated in Figure 6-5, where the solid lines represent the unbiased input and corresponding strain output. Not only would this be an undesirable outcome but also would prevent the

simultaneous measurement of temperature at the sensor head. This will be discussed in a later section. It was therefore beneficial to attempt to overcome this effect.

The literature has shown that in other applications, for example magnetostrictive actuators, the application of a magnetic bias via a coil has facilitated both elongations and contractions from magnetostrictive materials. This works by applying an initial magnetic field, known as a magnetic bias field, which moves the quiescent point of the material away from its zero point further along the positive scale as illustrated in Figure 6-3.

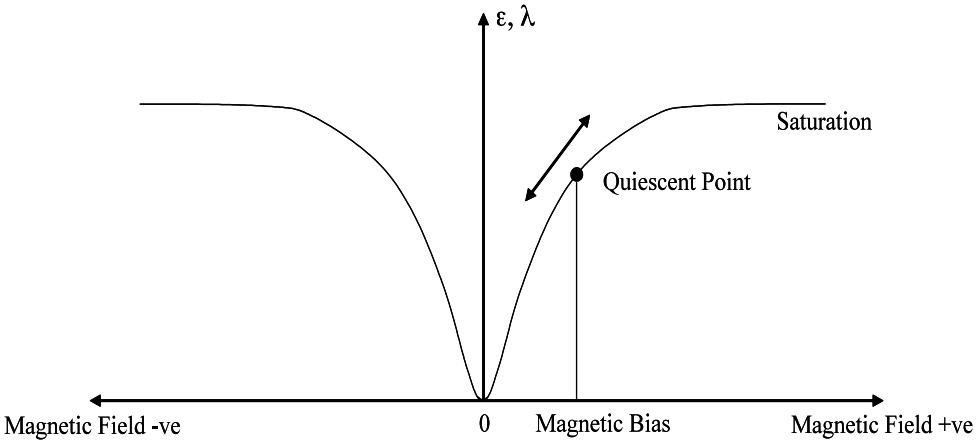


**Figure 6-3: Simplified butterfly loop showing the biased quiescent point**

This in turn causes an initial expansion of the material such that an applied positive magnetic field will further elongate the material while an applied negative magnetic field would cause it to contract.

This process is demonstrated in Figure 6-4. The application of a magnetic bias field causes an initial expansion of the material sample to position $\Delta l_o$ (see Figure 6-4(a)). Then, as a positive cycle of the ac current is introduced, the fields add causing additional expansion to position $\Delta l_{+ve}$ (Figure 6-4(b)). On the negative half of the cycle the fields are subtracted or cancelled depending on the bias applied and the displacement from the neutral position $\Delta l_o$ is reduced to position $\Delta l_{-ve}$ (Figure 6-4(c)).

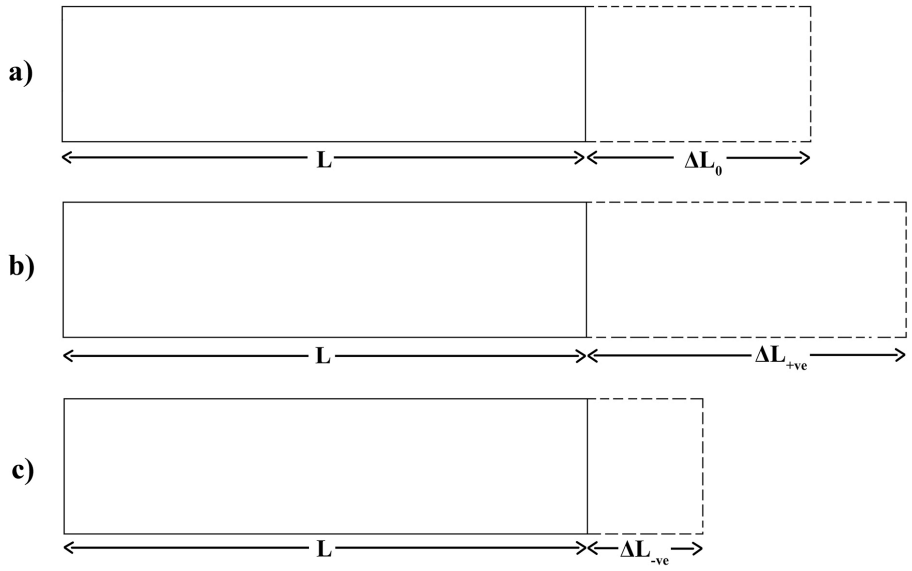


**Figure 6-4: Illustrative sketch of elongation for biased magnetostrictive material**

If an appropriate level of magnetic bias current was chosen and applied to the sensor, this could facilitate the measurement of ac currents. The dashed lines in Figure 6-5 demonstrate the performance improvements achievable by applying a magnetic bias to the material. Given that the sensor design was required to measure ac currents, the addition of a magnetic bias was found to be a positive addition to the sensor design. Therefore an optimum value of magnetic bias had to be determined.

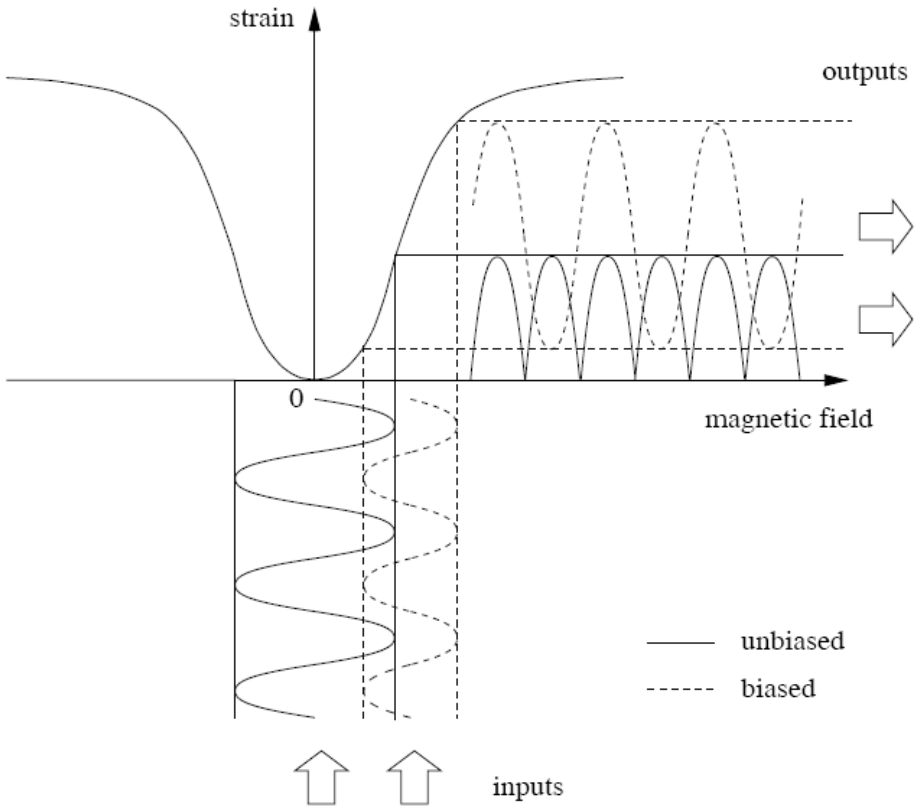


**Figure 6-5: Potential effect of a magnetic bias on the sensor output**

The optimum value of magnetic bias was determined from the material characteristic graph supplied by the material manufacturer, Figure 5-2 [8]. Choosing the most suitable operating point was a compromise between trying to operate in the most linear region of the material and avoiding moving too close to the saturation point into a region of lower magnetostriction and thus lower sensitivity. A magnetic bias of 40 kA/m was chosen as the most suitable for use in the experimental demonstration of the current sensor.

Unlike the magnetic bias facilitated by a coil, favoured in the literature, it was concluded that a magnetic bias provided by permanent magnets was more appropriate for the sensor design. This method of providing a magnetic bias was chosen in order to eliminate the need for a power supply to the coil; thus keep the sensor design as

simple and non-invasive as possible. A range of magnets was considered for this purpose, with the magnet material of choice being samarium cobalt, $Sm_2Co_{17}$.

SmCo magnets are one of two types of rare earth magnets. They are strong permanent magnets made of an alloy of samarium and cobalt. Formed by powder metallurgical processes their magnetic performance is optimised by applying a magnetic field during the pressing operation, thus producing a preferred direction of magnetisation. They were chosen for this application due to their high magnetic fields, lightweight and for their thermal stability. They have operating temperatures up to 350˚C and excellent corrosion resistance without the need for any additional coating [9].

Introducing a magnetic bias of 500 Oe (40 kA/m) did not move the sensor operating point into the most linear region as can be seen from Figure 5-2. A more linear operating range would have been achieved if a magnetic bias of 2000 Oe (160 kA/m) had been applied. However, this would have resulted in the sensor being less sensitive to changes in current and a reduced operating range since the operating point would have been closer to the saturation point of the magnetostrictive material.

## 6.4 Methods of Reducing Hysteresis

A number of methods of reducing the hysteresis inherent in the sensor were reviewed as part of this research. The two main methods considered are discussed within this section.

### 6.4.1 Prestress

One method investigated of reducing the inherent hysteresis in magnetostrictive materials is through the application of a mechanical compressive stress. This stress, termed prestress, is applied to the material sample prior to the magnetic field and serves to further align the magnetic domains within the material [4].

An initial compressive stress is often used to increase the alignment of magnetic moments along the easy axis perpendicular to the applied magnetic field. Thus, when a magnetic field is applied in the direction of the applied stress, the resulting magnetostriction is larger in magnitude than if the prestress had not been applied [10]. This is illustrated in Figure 6-6.

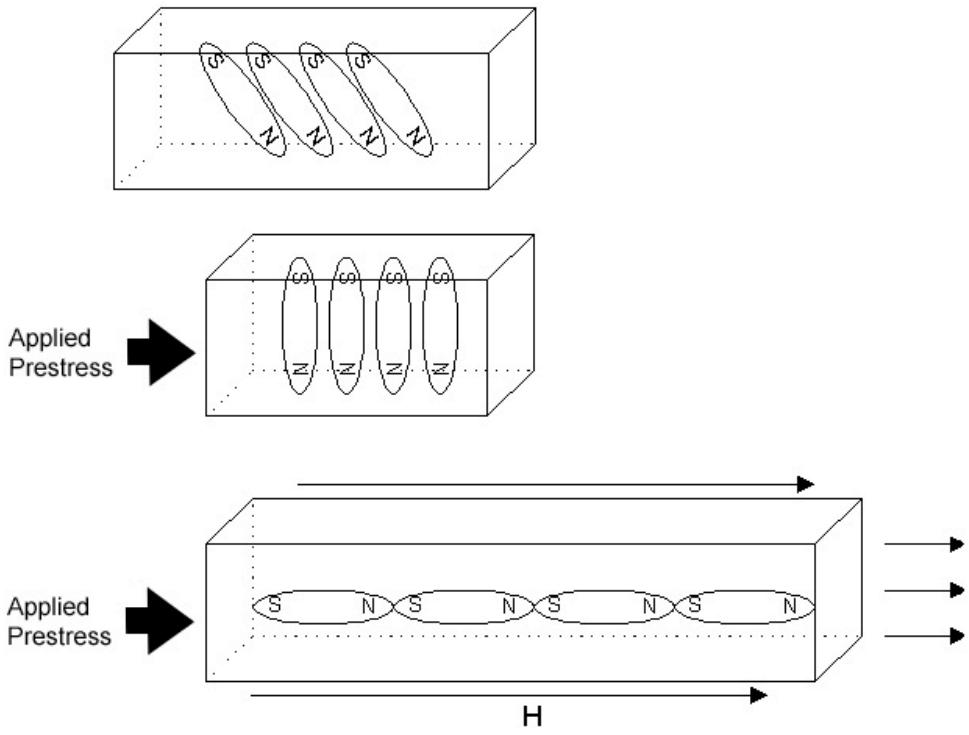


**Figure 6-6: Effects of magnetic field, H on magnetostrictive material under prestress**

The application of an adequate prestress is capable of improving the magnetic state in the material as a result of the coupling between the magnetic and mechanical states. The mechanical energy in the form of the prestress is an additional source of anisotropy energy which competes against the magnetocrystalline anisotropy, strain and applied field energies. The application of a prestress forces a large number of magnetic domains to align perpendicular to the direction of the prestress, where a state of local minimum energy is reached.

This does not serve to increase the saturation length of the magnetostrictive material, but does decrease the samples zero field length, thereby maximising the net available strain due to an increase in the rotation angle of the moments. This is also used to make the material behaviour repeatable, as without a prestress the initial magnetisation orientation is unknown. Therefore, applying a sufficient prestress to the magnetostrictive material is critical such that when the magnetic field is removed, the magnetisation will return to a known "rest" state. For Terfenol-D, Clark *et al* (1988) theoretically calculated this stress to be approximately 5 MPa based on anisotropy energy [11].

Several authors have conducted work in this area covering a range of applied stresses. Some of the most relevant papers are summarised below.

In [12] Calkins, Dapino and Flatau (1997) looked at both the effect of prestress and magnetic bias on Terfenol-D rods. The range of prestress used was 3.49 - 10.34 MPa. In this research trends in the properties with prestress and drive levels are indicated.

In [13] Cullen, Hathaway and Clark (1997) carried out mathematical calculations to determine what rate of prestress would result in overcoming the hysteresis effect in magnetostrictive materials. They studied a method of applying stress along certain symmetry axes in a manner that ensures continuous rotation of domain magnetisation as a magnetic field is applied along the same axis. They concluded that the minimum value of prestress capable of achieving this was 65 MPa. It was reported that when compressed in this manner, the magnetostrictive material would still expand (elongate) when placed in a magnetic field. However, it was stated that under this level of prestress the expansion would not be free. The mathematical theory of Cullen *et al* has yet to be proven with laboratory experiment.

Although no experiments have been carried out as part of this research to experimentally prove or disprove Cullen *et al* theory on eliminating hysteresis under a 65 MPa prestress, some initial calculations were carried out. This will be discussed in section 8.1.1.

The most widely used technique for applying a prestress to material samples involves the use of a prestress housing. An example design of a prestress housing can be seen in Figure 6-7 [14]. There are several different designs which can be used, with the most important feature being the prestress mechanism. The example prestress mechanism shown in Figure 6-7 [14] consists of a spring washer in series with a Terfenol-D rod. The prestress can be varied with the prestress (compressive) bolt which pushes the rod into the washer. The magnetostrictive material rod is constructed so that the magnetic moments are primarily oriented perpendicular to the longitudinal axis. The prestress mechanism can then be used to further increase the number of perpendicular moments and compression in the rod.

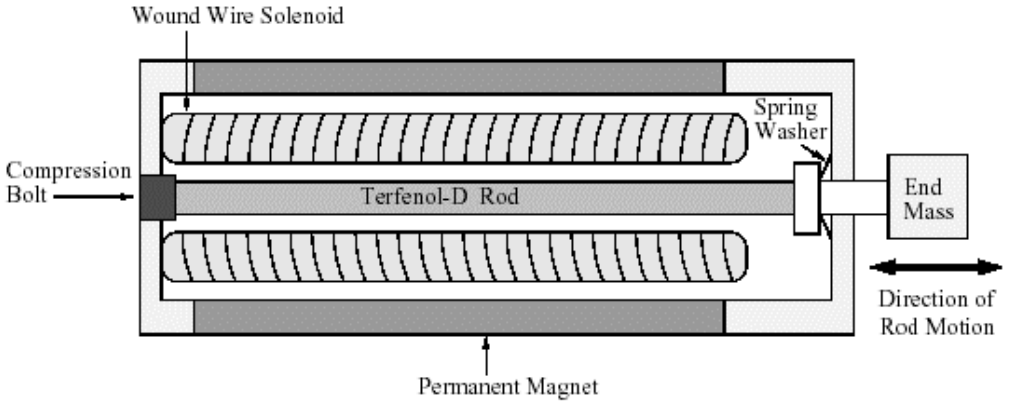


**Figure 6-7: Example prestress housing**

While extensively used in magnetostrictive transducer design research, the prestress housing design shown above is not appropriate for use with the sensor developed within this work. It was designed for a magnetostrictive actuator and would be difficult to adapt for a material sample bonded to an FBG. If the sensor were to be placed under a prestress, care would have to be taken not to damage the attached optical fibre.

### 6.4.2 Addition of a Fourth Element to the Material Stoichiometry

Another method investigated for reducing hysteresis loss in $Tb_xDy_{1-x}Fe_y$ magnetostrictive alloys, is through the introduction of a fourth element to the material

stoichiometry. One element which has been suggested for this purpose is Holmium, Ho. Holmium is a rare-earth element like terbium and Dysprosium. However, it has a much smaller saturation magnetostriction than either Tb or Dy, thus the addition of Ho reduces the magnetostriction of the alloy [15].

The substitution of Ho for Tb and Dy in the magnetostrictive alloy Terfenol-D and the corresponding changes in crystalline anisotropy and magnetomechanical coupling have been studied in the past.

Research conducted by Wun-Fogle, Restorff, and Clark, 1999 [16], in this area has shown that by substituting small amounts of Ho for Fe in Terfenol-D, the magnetocrystalline anisotropy can be lowered leading to reduced hysteresis loss. It also demonstrated that compared to magnetostrictive materials such as Terfenol-D, alloys containing Holmium can have lower hysteresis with only slightly lower magnetostriction.

Their studies were confined to very small concentrations of Ho in order to avoid a substantial decrease in magnetostriction. Figure 6-8 [16] shows two graphs taken from this research. The top graph shows hysteresis width, $W_h$ plotted against percentage Ho concentration, while the lower graph shows the resulting magnetostriction, or peak-to-peak strain $S_{pp}$, against the same Ho concentration axis. Both graphs show the results of Wun-Fogle *et al* research for a magnetostrictive material under 22 MPa prestress denoted by the red square and 47 MPa denoted by the blue circle. The results determined that a magnetostrictive sample containing ~15 atomic percent Ho under a compressive prestress of 22 MPa experiences a ~15 percent decrease in hysteresis width with a minimal 3% loss of magnetostriction. For further details on this research the reader is referred to [15], [16].

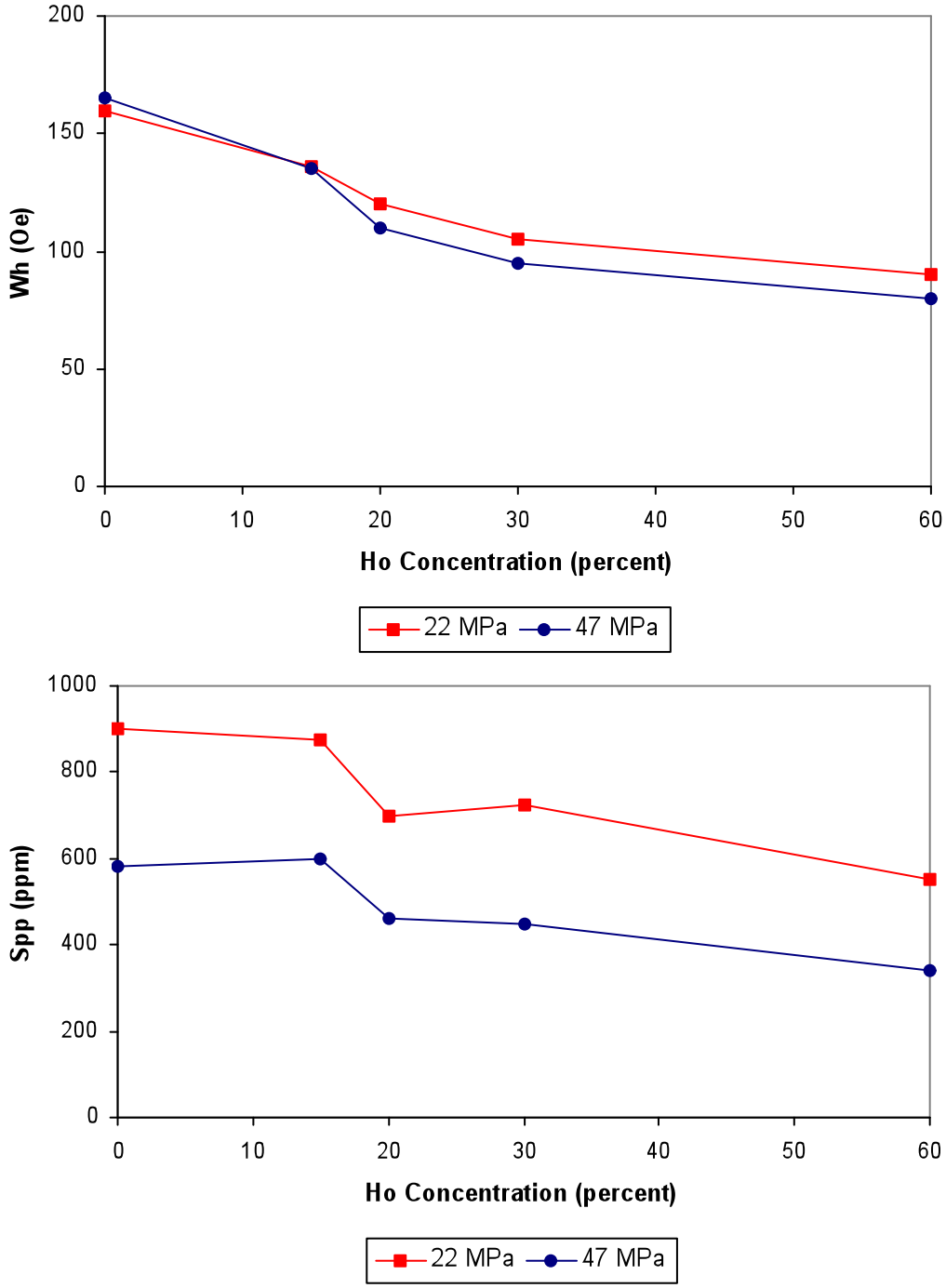


**Figure 6-8: Peak-to-peak strain $S_{pp}$ and hysteresis width $W_h$ vs concentration**

Although this research along with others shows improved properties over the original material composition, at the time of building the sensor it had yet to be seen if this material warranted sufficient interest to begin commercial production. Initial

enquires, conducted at that time, found that magnetostrictive alloys of this stoichiometry were not yet commercially available. Therefore, in order to use such a material in the sensor design it would have had to have been custom made. This was not deemed a viable option. This material termed Terfenol-DH has since become commercially available.

## 6.5 Correcting for Hysteresis

Following the previous section, where possible methods of reducing the hysteresis behaviour and other nonlinearities exhibited by the sensor were explored, this section will focus on possible methods of quantifying these effects or otherwise correcting for their contribution to the sensor's output characteristics.

Available mathematical models of hysteresis will be briefly reviewed to determine their suitability for use in correcting for the hysteresis exhibited by the sensors. The possibility of devising a computation routine or constructing a look-up table, and applying it to the sensor output will also be considered as a possible method of correcting the sensor output.

### 6.5.1 Mathematical Models of Hysteresis

In this section, a number of mathematical models of hysteresis, applicable to magnetostrictive materials, will be reviewed acknowledging the fact that the magnetostrictive effect is nonlinear due to the saturation effect and irreversible due to hysteresis.

It was found that the vast majority of hysteresis modelling in the literature is based on magnetic hysteresis not magnetostrictive hysteresis. The field of mathematical modelling of magnetostrictive hysteresis is a fairly young field with most models being developed in the last few years. The majority of these more recently adapted models concentrate largely on the identification and compensation of the hysteretic behaviour of magnetostrictive actuators. Since the majority of the magnetostrictive

actuators utilise Terfenol-D or materials of a similar chemical composition then it is likely that, if deemed useful, they can be adapted for application to the sensor design.

Mathematical models of hysteresis are largely classified into two categories: physical models and phenomenological models. Although research can also be found on models referred to as mixed-type models [17].

**Physical Models**

In physical modelling the magnetisation processes of ferromagnetic materials are simulated in order to understand the phenomena involved.

While several physical models of hysteresis have been described in the literature [18], [19], [20] it was found that most of these are based on Jiles-Atherton model; one of the most favoured physical model.

Jiles and Atherton introduced the Jiles-Atherton model for the simulation of hysteresis characteristic of ferromagnetic materials in 1983 [21] on the basis of the physical principles, rather than the mathematical arguments of experimental curves.

This is a physical model that provides a characterisation of the inherent hysteresis which is based upon the hysteretic magnetisation along with reversible and irreversible domain wall movements in the material. When coupled with nonlinear strain/magnetisation relations, this yields a model which characterises strain output in terms of input current to the coil. Minor loops are incorporated through the enforcement of closure conditions.

In [22], Jiles and Atherton (1984) describe a hysteresis model based on equilibrium thermodynamics and domain wall motion. Hysteresis is shown to occur as a result of impedances to magnetostriction changes such as when domain walls are pinned, while the mutual interactions of magnetic moments are shown to be of secondary importance. Results are presented which show all the features of hysteresis such as the

initial magnetisation curve, major and minor hysteresis loops in excellent agreement with static experimental results.

The Jiles-Atherton theory is often preferred over the other physical model available, because it can be relatively easily implemented. Moreover it requires little memory storage and the following five physical parameters are all that are needed for complete description of the magnetic state of a material:

$M_s$ the spontaneous magnetisation
K pinning coefficient
α interactions between domains
a thermal aspect (domain wall density)
c reversible magnetisation component

The ability to calculate the hysteresis parameters from a set of experimental data is a key step in the process of utilisation of this hysteresis model. A number of authors have proposed methods of determining these parameter [23-30].

In [23] Wang, Thomas, Sumner and Cabral (2009) propose a method of estimating these five parameters of ferromagnetic hysteresis by fitting the model to symmetrical hysteresis loops through curve fitting and numerical optimised iteration. The performance of the method is evaluated by both theoretical and experimental data. Jiles and Thoelke (1989) [24] have described how the parameters can be calculated from the anhysteretic susceptibility at the origin, the coercivity, the remanence and the coordinates of the hysteresis loop tip. They developed algorithms capable of determining the parameters to within a few percent in most cases. However, convergence problems may be encountered in the identification of these parameters by using iterative procedures [24], [25].

Many researchers have proposed a number of other methods by which these parameters can be determined such as generic algorithms (GA) [26], nonlinear least-square method [27], false position method [28], particle swarm optimisation (PSO)

[29], random and deterministic searches [30], as well as direct search method [31] among others. Each of these methods has their own applicability domain and constraints.

**Phenomenological Models**

In phenomenological modelling, mathematical functions are sought that fit the experimental data. These models are computationally more efficient than physical models but give no insight into the physical processes involved. While the scientific scope of most of these models is limited, they can be useful in engineering, where the physics behind the material behaviour is of secondary importance.

Several phenomenological models exist for hysteresis including Preisach modelling, first-order reversal curve analysis (FORC) [32], Barkhausen analysis and micromagnetic mean-field modelling. Of those available the Preisach model is the most widely used.

The Preisach model is one of the earliest hysteresis models; presented in 1935 by F. Preisach [33]. Since then, it has become a widely accepted model of hysteresis. It is used to represent the magnetic properties of a material for magnetisation as a function of field. It does not give much physical insight into the magnetic properties of the material. It is a complicated curve-fitting procedure, which has been shown to give a reasonable mathematical representation of hysteresis curves once the curves are already known.

The Preisach model is empirical in that it can be used to mathematically represent hysteresis curves in terms of shape parameters determined through least squares fits to experimental data. Since the model contains no physics specific to a certain area, it can be used to model dynamics in which the underlying physics is not thoroughly understood and therefore it is applicable to a broad range of phenomena that exhibit hysteresis, for example AFC Magnetic Recording Media [34] and Soil-Moisture Hysteresis [35].

The use of Preisach techniques for characterising general magnetic hysteresis is well established in the literature [36-39] and some aspects have been extended to magnetostrictive materials [40 - 43]. Mayergoyz explained this model in detail in [44] and many variations of this model have been developed.

The idea behind the Preisach model is that the observed bulk magnetic hysteresis loop of a material is due to a summation of more elementary hysteresis loops of domains with differing switch fields or coercivities. These domains can only have two states within the confines of the model, with magnetisation parallel or antiparallel to a given direction. The model relies on a density function called the Preisach function which is defined on a plane described by the positive and negative fields $H_+$ and H-. This function is used to determine how many domains switch their orientation from +ve to -ve, or vice versa, as the field is swept between limiting values of magnetic field H.

The model supposes an infinite number of generic elements with hysteresis that have outputs of only ± 1. There are various forms of the model in use. Following the Mayergoyz notation each of the elements are denoted as $\gamma(\alpha,\beta)$. As the input is increased, the element switches from –1 to +1 as the input value reaches $\alpha$ and switches from +1 to –1 the input decreases to $\beta$ (Figure 6-9). A continuous distribution of elements with various $\alpha$'s and $\beta$'s is assumed with the restriction that $\alpha>\beta$. In order to find the output value, the elements are summed with a weighting function $\mu(\alpha,\beta)$. It is the weighting function that contains the desired information.

The problem is to determine which elements have output of +1 and which elements have output of –1 when the model is interrogated. In order to obtain this information, the model is required to maintain a history of the magnetic field applied in order to predict the system's response to a given magnetic field. This history takes the form of two lists that record the local minimums and maximums of the input. In theory, this list could grow without limit. In practice, however, this does not happen since the list is truncated whenever a minimum lower than the lowest previous minimum or a

maximum higher than the highest previous maximum occurs. For example, when the input saturates the sample, the list has a length of one regardless of the previous history.

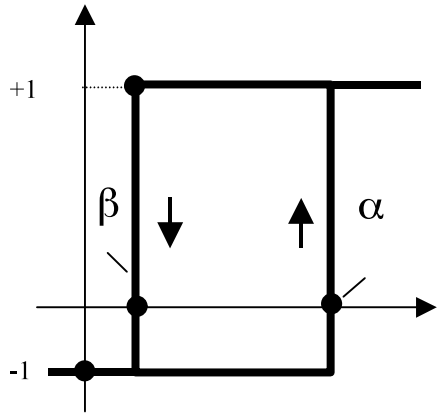


**Figure 6-9: A generic element exhibiting hysteresis**

Since the Classical Preisach model was proposed, phenomenological modelling of hysteresis has continued to develop. Various modifications of the model have been and continue to be suggested. Many of which have lead to substantial enhancement of the model stability and of the accuracy with which the magnetic properties of various materials can be represented: namely, Krasnoselskii and Pokrokovskii [45], and Mayergoyz [46].

This section is not intended to be a comprehensive description of mathematical models of hystersis due to the wide range of research being conducted in this area. For more theoretical models of hysteresis, the reader is refered to Visintin [47], Mayergoyz [46] , Krasnoselskii and Pokrovskii [45] or Brokate [48].

### 6.5.2 Computation Routine or Lookup Table

Another approach to correcting for the hysterisis and nonlinear response of the sensor is through the use of a computation routine or lookup table. The principle behind these correction methods is briefly described in this section.

The relationship between the input optical signal and the desired output signal (obtained from the reference measurement) can either be expressed as a single function, set of functions or as a series of data points in a look-up table.

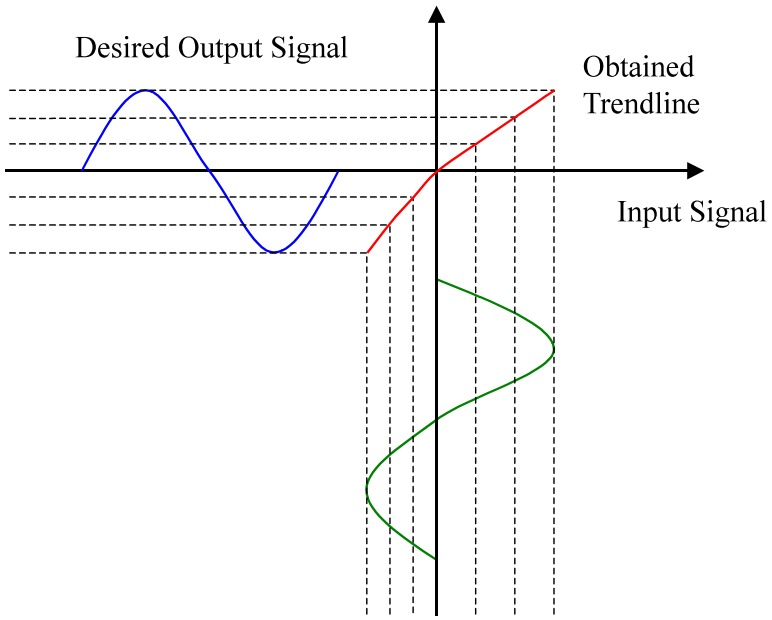


**Figure 6-10: Relationship between Input and Output Signals**

Figure 6-10 illustrates one method through which this relationship could be determined. Each input point is related to corresponding output point. A best-fit trendline can be drawn through these points. If the trendline is easily described by a simple function then this function can be used to convert all the input data into the correct output signal. There are many statistical computing packages available to aid in this process.

If no suitable function exists to describe the relationship, then a set number of points are stored in a look-up table. Each input point is then cross-referenced to a stored output point. In the simplest examples of look-up tables, the closest stored input point to the actual input point will be used, and its corresponding stored output point will be the system output. This means that the system measurement resolution

can only be as small as the step-size between the points stored in the table. In more complex systems, interpolation between the stored input and output points will take place and a more accurate system output will result.

## 6.6 Proposed Signal Processing Method

In this chapter, an overview of possible methods of reducing or correcting for the sensor's inherent hysteresis and nonlinear response was provided. Of the methods described it was decided that the statistical computation approach would be developed further.

This approach was chosen as the preferred solution since it was discovered through experiments conducted on the sensor that the main effects on the optical signal that required correction through signal processing are the nonlinearity and thermal effects. It was experimentally proven that errors introduced by the hysteresis had a lesser impact on the sensor output in comparison.

Furthermore, during the experimental process, relationships were discovered that made it possible to recover both current and temperature from the sensor output signal. The experimental data, taken over a specific test range, was entered into the Statistics package R to enable general linear models of the data to be computed. R is a programming language and software environment for statistical computing and graphics and was chosen for use because it's widely accepted in business and academia and free to use. For more information on R, the reader is referred to [49], [50].

It was found that the statistical computational approach could provide a simple and reliable solution to correct for the sensor's nonlinearities over the test range. Moreover, since this method of signal process utilises only the peak-to-peak and average wavelengths, the results obtained from this signal processing method are unaffected by the effects of hysteresis. This approach will be discussed further in a later chapter.

From this initial review, it was also decided that some more preliminary research would be conducted into the effects of prestress on the magnetostrictive material. As a result, a prestress housing was designed and built as part of this research to facilitate any experiments, as part of future work, into this area.

## 6.7 Chapter References


[1] Hansen, T. T., "Magnetostrictive materials and ultrasonics," CHEMECH, Vol. 26, Issue 8, American Chemical Society, August 1996, pp.56-59.

[2] Jiles, D., "Introduction to Magnetism and Magnetic Materials," Second Edition, Chapman and Hall, 1998.

[3] Craik, D., "Magnetism – Principles and Applications," Wiley, 1995.

[4] Cullen, J. R., Hathaway, K.B., Clark, A.E.,"Critical behaviour of cubic magnetostrictive materials under stress," Journal of Applied Physics, Vol. 81, Issue 8, April 1997, pp.5417-5419.

[5] Asti, G., Rinaldi, S., Proceedings of the Third European Conference on Hard Magnetic Materials, Amsterdam, 1974, pp.302.

[6] Mukamel, D., Fisher, M., Domany, E., "Magnetization of cubic ferromagnets and the three-component Potts model," Physical Review Letters, Vol. 37, Issue 10, 1976, pp.565-568.

[7] Singh, D. J., Papaconstantopoulos, D. A., "Electronic Structure and Magnetism of Complex Materials," Springer, 2003.

[8] MaTeck GmbH Website - http://www.mateck.de

[9] Metall Advanced Magnets Limited Website – http://www.mamag.com.cn/mag/smcol.htm

[10] Dapino, M.J., Flatau, A.B., Calkins, F.T., "Statistical analysis of Terfenol-D material properties," Journal of Intelligent Material Systems and Structures, Vol.17, No.7, 2006, pp. 587-599.

[11] Clark, A. E., Teter, J.P., McMasters, D., "Magnetostriction "jumps" in twinned $Tb_{0.3}$ $Dy_{0.7}$ $Fe_{1.9}$," Journal of Applied Physics, Vol. 63, Issue 8, 1988, pp.3910-3912

[12] Calkins, F. T., Dapino, M. J., Flatau, A. B., "Effect of Prestress on the Dynamic Performance of a Terfenol-D Transducer," SPIE 1997, Proceedings on Smart Structures and Materials, Paper #3041-23, 3/97.

[13] Cullen, J. R., Hathaway, K. B., Clark, A. E., "Critical behaviour of cubic magnetostrictive materials under stress," Journal of Applied Physics, Vol. 81, No. 8, April 1997, pp.5417-5419.

[14] North Carolina State University, Multifunctional Materials Group Website – http://www.ncsu.edu

[15] Restorff, J.B., Wun-Fogle, M., "Temperature and Stress Dependency of the Magnetostriction in Tertiary and Quaternary Terfenol Alloys," Journal of Applied Physics, Vol.87, Issue 9, May 2000, pp.5786-5788.

[16] Wun-Fogle, M., Restorff, J. B., and Clark, A. E., "Hysteresis and Magnetostriction of $Tb_xDy_yHo_{1-x-y}Fe_{1.95}$ [112] Dendritic Rods, "Journal of Applied Physics, Vol. 85, Issue 8, April 1999, pp. 6253-6255.

[17] Stancu, A., Păpusoi, C., Spĭnu, L., "Mixed-type Models of Hysteresis," Journal of Magnetism and Magnetic Materials, Vol. 150, Issue 1, September 1995, pp.124-130.

[18] Calkins, F.T., Smith, R.C., Flatau, A.B., "An Energy-based Model for Magnetostrictive Transducers," IEEE Transactions on Magnetics, Vol. 36, Issue 2, March 2000, pp.429-439.

[19] Zheng, X., Sun, L., "A one-dimension coupled hysteresis model for giant magnetostrictive materials," Journal of Magnetism and Magnetic Materials, Vol. 309, Issue 2, February 2007, pp263-271.

[20] Zheng, J., Cao, S., Wang, H., "Modelling of magnetomechanical effect behaviour in a giant magnetostrictive device under compressive prestress," Sensors and Actuators A: Physical, Vol. 143, No. 2, May 2008, pp.204-214.

[21] Jiles, D. C., Atherton, D. L., "Ferromagnetic Hysteresis," IEEE Transactions on Magnetics, Vol. MAG-19, No. 5, September 1983, pp.2183-2185.

[22] Mayergoyz, I.D., "Mathematical Models of hysteresis and their Applications," Elsevier Academic Press, 2003.

[23] Wang, X., Thomas, D.W.P., Sumner, M., Paul, J., Cabral, S.H.L., "Numerical determination of Jiles-Atherton model parameters, " COMPEL: The International Journal for Computation and Mathematics in Electrical and Electronic Engineering, Vol. 28, Issue 2, 2009, pp.493-503.

[24] Jiles, D., Thoelke, J., "Theory of ferromagnetic hysteresis: determination of model parameters from experimental hysteresis loops, " IEEE Transactions on Magnetics, 1989, pp.3928-3930.

[25] Jiles, D., Thoelke, J., Devine, M., “Numerical determination of hysteresis parameters for the modelling of magnetic properties using the theory of ferromagnetic hysteresis,” IEEE Transactions on Magnetics, Vol. 28, January 1992, pp.27-35.

[26] Chwastek, K., Szczyglowski, J., “Mathematics of a hysteresis model parameters with genetic algorithms,” Mathematics and Computers in Simulation, Vol. 71, Issue 3, May 2006, pp.206-211.

[27] Kis, P., Iványl, A., “Parameter identification of Jiles-Atherton model with nonlinear least-square method,” Physica B: Physics of Condensed Matter, Vol. 343, Issue 1-4, Proceedings of the Fourth International Conference on Hysteresis and Micromagnetic Modeling, January 2004, pp.59-63.

[28] Hamimid, M., Felliachi, M., Mimoune, S.M., “Modified Jiles-Atherton model and parameters identification using false position method,” Physica B: Physics of Condensed Matter, Vol. 405, Issue 8, April 2010, pp.1947-1950.

[29] Marion, R., Scorretti, R., Siauve, N., Raulet, M. A., Krähenbühl, L., “Identification of Jiles-Atherton model parameters using Particle Swarm Optimization,” IEEE Transactions On Magnetics, Vol. 44, No. 6, June 2008, pp.894-897.

[30] Del Moral Hernandez, E., Muranaka, C.S., Cardoso, J.R., “Identification of the Jiles-Atherton model parameters using random and deterministic searches,” Physica B: Physics of Condensed Matter, Vol. 275, Issue 1-3, January 2000, pp.212-215.

[31] Chwastek, K., Szczyglowski, J., Najgebauer, M., “A direct search method for estimation of the Jiles_Atherton hysteresis model parameters,” Material Science and Engineering: B, Vol. 131, Issues 1-3, July 2006, pp.22-26.

[32] Pike, C.R., “First-order reversal-curve diagrams and reversible magnetization,” Physical Review B, Vol. 68, Issue 10, September 2003, pp.104-109.

[33] Preisach, F., “Uber die magnetische Nachwirkung,” Zeitschrift fűr Physik, Vol. 94, 1935, pp.277-302.

[34] Ktena, A., Fotiadis, D.I., Berger, A., Massalas, C. V., "Preisach Modeling of AFC Magnetic Recording Media," IEEE Transactions on Magnetics, Vol. 40, No. 4, 2004, pp.2121-2130.

[35] Flynn, D., McNamara, H., O'Kane, P., Pokrovskii, A., "Application of the Preisach model in soil-moisture hysteresis," The American Geophysical Union, Abstract No.H22J-06, 2003.

[36] Charap, S.H., Ktena, A., "Vector Preisach Modelling," Journal of Applied Physics, Vol. 73, Issue 10, May 1993, pp. 5818-5823.

[37] Torre, E.D., "Energy Considerations in Hysteresis Models," IEEE Transactions on Magnetics, Vol. 28, Issue 5, September 1992, pp. 2608-2610.

[38] Adly, A.A., Mayergoyz, I.D., "A New Vector Preisach-Type Model of Hysteresis," Journal of Applied Physics, Vol.73, Issue 10, May 1993, pp. 5824-5826.

[39] Visintin A., Differential Models of Hysteresis, Springer-Verlag, New York, 1994.

[40] Adley, A.A., Mayergoyz I.D., Bergqvist, A., "Preisach Modeling of Magnetostrictive Hysteresis," Journal of Applied Physics, 69, Issue 8, 1991, pp. 5777-5779.

[41] Bergqvist, A., Engdahl, G., " A Phenomenological Magnetomechanical Hysteresis Model," Journal of Applied Physics, Vol. 75, Issue 10, 1994, pp.5496-5498.

[42] Natale, C., Velardi, F., and Visone, C., "Identification and compensation of Preisach hysteresis models for magnetostrictive actuators," Physica B: Physics of Condensed Matter, Vol. 306, Issues 1-4, December 2001, pp.161-165.

[43] Smith, R.C., "Hysteresis Modeling in Magnetostrictive Materials via Preisach Operators," Institute for Computer Applications in Science and Engineering, NASA Contractor Report 201695, ICASE Report No. 97-23, May 1997

[44] Mayergoyz, I. D., "Mathematical Models of Hysteresis and their Applications," Elsevier Academic Press, Amsterdam, Boston, 2003.

[45] Krasnoseliskii, M., Pokrovskii, A.,"Systems with Hysteresis", Springer-Verlag, 1989.

[46] Mayergoyz, I.D., "Mathematical Models of Hysteresis", Springer-Verla, 1991.

[47] Visintin, A., “Differential Models of Hysteresis”, Springer-Verlag, 1991.

[48] M. Brokate, “Hysteresis and Phase Transitions”, New York: Springer, 1996.

[49] Hornick, K., “The R FAQ,” 2010, ISBN: 3-900051-08-9, www.cran.r-project/doc/FAQ/R-FAQ.html

[50] The R Project for Statistical Computing website – www.r-project.org

# 7 Sensor Design

This section looks at the sensor proposed within this research: details of the sensor fabrication and operation are given along with advantages and limitations of the sensor design.

## 7.1 Sensor Fabrication

The sensor element consists of an FBG, bonded using epoxy resin to a piece of magnetostrictive material. Epo-Tek 353ND heat curing epoxy resin was used for this purpose. This specific epoxy was chosen because it is designed for use in high temperature applications [1]. It has been proven to perform continuously at 200ºC and can endure temperatures of 300~400ºC for several minutes. It has excellent resistance to many types of solvents and chemicals and is ideal for bonding fibre optics, metals, glass, ceramics and most plastics [2]. Since Epo-Tek 353ND remains liquid until heat is applied, the bond was effected using heat treatment. This was achieved by placing the components in an oven at 80°C for 4 hours.

The FBG utilised in the sensor design was written in a single mode fibre at a peak wavelength of 1547.5 nm at room temperature. The sensor element was enclosed in an aluminium housing which also allowed small samarium cobalt magnets to be located near the sensor for biasing purposes, this will be discussed in greater detail in Chapter 8. The housing was designed to fit inside a plastic bobbin, around which 1280 turns of 19 SWG, 1 mm enamelled copper wire were wound. Figure 7-1 shows the schematic of the sensor set-up.

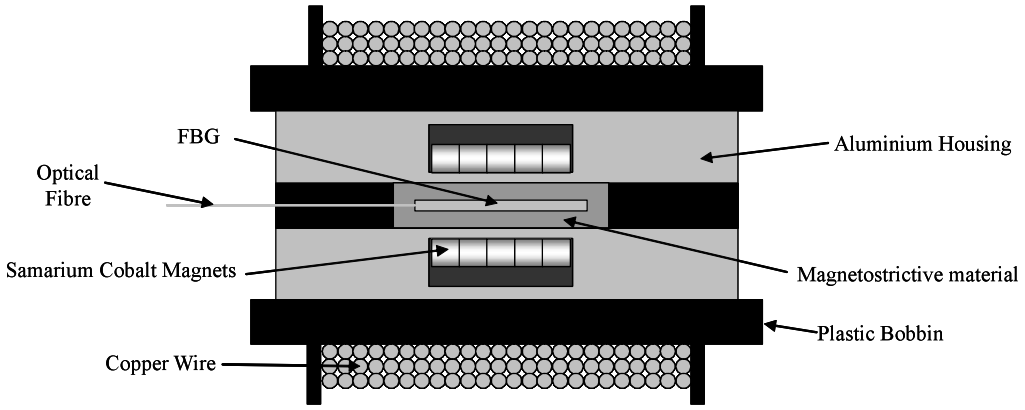


**Figure 7-1: Sensor set-up**

## 7.2 Sensor Operation

The sensor works on the principle that the current to be measured induces a magnetic field in a wound wire coil. As the current varies, the magnetic field also varies, causing the biased magnetostrictive material inside the coil to elongate or contract. This in turn applies strain to the FBG, causing a shift in the period, $\Lambda$. The wavelength of the FBG will therefore change with the magnetic field, which can be interpreted by the interrogation system as a change in the current.

The strain response element of the FBG will be utilised within the sensor in order to facilitate the measurement of current. However, as discussed in Section 4.2 changes in temperature also have an effect on the stain induced in the FBG.

At this point, it is worth looking at the ways in which temperature variations can affect the sensor. These are described below:

- Thermal expansion of the magnetostrictive material will produce an additional elongation, unrelated to the magnetic field, which will produce an additional strain in the grating.

- The refractive index of the grating varies significantly with temperature, producing a change in the Bragg wavelength unrelated to the strain which the grating is under, and therefore the magnetic field.

- Thermal expansion of the grating has a relatively small effect on the Bragg wavelength. Most references combine the wavelength changes due to the change in refractive index and the change due to thermal expansion into a single coefficient of proportionality, normally about $6.67\times10^{-9}$ m $^{o}C^{-1}$.

Therefore care will have to be taken to ensure that effects of temperature are decoupled from the current measurement. The temperature at the sensing point can be determined through averaging of the sensor output signal.

## 7.3 Advantages of Sensor Design

The main advantages of the sensor design stem from the use of an FBG based optical fibre sensor. Optical fibre sensors offer many advantages over conventional sensors such as their inherent high voltage insulation, chemically inert nature and intrinsically safe mode of operation as well as their small physical size and light weight. These advantages will be particularly useful when such as a sensor is utilised within an ESP.

Additional benefits of using wavelength encoded fibre sensors included their immunity to source fluctuations, enhancement in signal bandwidth and dynamic range, and the ease with which they can be multiplexed.

In addition to the advantages associated with FBG sensors, the sensor described in this thesis is capable of measuring alternating current magnitude, while allowing the measurement of the temperature at the sensor head using a single FBG. The principle benefit of being able to measure both measurands simultaneously and at precisely the same location is the ability to decouple the effects of temperature from the current measurement. The main advantage of using a single FBG is the cost savings and reduced optical bandwidth requirements.

## 7.4 Technology Limitations

The range of the sensor is limited by the saturation point of the magnetostrictive material. Magnetic fields which are greater than those required to induce saturation cannot be unambiguously resolved.

The resolution of the sensor is determined by the minimum wavelength shift that the interrogation system can discern. This will relate to a minimum strain in the sensor and therefore a minimum current. The magnetic field produced by the current in the conductor decreases in intensity as the distance of the sensor from the conductor increases. It follows that, by locating the sensor at a further distance from the conductor, greater magnitudes of current can be measured. However, this will also adversely affect the resolution of the system as the strain, and therefore the wavelength shift, will be lower for a given current.

Since the motor used to drive an ESP is typically a three phase, squirrel cage induction motor [3], the sensor system will require three current sensors; one per phase. Although each of the three sensors will be assigned to measure a particular phase, magnetic crosstalk from the other phases may occur. The extent of the crosstalk will partially depend on the relative positions of each of the sensors in relation to the conductors. It may not be possible, therefore to easily locate the sensor further from the conductor without severe crosstalk effects.

Temperature will have an effect on the system in terms of thermal expansion of the magnetostrictive material, thermal expansion of the silica fibre and change in refractive index of the Bragg gratings. These effects will have to be decoupled from the current measurement signal.

## 7.5 Chapter References

[1] Epo-Tek® 353ND High Temperature Epoxy Technical Data Sheet – http://www.epotek.com/SSCDocs/datasheet/MSDS/353ND_msds.pdf

[2] Precison Fiber Products website – http://www.precisionfiberproducts.com

[3] Takacs, G., "Electrical Submersible Pumps Manual: Design, Operations, and Maintenance," Gulf Professional Publishing, 2009.

# 8 Prestress Housing Design

It was found that one method of reducing the inherent hysteresis in the current sensor was to apply a prestress to the magnetostrictive material sample. Prestress was discussed in Section 6.4.1. It was decided at an early stage in the sensor design that a prestress housing should be designed not only to allow prestress experiments to be carried out at as part of future work, but also as a housing for the sensor. The use of a prestress housing would also have an impact on the coil design.

The housing design had to take into consideration that all four sides of the magnetostrictive material could not be tightly enclosed, because the fibre containing the FBG is bonded to one side. The design had to achieve this as well as minimising the chances of the material sample buckling under the compression.

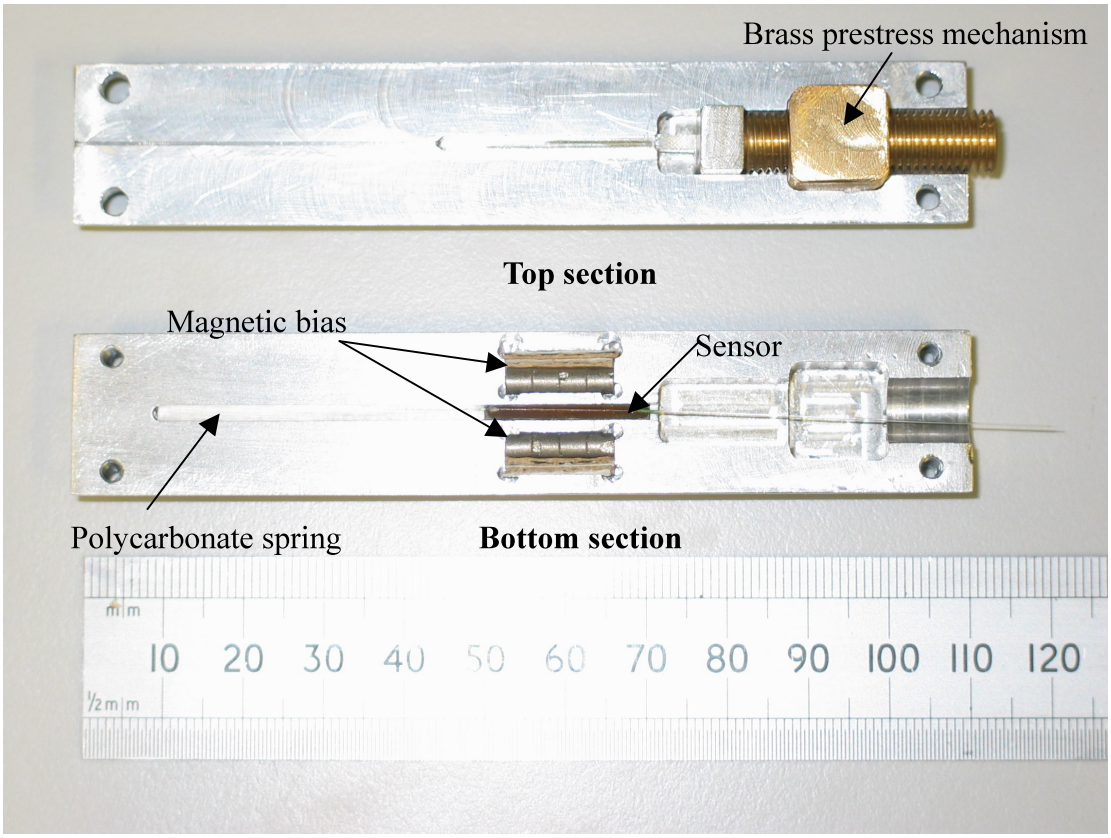


**Figure 8-1: Prestress housing**

The prestress housing was designed to facilitate the application of compressive stresses of up to 65 MPa in order to enable the calculations by Cullen *et al* [1] to be experimentally proven as part of future research.

The prestress housing, a photograph of which can be seen in Figure 8-1, consists of a halved, 20 mm diameter aluminium rod so the sensor can be placed inside the two halves. Aluminium was chosen because of its neutral magnetic properties to avoid unnecessary interference with the magnetic fields and because of its relatively lightweight.

The prestress mechanism is constructed from brass and, instead of a spring washer, a length of polycarbonate is used as a spring. Polycarbonate was chosen for its high modulus of elasticity, low deformation under load, excellent strength retention at elevated temperatures and low coefficient of thermal expansion [2]. A suitable length of the polycarbonate spring was calculated as 30mm. This calculation was based on the application of a maximum compressive stress that the spring would experience as a result of 65 MPa of stress being applied to the magnetostrictive material. The additional stress that would be experienced from the expansion of the magnetostrictive material when subjected to a magnetic field was also calculated. These calculations can be seen in Appendix A.

Some material properties for polycarbonate are listed in the table below [2]:

| | |
|---|---|
| Density ($g/cm^3$) | 1.2 |
| Water Absorption, 24 hrs (%) | 0.12 |
| Young's Modulus (MPa) | 2206 |
| Compressive Strength (MPa) | 83 |
| Coefficient of Linear Thermal Expansion ($x\ 10^{-5}$ in./in./°F) | 3.9 |

**Table 2: Material properties for polycarbonate**

The bottom half of the aluminium rod shown above in Figure 8-1 was machined down the centre to a depth of 2 mm and width of 2 mm to allow space for the polycarbonate spring and magnetostrictive material sample. This machined section enclosed both the spring and material sample on three sides.

It was necessary to secure the fourth – top – side of the magnetostrictive material to stop it from buckling under the prestress, and to ensure that no damage was done to the optical fibre bonded to the upper side. A 0.4 mm grove was machined to route the optical fibre out of the housing. A drawing of the prestress housing can be seen in Appendix B.

Since prestress experiments were not conducted as part of this research, the effectiveness of the prestress mechanism and the polycarbonate rods ability to act as a spring have not yet been experimentally proven. Nor as yet, has the prestress housing been experimentally proven to be capable of applying a 65 MPa to the material sample.

### 8.1.1 Expected Sensor Sensitivity under Prestress

Although prestress experiments were not conducted as part of this research, to determine the sensor response when subject to a 65 MPa prestress, initial calculations were carried out to determine how the sensitivity of the sensor is expected to change under such a high compressive prestress.

From the calculations below, taking into consideration the range in which the material samples Young's modulus lies, the material's forecasted sensitivity was calculated.

The material sensitivity, S, can be determined using the following equation:

$$S = S^H T + dH \tag{15}$$

where

S is the strain;

$S^H$ is the elastic modulus measured with coil leads open circuit;

T is the mechanical stress (prestress);

d is the magnetostrictive "d" constant corresponding to the slope of the magnetostrictive strain as a function of magnetic field curve in Figure 5-2;

H is the magnetic field.

The following equation was used to determine $S^H$ :

$$S^H = \frac{1}{Y} \tag{16}$$

where

Y is the Young's Modulus of the material.

The value of Young's modulus for the material according to the manufacturers data, shown in Table 1, falls into a range as opposed to an exact value. Therefore the forecasted sensitivity of the material will also fall within a range of two values. Figure 8-2 shows the calculated sensitivity of the sensor under an applied compressive prestress of 65 MPa.

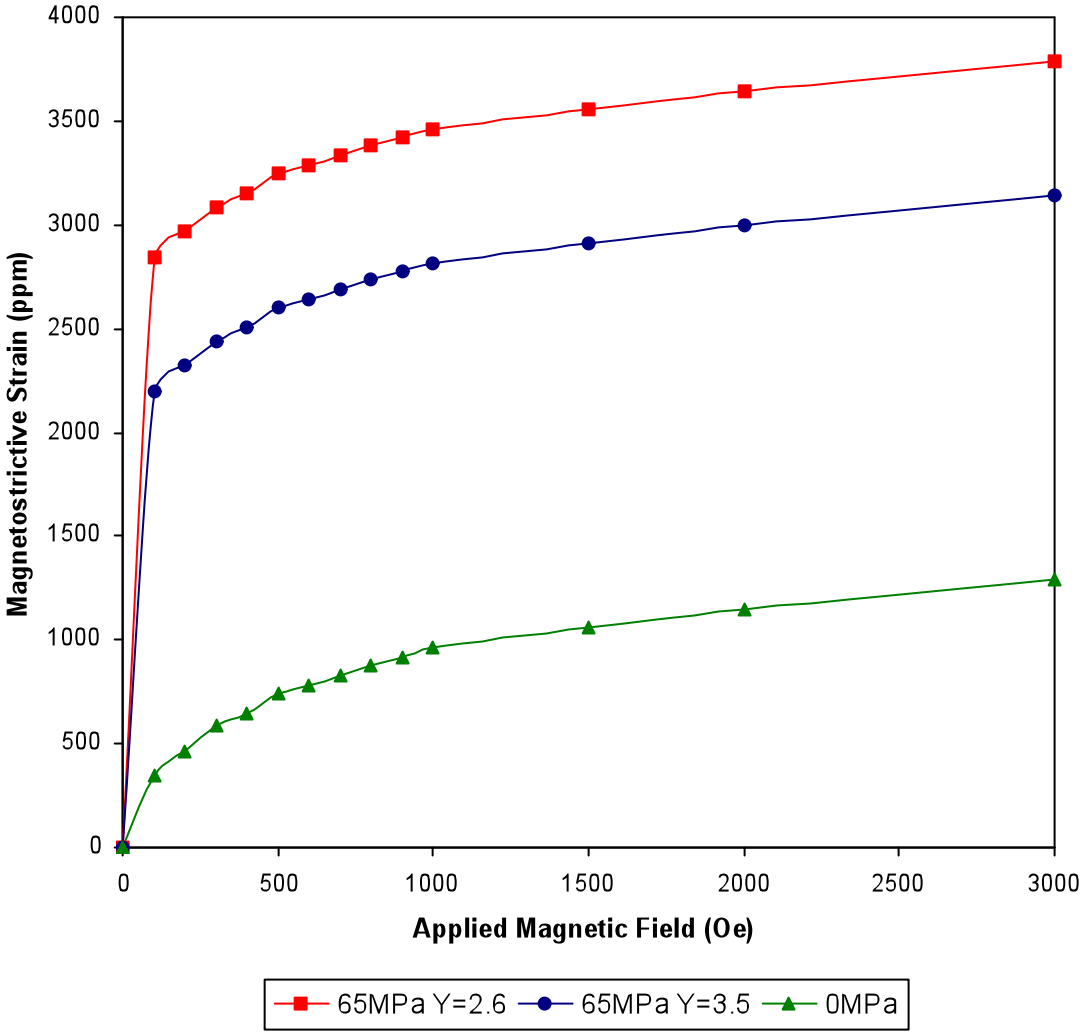


**Figure 8-2: Forecasted sensitivity of sensor under 65 MPa prestress (1)**

In Figure 8-2 the green line depicts the material's response with no applied prestress. Under the application of a 65 MPa prestress the materials actual response would lie somewhere in the region between the red and blue line.

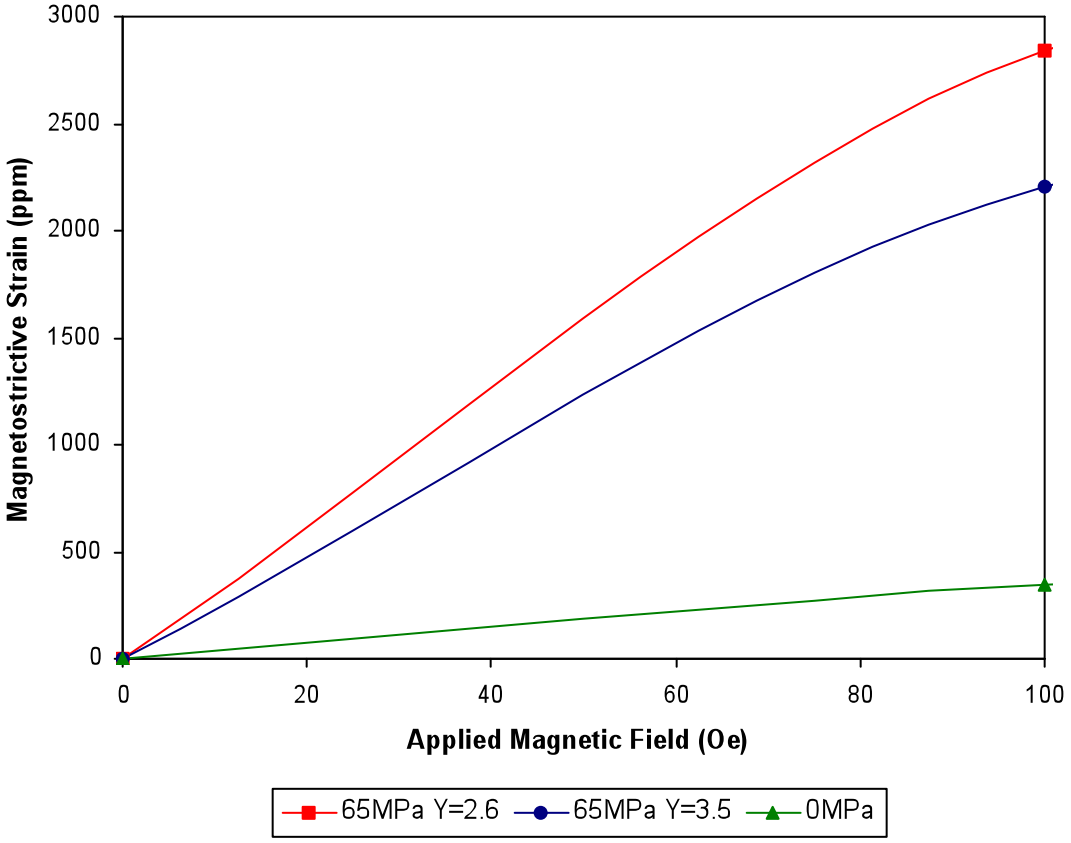


**Figure 8-3: Forecasted sensitivity of sensor under 65 MPa prestress (2)**

Looking more closely at the region of 0 to 100 Oe (Figure 8-3), it can be seen that the application of 65 MPa of compressive prestress would significantly increase the sensitivity of the material and thus the sensor.

## 8.2 Chapter References

[1] Cullen, J. R., Hathaway, K. B., Clark, A. E., "Critical behaviour of cubic magnetostrictive materials under stress," Journal of Applied Physics, Vol. 81, No. 8, April 1997, pp.5417-5419.

[2] http://www.boedeker.com/polyc_p.htm

# 9 Experimental Set-up and Sensor Interrogation

Throughout the experimental stage of this research two different experimental set-ups were used; one for the direct current (dc) experiments and another for the alternating current (ac) experiments. Both set-ups involved the use of a power supply, an interrogation system, a PC, a specially designed coil and the sensor.

In this section, both the experimental set-up and sensor interrogation systems used in the dc, and the ac experiments will be described. Details of the experimental coil design will also be discussed.

## 9.1 DC Experimental Set-up and Sensor Interrogation

For the initial dc experiments a Xantrex XHR 40-25 power supply was used and the input voltage was manually increased and decreased. A broadband light-emitting diode (LED) source was used to illuminate the FBG and a Micron Optics FBG-IS wavelength detector was used to measure the reflected wavelengths. A Micron Optics FBG-IS is a multi-sensor measurement system, specifically designed to simultaneously measuring up to 31 FBG sensors. The system combines the resolution of less than 1 pm of its Fibre Fabry-Perot Tunable Filter with the accuracy of the *pico*Wave® reference technique to resolve sub-picometer changes in optical wavelengths. It has a Scanning frequency of 52.4 Hz, a wavelength range of 1528-1568 nm, and can achieve 10 pm calibrated wavelength accuracy. It has standard software capable of collecting data and displaying wavelength information. However, there is also the option for the user to create custom interfaces with LabVIEW.

With a scanning frequency of 52 Hz this set-up proved to be insufficient for use in the 50 Hz ac current experiments. For these a scanning frequency of at least 100 Hz was required. With no such system available commercially at the time, it was necessary to build a custom-built interrogation system to obtain a sufficiently high scanning frequency.

In order to provide the means for characterising the sensor response to a 50 Hz ac current, a system was built in the laboratory as part of the Scottish Enterprise Proof of Concept Project. The interrogation system used, and described within the following section was designed by Grzegorz Fusiek as part of his PhD [1].

## 9.2 AC Experimental Set-up and Sensor Interrogation

The following experimental system was built in the laboratory (see Figure 9-1). A broadband super fluorescent source (SFS), with a 3 dB wavelength range of 1525 – 1565 nm, was used to illuminate the FBG through an optical coupler and the length of single mode optical fibre.

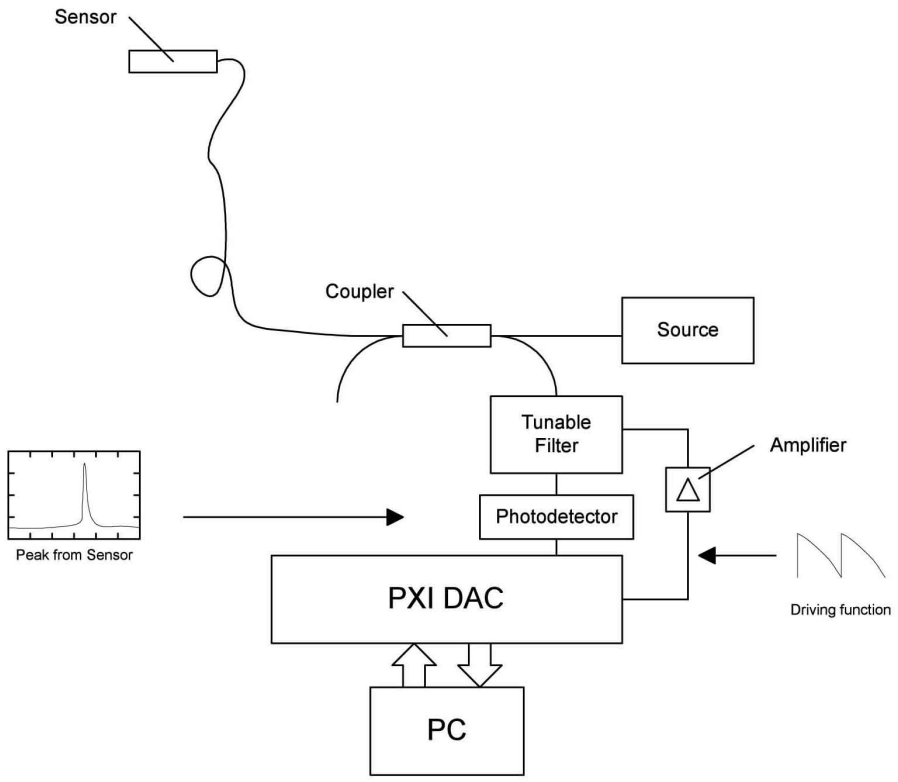


**Figure 9-1: Custom-built sensor interrogation system**

The optical source used in this research was an Optosci EDFA Broadband source. This source operates by using a 980 nm pump laser to stimulate photon emission in a length of fibre doped with erbium. This results in a broad source spectrum as shown in Figure 9-2. The advantage of this type of source is, that it provides a large bandwidth (typically 35 nm) and a high-power output (up to 30 mW). A disadvantage of this type of source is the large variation in power levels across the spectrum.

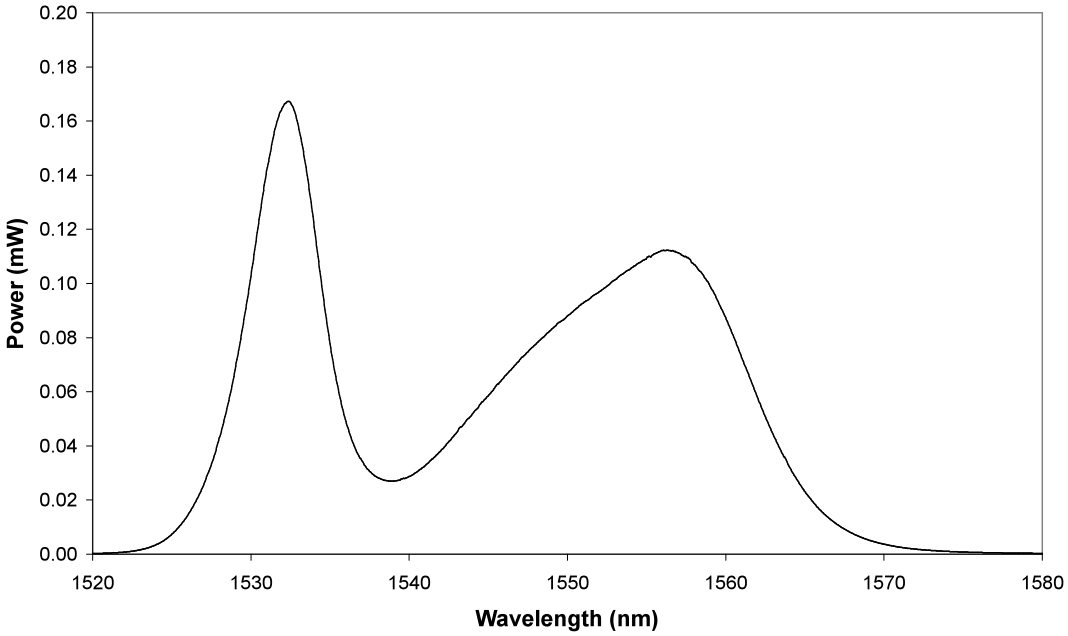


**Figure 9-2: EDFA source spectrum**

Spectral signals reflected from the FBG were analysed using a high speed scanning Fabry–Perot tunable filter (FP-TF, Nortel Networks) driven by an analogue saw-tooth voltage signal from a PXI digital-to-analogue converter (National Instruments) to change the length of the cavity to enable it to sweep across the spectral signal. The tuning voltage per FP-TF free spectral range was 40 V. A voltage amplifier was used to adjust the DAC output level so that it was compatible with that of the filter drive voltage requirement. The spectral signal reflected from the sensor was recorded using a detector and a PXI data acquisition card, and subsequently processed in a computer to recover the instantaneous position of the FBG peak. The FP-TF was thermally

stabilized using a thermoelectric cooler (TEC) controller. All optical components were interconnected using single-mode fibre, spliced or terminated with FC/APC connectors. This system has a maximum scanning frequency of 4 kHz and a wavelength range of 1525-1574 nm. The additional temperature reference was provided by a thermocouple.

The specially designed interrogation system used in these experiments was designed and built by Grzegorz Fusiek as part of his PhD studies. For more detail information on this system, the reader is referred to [1-3].

Since this interrogation system was used to conduct the experiments discussed in the next chapter, there have been a number of developments in Bragg grating sensor interrogations systems and progress continues to take place in this area. Systems with scanning filters of up to 10 kHz have been reported in the literature [4]. Using these new and improved systems would further improve the output obtained from the sensor.

## 9.3 Coil Design

A coil was designed for experimental testing of the sensor for ac currents up to 1 A (zero-to-peak), 2 A (peak-to-peak) and temperatures of up to 70°C.

The coil consists of 1280 turns of 19 SWG, 1 mm enamelled copper wire. The copper wire has a resistance of 22.63 ohms per kilometre and was turned round a specially designed plastic bobbin. The bobbin was designed to hold the sensor's holder/ prestress housing and withstand the high temperatures that would be produced during the experimental process. The bobbin was constructed from a tube of Caw black PVC with outer diameter of 2.5 mm. The black caw PVC has a melting point of 160-165˚C, and was chosen due to material availability. The bobbin design was completed with outer holders made from Nylon 66, which has a melting point of 255˚C.

The caw PVC tube was cut to 110 mm and the outer holders were placed 80 mm apart at a distance of 10 mm from the end of the caw tube. The coil was made of 6 layers each with 80 turns. The total wire length is 135.21 m and therefore, the coil has a total resistance of 3.06Ω and inductance of 21.97 mH. The coil calculations can be seen in Appendix C.

The measurement range of the sensor can be varied by altering the design of the sensor coil.

## 9.4 Chapter References


[1] Fusiek, G., "Wavelength Discrimination Devices and Spectrally Encoded Sensors for Dynamic Monitoring of Electrical Plant," PhD Thesis, University of Strathclyde, Department of Electronic and Electrical Engineering, 2008.

[2] Fusiek, G., Niewczas, P., McDonald, J. R., "Extended Step-out Length Fiber Bragg Grating Interrogation System for Condition Monitoring of Electrical Submersible Pumps", Optical Engineering, Vol. 44, Issue 3, 2005

[3] Fusiek, G., Niewczas, P., McDonald, J. R., "Performance Analysis of the Fibre Bragg Grating Interrogation System Based on an Arrayed Waveguide Grating," IEEE Instrumentation and Measurement Technology Conference, Colorado, USA, May 2003.

[4] Todd, M.D., Seaver, M., Bucholtz, F., "Improved, operationally-passive interferometric demodulation method using 3 x 3 coupler," Electronic Letters, Vol. 38, No.15, July 2002, pp.784-786.

# 10 Experimental Results

The following section details a number of experiments that were conducted during the characterisation and testing of the sensor. This includes the characterisation of the nonlinearities and hysteresis inherent in the magnetostrictive material, determination of how these characteristics are affected by the application of a magnetic bias and observing the effect of current and temperature on the sensor. Work carried out in compiling the proposed signal processing method is also discussed.

## 10.1 Sensor Characterisation

Initial experiments were conducted using a dc current source and a specially designed coil, as discussed in Chapter 9, in order to characterise the sensor. Although the sensor was designed to demonstrate measurement of zero to one Amperes ac (zero-to-peak), it was necessary first to characterise the sensor over a greater current range. The chosen current range was 0 to 8 A dc. These initial experiments were first conducted on the material in its natural state: without a magnetic bias.

The current applied to the coil was increased from 0 to 8 A and then decreased back to 0 A. The corresponding wavelength shift was plotted in Figure 10-1 below.

Although Figure 10-1 shows input current plotted against wavelength, it effectively shows the positive section of the sensor's "butterfly" curve as described in Section 6.2. The current applied to the coil determines the magnetic field induced in the sensor, while the wavelength shift exhibited is a measure of the sensor's response to the magnetostriction (strain) experienced by the magnetostrictive material in the sensor.

This graph shows the sensor's nonlinear response in its natural state. Between 0 and 3 A the sensor's response is nonlinear and there appears to be significant hysteresis. The sensor is much more sensitive over this range than at higher currents. At 3 A there is a severe fluctuation caused by the power supply. Above 3 A, the sensor response becomes more linear and the width of the hysteresis loop decreases

significantly. However, the wavelength shift is much smaller for a given increase in current, demonstrating that the sensor has lower sensitivity in this region. This is because at higher currents the magnetostrictive material is approaching its saturation point.

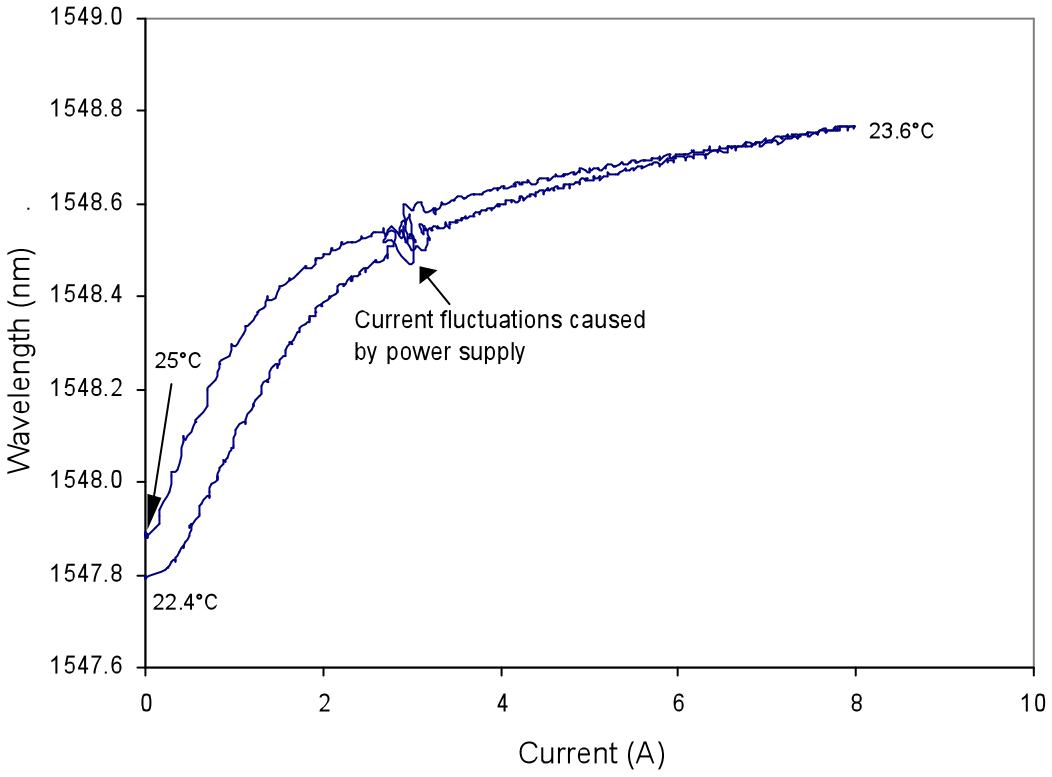


**Figure 10-1: Sensor response in its natural (unbiased) state**

It should be noted that the severe fluctuation evident at 3 A was caused by a fault in the power supply that was used during the experimental process. The slight fluctuations in the sensor output resulted from the current being increased manually during the experiment which was the only way of operating the available power source. The manner in which the current was increased and decreased made it difficult to achieve the desired output in a smooth fashion. These fluctuations can be seen in the power supply output as illustrated in Figure 10-2.

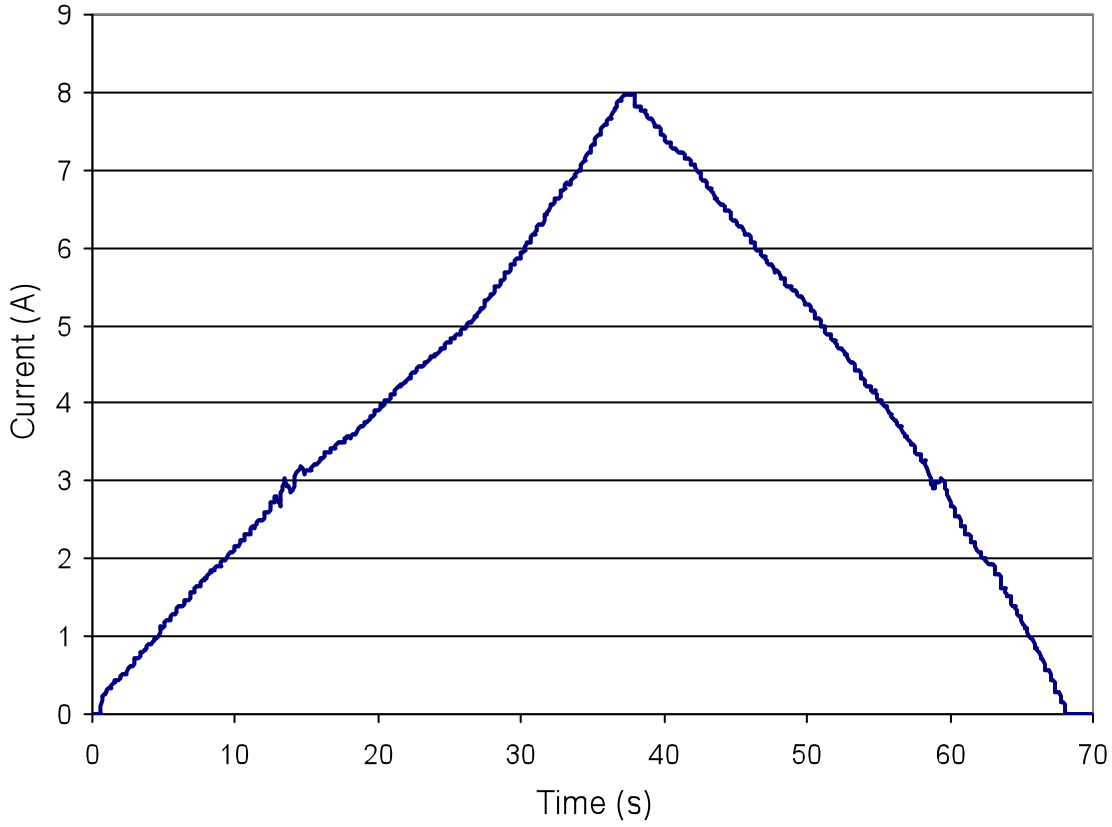


**Figure 10-2: Output from the power supply**

When characterising the sensor, it is important to consider the effects of the operating conditions on its output response. The sensor will not only be operating in an environment of changing magnetic field but also of varying temperature. Therefore it is important to gain an understanding of how the sensor's output response is affected by changes in temperature. This was achieved by conducting the sensor characterisation experiment, as described above, at a range of different temperatures.

Holding the temperature constant during the experimental process proved to be difficult since the test run, while short, generated a large amount of heat in the coil. During the experiment from which the graph (shown in Figure 10-1) was produced, the temperature was monitored using a thermocouple. At the start of the experiment

the temperature at the sensor head was 22.4°C. The temperature had increased to 25°C by the time the current was reduced back to zero. The width of the hysteresis loop at the 0A point in Figure 10-1 is equal to approximately 0.1 nm. There is no doubt that this is partially due to the inherent hysteresis of the magnetostrictive material. However, it is worth quantifying the portion caused by temperature variation experienced during the cycle.

Temperature will have an effect on the system in terms of thermal expansion of the magnetostrictive material, thermal expansion of the silica fibre and change in refractive index of the Bragg gratings as discussed in Section 7.2. Therefore, the following calculations were performed in order to quantify the effect of temperature change on the results obtained during the experiment previously discussed.

*Contribution due to the thermal expansion of the magnetostrictive material:*

Temperature change, $\Delta T = 2.6$ °C

Coefficient of thermal expansion of the material, $\alpha = 10\sim12$ ppm / °C

Constant of proportionality between strain and wavelength shift in an FBG,

$Cp = 1.15 \text{ pm} \cdot \mu\varepsilon^{-1}$

*Strain experienced in the material for a temperature change ΔT:*

$$\varepsilon = \alpha \cdot \Delta T$$

$\varepsilon = 26\sim31.2$ ppm or με

*Wavelength shift experienced due to temperature induced strain*:

$$\Delta\lambda_B = \varepsilon \cdot Cp$$

$\Delta\lambda_B = 29.9\sim35.9$ pm $= 0.0299\sim0.0359$ nm

*Contribution due to change in refractive index of FBG due to temperature:*

Bragg wavelength, $\lambda_B = 1547$ nm

$$\Delta\lambda_B = 6.67 \cdot 10^{-6} \cdot \lambda_B \cdot \Delta T$$

$$\Delta\lambda_B = 0.0268 \text{ nm}$$

***Total contribution due to temperature change:***

$\Delta\lambda_B = 0.0359 + 0.0268$

$\Delta\lambda_B = \underline{0.0627 \text{ nm}}$

The temperature change was measured to be 2.6 ºC, calculated to be equivalent to a wavelength shift of 0.0627 nm. Figure 10-1 shows the width of the hysteresis loop at the zero ampere point to be 0.1 nm. Thus the above calculations suggest that approximately 63% of this width is caused by the effects of temperature and therefore approximately of 27% is due to hysteresis. This demonstrates that in these operating conditions the effect of temperature change is more significant than that of hysteresis.

This simple calculation shows that even small changes in temperature have an effect on the accuracy of the sensor and highlights the importance of decoupling temperature from the sensor's output signal. The sensor design described in this thesis is capable of simultaneously measuring ac current and temperature at the sensor head and thus enables temperature compensation to be applied. This will be discussed in a later section.

Figure 10-3 shows the sensor response with increasing temperature over the same current range as that shown in Figure 10-1. When the experiment started the temperature was 22.4˚C and the heating effect of the coil was used as the method of raising the temperature for experimental purposes. The current was cycled between 0 and 8 A four times and the temperature had reached 43.6˚C on completion. Due to the

method used to raise the experimental temperature it was not possible to achieve steady temperature increments.

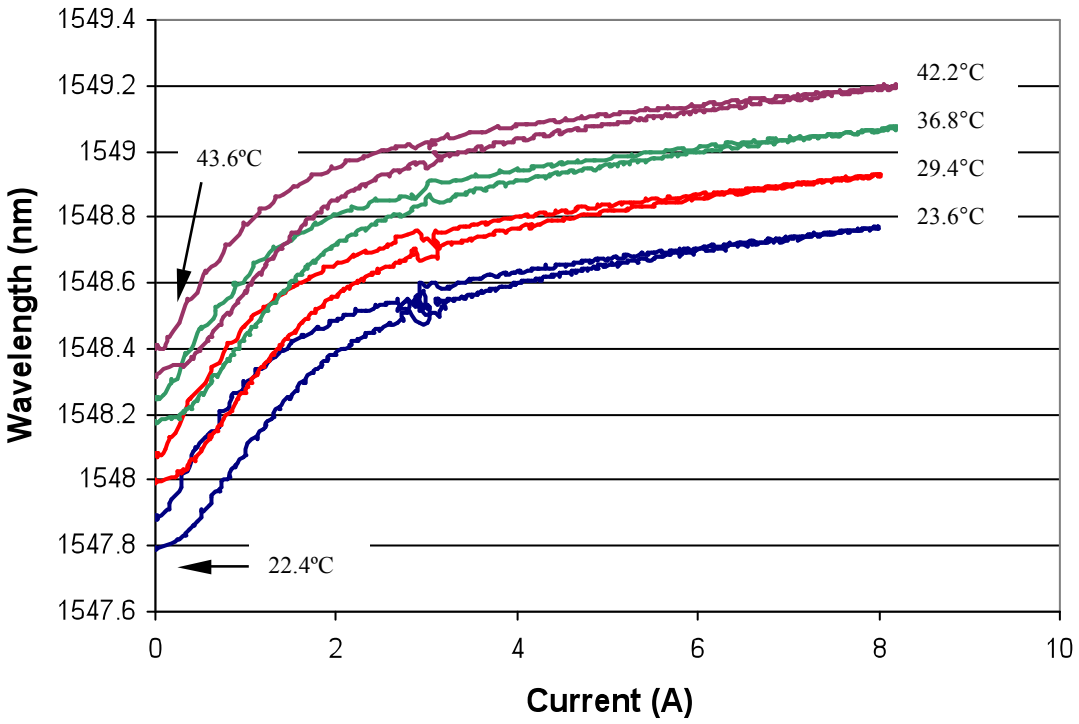


**Figure 10-3: Change in material characteristic for increasing temperature**

Visually, it seems that there is no significant change to the overall sensor output characteristic. However, it can be seen that, as the temperature increases, the characteristic shifts in the wavelength axis. In fact, the temperature also has an effect on each individual cycle, slightly broadening the "loop" of each cycle.

Following the initial dc experiments, the polarity of the applied dc current was reversed. The experiments performed under these conditions also resulted in a positive expansion of the magnetostrictive material under increasing current and the sensor output was very similar to that achieved in the previous set-up.

## 10.2 Application of Magnetic Bias

A magnetic bias was applied to the magnetostrictive material to enable a relative negative strain to be produced in the material sample for the negative part of an ac signal instead of positive elongation for both the positive and negative parts of a cycle. Thus allowing a sinusoidal measured signal to be produced from the optical current sensor, as discussed in section 6.3 and depicted in Figure 6-5.

The optimum magnetic bias was chosen to be 40 kA/m to facilitate a more linear sensor operation. Figure 10-4 shows the sensor output over the range 0 to 8 A dc following the application of the magnetic bias. The resulting response is more linear and appears to suffer less from hysteresis. This graph shows the likely response of the sensor during the positive parts of the ac current cycle.

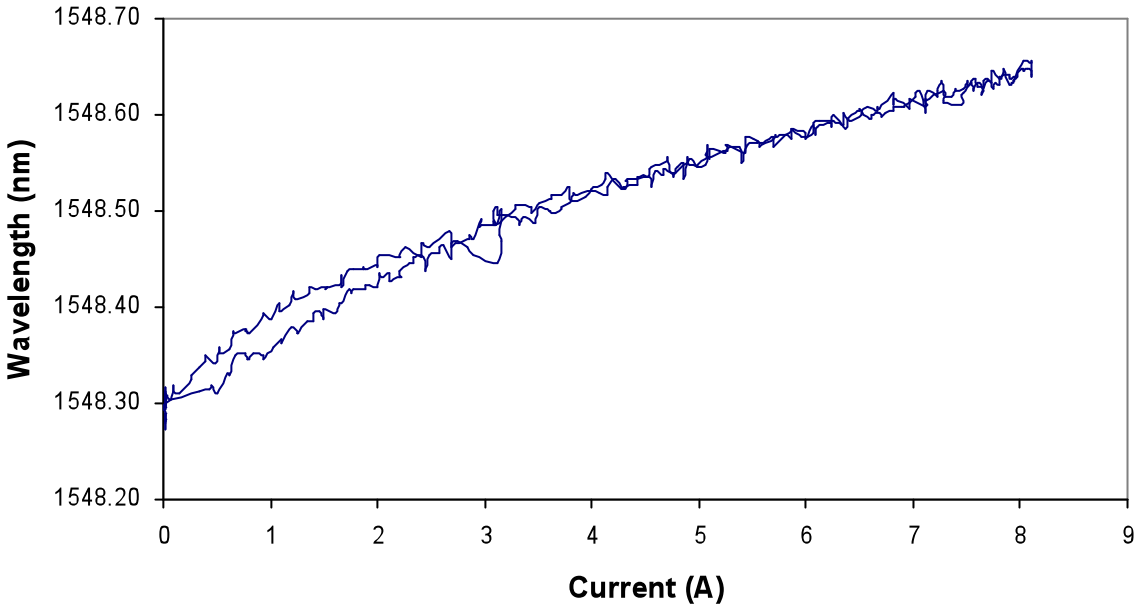


**Figure 10-4: Bias material output**

The polarity of the coil leads were then switched. Again the sensor was exposed to the magnetic field resulting from dc current in the range 0 to 8 A. The sensor output is shown in Figure 10-5.

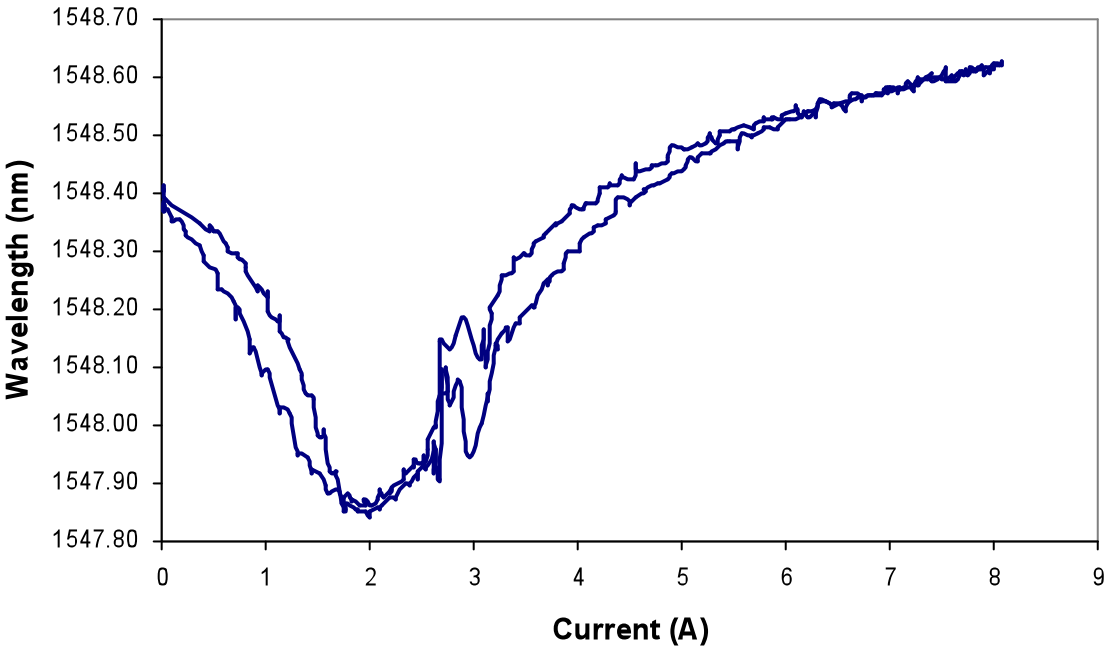


**Figure 10-5: Biased material output (reversed polarity)**

Both Figure 10-4 and 10-5 together show the butterfly hysteresis loop for the sensor: if the mirror image of Figure 10-5 along the y-axis was lined up with the y-axis of Figure 10-4. However, it should be noted that due to the use of a coil in the experimental set-up, it was difficult to conduct the experiments for both polarities at the same temperature. That is why the graphs do not line up precisely along the y-axis. The experimental conditions during the experiments illustrated in Figure 10-4 and 10-5 are shown in Table 3.

| | **Figure 10-4** | **Figure 10-5** |
|---|---|---|
| **Start Temperature (˚C)** | 24.1 | 28.8 |
| **End Temperature (˚C)** | 24.6 | 31.2 |
| **Duration (s)** | 46.26 | 51.54 |

**Table 3: Magnetic bias experimental conditions**

Therefore, due to the 4.2˚C temperature rise, while the polarity was being changed over, the wavelength at 0 A in Figure 10-5 is approximately 0.1 nm higher than at the end of the experiment illustrated in Figure 10-4. This shift in wavelength can be theoretically proven to be the result of the temperature change in the following calculations:

*Contribution due to the thermal expansion of the magnetostrictive material:*

Temperature change, $\Delta T = 4.2$ °C

Coefficient of thermal expansion of the material, $\alpha = 10\sim12$ ppm / °C

Constant of proportionality between strain and wavelength shift in an FBG,

$Cp = 1.15 \text{ pm} \cdot \mu\varepsilon^{-1}$

*Strain experienced in the material for a temperature change ΔT:*

$$\varepsilon = \alpha \cdot \Delta T$$

$\varepsilon = 42\sim50.4$ ppm or με

*Wavelength shift experienced due to temperature induced strain*:

$$\Delta\lambda_B = \varepsilon \cdot Cp$$

$\Delta\lambda_B = 48.3\sim57.96$ pm $= 0.04830\sim0.05796$ nm

*Contribution due to change in refractive index of FBG due to temperature:*

Bragg wavelength, $\lambda_B = 1547$ nm

$$\Delta\lambda_B = 6.67 \cdot 10^{-6} \cdot \lambda_B \cdot \Delta T$$

$$\Delta\lambda_B = 0.04333 \text{ nm}$$

***Total contribution due to temperature change:***

$\Delta\lambda_B = 0.04830 \sim 0.05796 + 0.04333$

$\Delta\lambda_B = \underline{0.092 \sim 0.101 \text{ nm}}$

Since the prototype sensor was designed to measure ac currents up to 1 A (zero-to-peak) during the positive cycle of the ac current, the sensor response will follow the response illustrated in Figure 10-4 from 0 to 1 A. During the negative cycle of the ac current, the sensor will follow the response showing in Figure 10-5 from 0 to 1 A. Thus the application of the bias will enable the sensor to experience both positive (elongation) and negative (contraction) magnetostriction in response to an ac current as discussed in section 6.3.

These experiments also show that while operating within the designed operating range during the positive part of the cycle, the sensor will not reach saturation which takes place beyond 8 A dc and thus 8 A ac (zero-to-peak). For the negative part of the cycle, the sensor will not reach the point at which the relative negative magnetostriction would switch to positive magnetostriction (the former quiescent point). This point is located at approximately 2 A dc and thus 2 A ac (zero-to-peak), as illustrated in Figure 10-5, well beyond the sensor's designed operating range.

Following the application of the magnetic bias, further experiments were conducted to determine the sensor's response to ac currents.

## 10.3 AC Experiments

This section looks at the output of the sensor when a 50 Hz ac current is applied to the coil following the application of the magnetic bias.

### 10.3.1 Current Measurement

During the course of the ac experiments, known currents were applied to the coil covering the measurement range 0.1 to 1.0 A (zero-to-peak), 0.2 to 2 A (peak-to-peak), 0.07 to 0.71 A (rms) and the optical output signal was obtained from the

custom-built interrogation system. Both the input current signal and the optical output signal for the currents in the range were recorded in steps of 0.1 A (zero-to-peak), 0.2 A (peak-to-peak) and 0.07 A (rms). The input current signal was derived from the output voltage from an ac power supply as described in section 9.2. Throughout the remainder of this thesis alternating currents will be referred to in terms of their amplitude or zero-to-peak values.

Figure 10-6 shows the output of the sensor when a current of 0.3 A (zero-to-peak) is applied to the coil. As can be seen, the current sensor is capable of measuring both the positive and negative parts of the current due to the application of the magnetic bias.

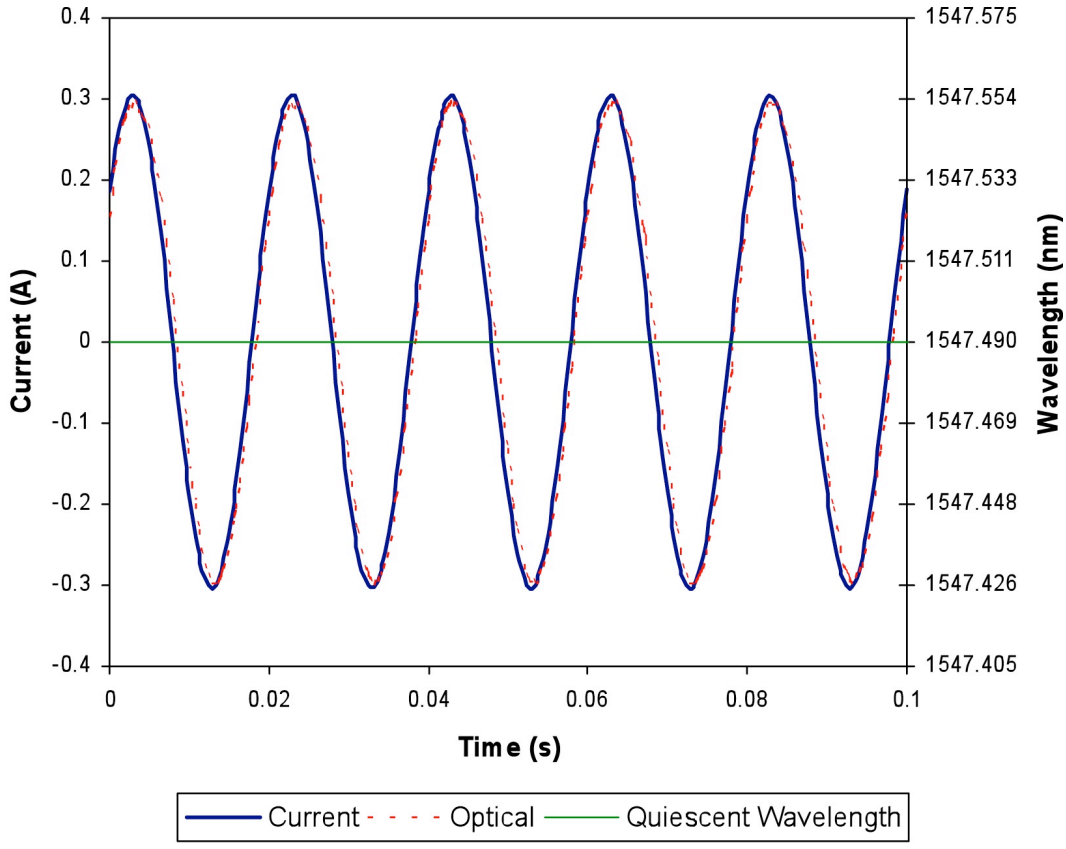


**Figure 10-6: Sensor optical output and 0.3 A reference current at 18.5˚C**

At 0.3 A (zero-to-peak), the optical output signal from the sensor appears to be a fairly well formed sine wave. At this current level the sensor's sensitivity is the same

for the positive and negative part of the ac current. This is because the sensor is still operating fairly close to the quiescent point which is located at approximately 1547.490 nm.

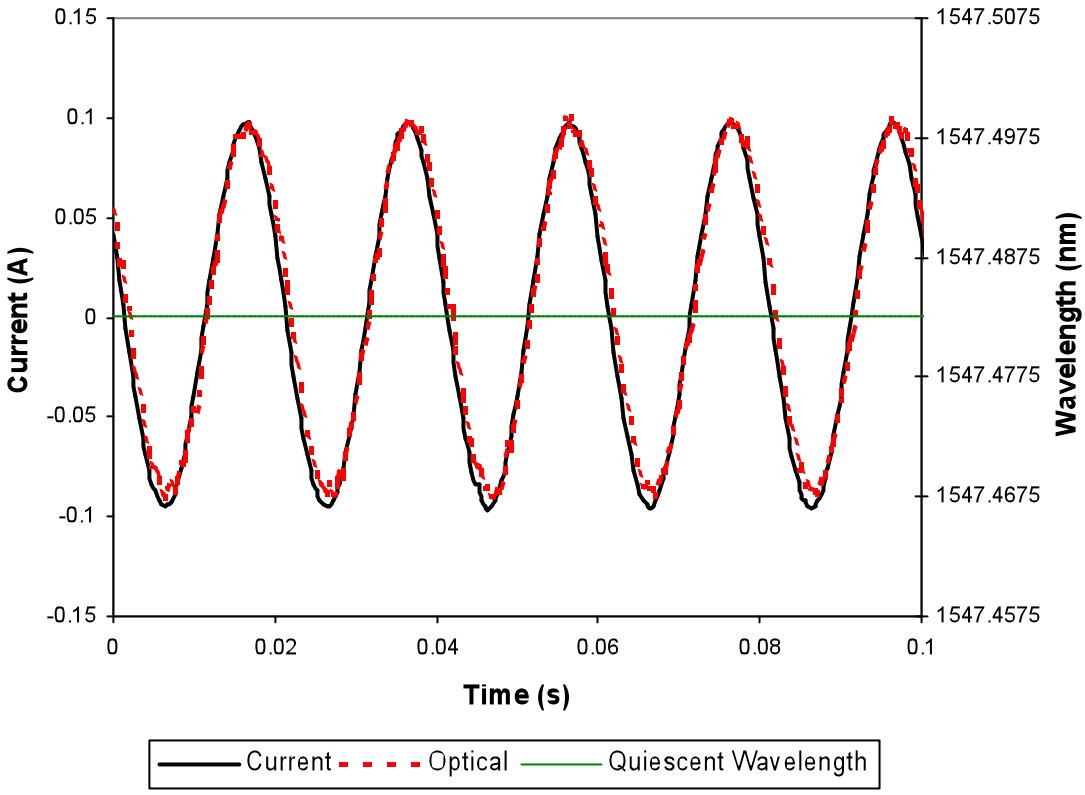


**Figure 10-7: Sensor optical output and 0.1 A reference current at 18.5°C**

Figure 10-7 shows the sensor's response to a smaller current of 0.1 A (zero-to-peak) being applied to the coil. The quiescent point is located at approximately 1547.483 nm. It is evident that although the output signal is also a fairly well formed sine wave, there is a lot of noise in the optical signal at this lower current level. Similar noise was also seen in the output signals for 0.05 A and 0.2 A (zero-to-peak).

Figure 10-8 and Figure 10-9 show the sensor's response to the application of higher ac currents to the coil, 0.6 A (zero-to-peak) and 1.0 A (zero-to-peak) respectively. It is apparent that at these higher currents the optical signal, unlike the

reference signal is not symmetrical. For larger currents the sensor is less sensitive to the positive part of the current than the negative part and thus the amplitude of the negative half cycle of the signal is greater than that of the positive.

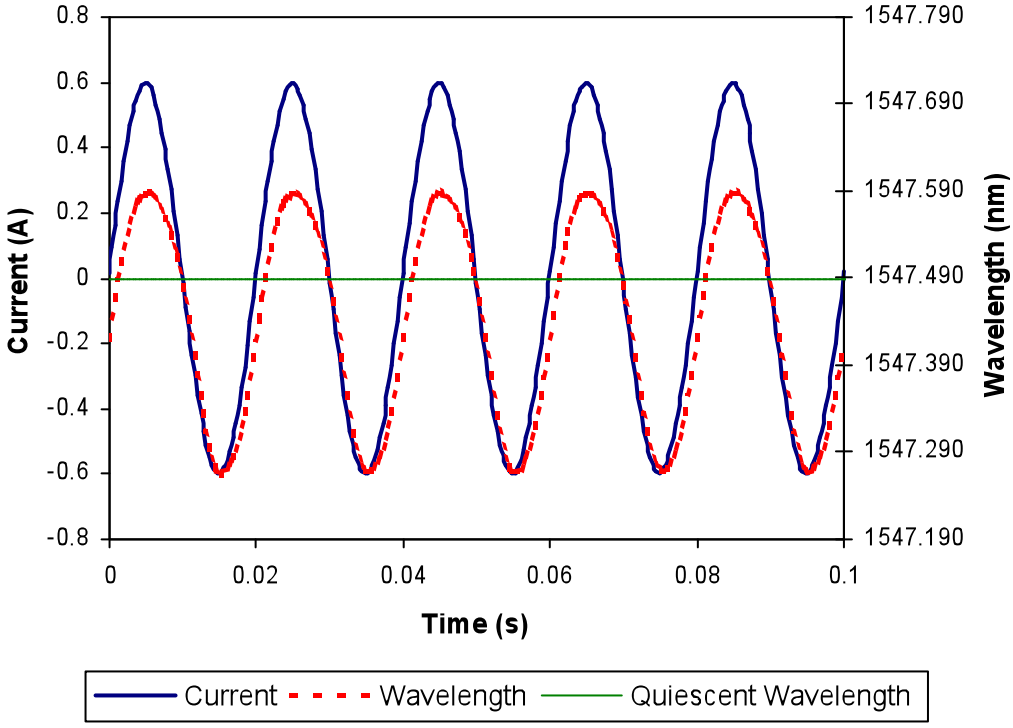


**Figure 10-8: Sensor optical output and 0.6 A reference current at 18.5°C**

At 0.6 A (zero-to-peak), the wavelength difference between the quiescent point, located at 1547.490 nm, and the positive peak is 0.0969 nm, while there is a 0.0223 nm wavelength difference between the quiescent point and the negative peak. At this current level the sensor is 130% more sensitive to the negative part of the current cycle compared to the positive part.

As the current increases, this sensitivity difference increases even further. At 1.0 A (zero-to-peak), the sensitivity to the negative part of the cycle is 160% higher than for the positive part. The quiescent point is located at approximately 1547.490 nm, while the positive peaks and negative peaks are located at 1547.696 nm and 1546.959 nm respectively.

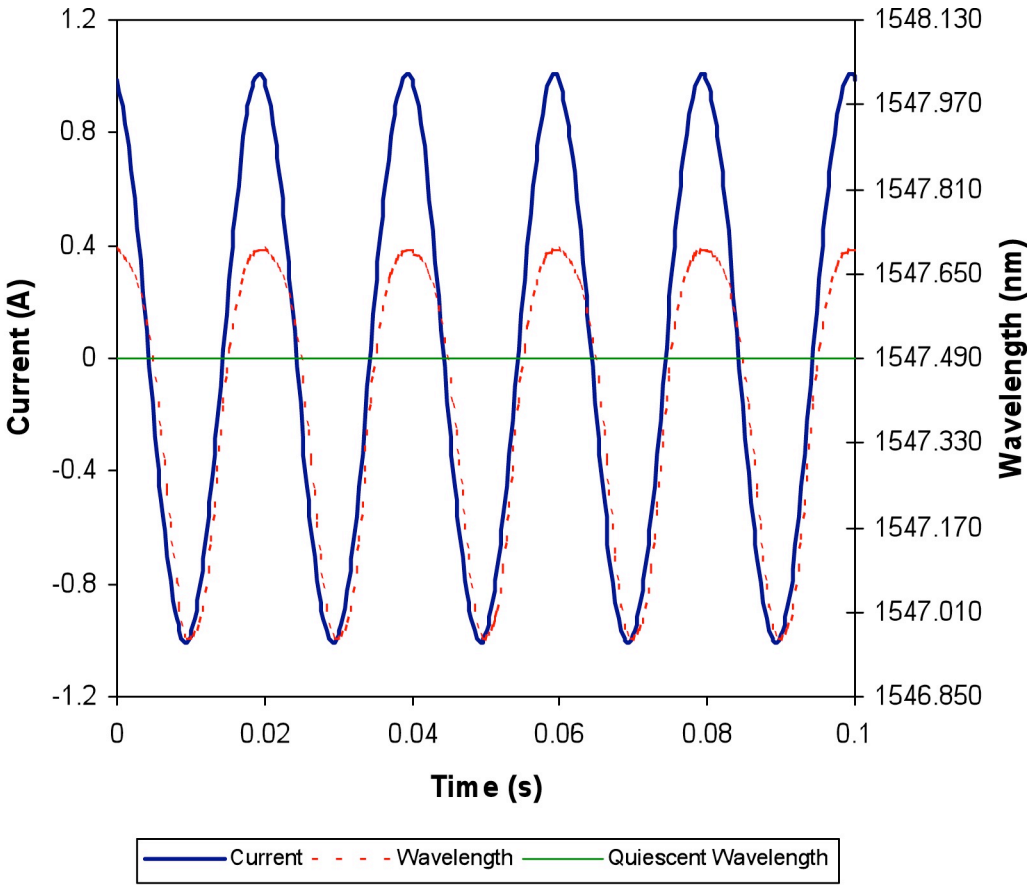


**Figure 10-9: Sensor optical output and reference current 1.0 A at 18.5°C**

Again, it is apparent from Figure 10-8 and Figure 10-9 that the optical signal, unlike the reference signal, is not symmetrical. For larger currents the sensor is less sensitive to the positive part of the current than the negative and thus the amplitude of the negative half cycle of the signal is greater than that of the positive. This is further illustrated in Figure 10-10, where the output signal for 0.3, 0.6 and 1.0 A is plotted on the same graph, this time without the input signal.

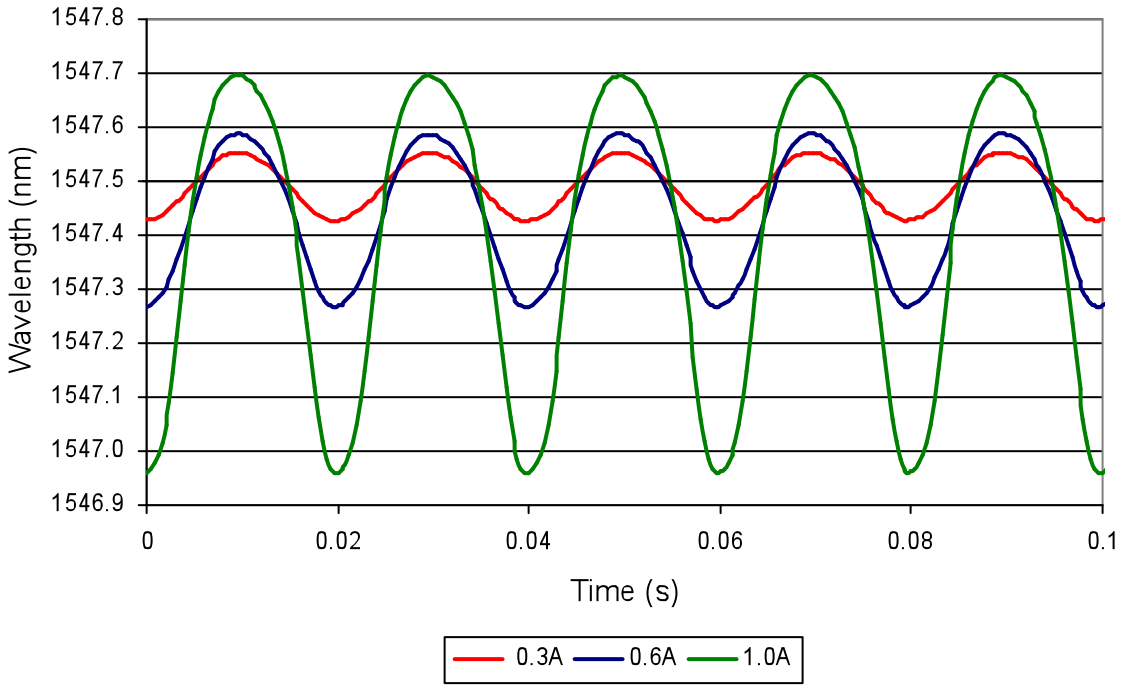


**Figure 10-10: Sensor optical output for 0.3, 0.6 and 1.0 A at 18.5˚C**

As described earlier, this is due to the nonlinearity of the material response. The introduction of the magnetic bias to the sensor also adds to this affect. As described in Section 6.3, the bias moves the sensor's quiescent point to a region in which the material characteristics are different at either side of the quiescent point. At higher currents this is also because for the positive part of the cycle, the magnetostrictive material is tending towards its saturation point. The quiescent point for all of these experiments is approximately 1547.490 nm; this is because all of the experiments were conducted at approximately 18.5˚C.

It can be seen from Figure 10-6 to Figure 10-10 that as the peak value of current increases, the sensor transfer characteristics depart significantly from the ones recorded for lower currents. However, there is a direct correlation between peak-to-peak amplitude and the applied current. This relationship is illustrated in Figure 10-11 at 18.5˚C.

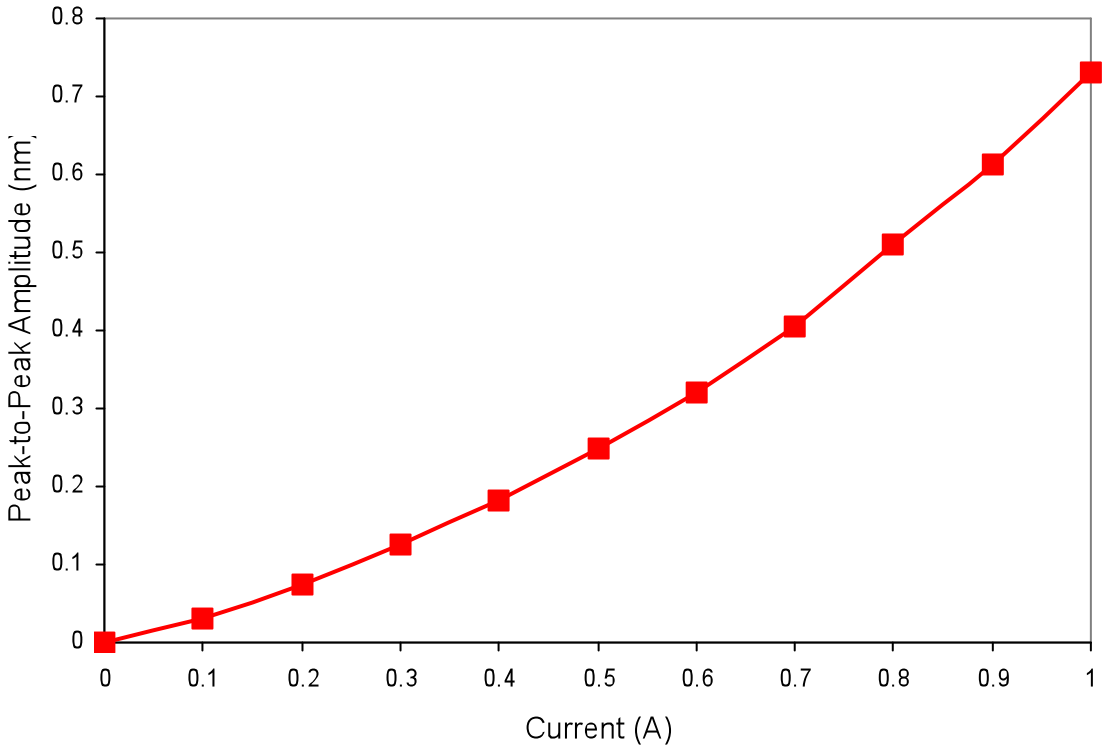


**Figure 10-11: Relationship between peak-to-peak wavelength and current at 18.5˚C**

The relationship between peak-to-peak wavelength and current as illustrated in Figure 10-11 is nonlinear. As the ac current levels increase, the corresponding increase in peak-to-peak current gets bigger. This is due not only to the nonlinear material characteristic, but also the application of the magnetic bias. At higher current levels, even though sensitivity of the sensor to the positive part of the current is decreasing, the sensor's sensitivity to the negative part of the current cycle is increasing. These effects combined result in a greater peak-to-peak amplitude for a given increase in current.

So far within this section we looked at the sensor's ability to measure a range of currents at constant temperature. During the experiments every effort was made to keep the temperature as constant as possible at approximately 18.5˚C. However,

during normal operation, the sensor will be situated in an environment where the temperature will vary. Therefore it is necessary to determine how this relationship will be affected by changes in temperature.

The above experiments were conducted over a range of temperatures and recorded at 18.5, 34.8, 46.0, 56.9 and 69.1˚C. The relationship between peak-to-peak wavelength and applied current at 18.5, 46.0 and 69.1˚C can be seen in Figure 10-12.

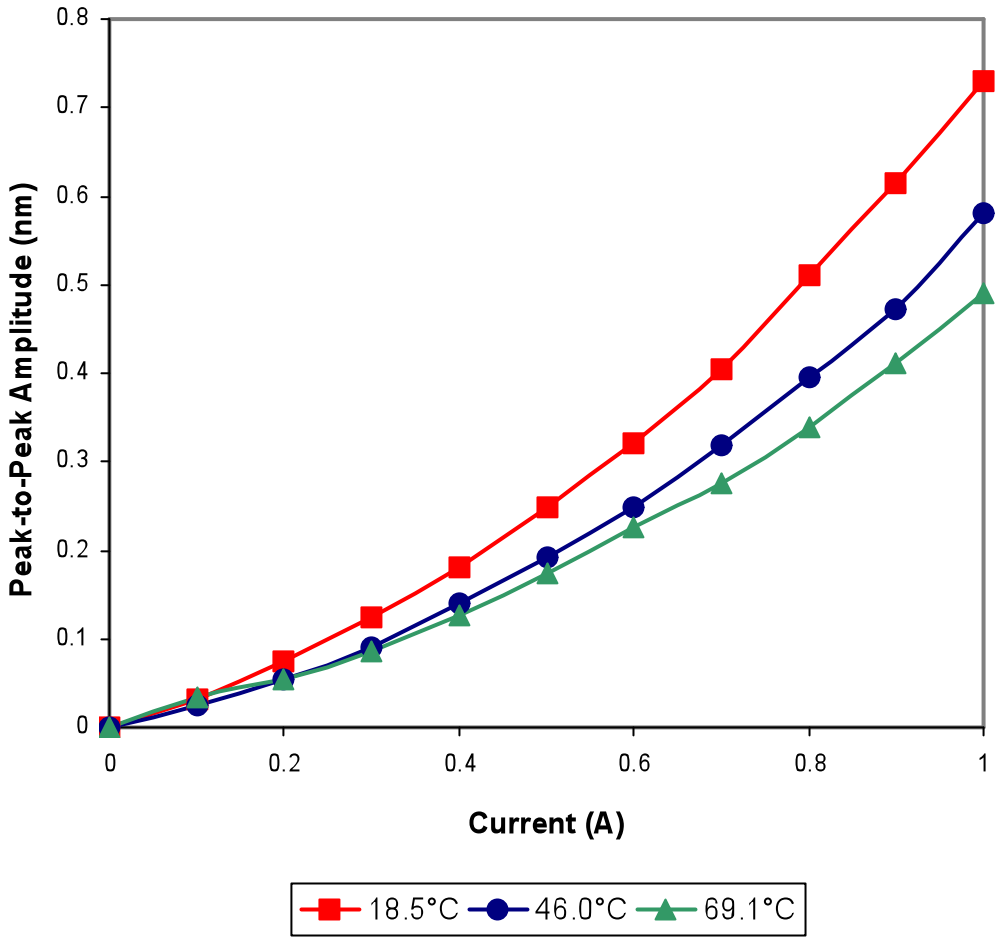


**Figure 10-12: Relationship between peak-to-peak wavelength and applied current at various temperatures**

It can clearly be seen that as the temperature increases, the peak-to-peak wavelength for a given current decreases. This is due to the inherent thermal

behaviour of the magnetostrictive material. Thermal expansion of the magnetostrictive material causes the quiescent point to shift up the material characteristic curve in the same matter as the magnetic bias. As the quiescent point shifts upwards, the sensor's operating characteristic moves into a less sensitive region of operation. This relationship is further illustrated in Figure 10-13.

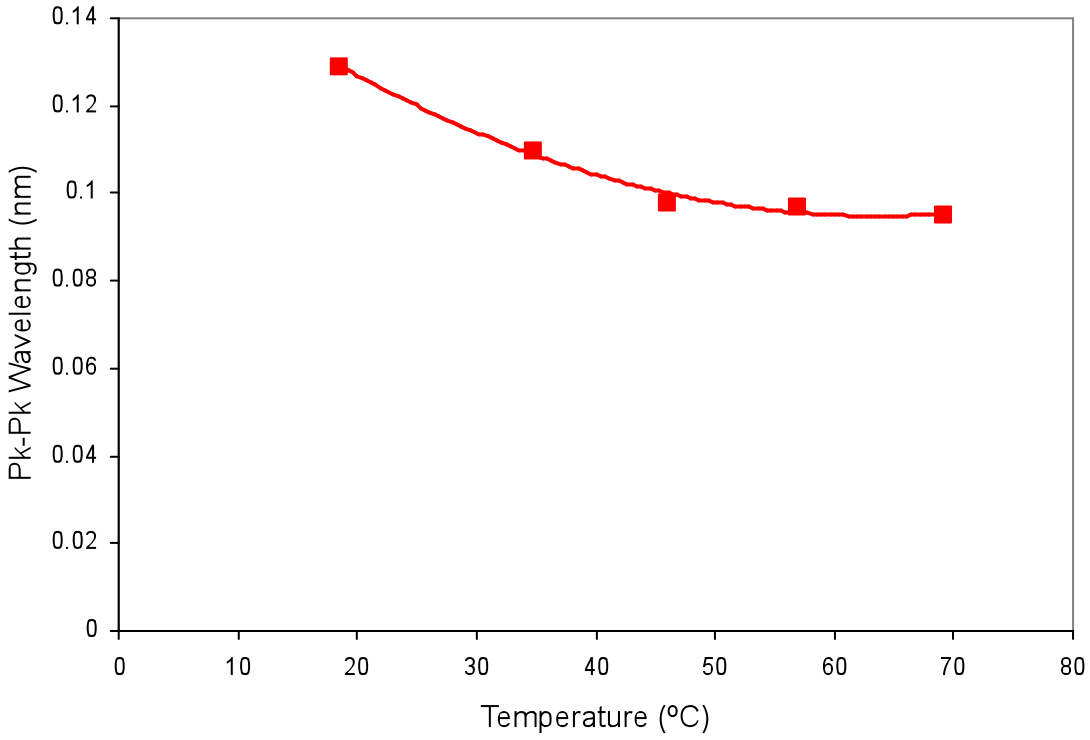


**Figure 10-13: Temperature dependence of instantaneous signal amplitude at 0.3 A**

In this section it has been shown that there is a relationship between peak-to-peak wavelength of the sensor output and the known current input. However, it has also been shown that this relationship is temperature dependent. Thus if peak-to-peak detection in the interrogation system is to be used to determine the magnetic field, and thus current at the sensor head, then the temperature at the sensor head must also be known.

Since the sensor is a combined optical current and temperature sensor, it is capable of recording both magnetic field and temperature at the sensor head. Thus this thermal dependence can be readily corrected using a correlation routine or look-up table. The following section describes how the sensor can be used to measure temperature at the sensor head.

### 10.3.2 Temperature Measurement and Sensor Hysteresis

Temperature information can also be recovered from the sensor's optical output by identifying the wavelength of the quiescent point. In the previous section, the quiescent point in Figure 10-6 to Figure 10-10 remained at approximately 1547.49 nm. This is because the temperature was held fairly constant, at 18.5˚C, during the experiments.

The quiescent point can also be seen from a hysteresis loop.

Figure 10-14 shows the hysteresis loop for current measurement of 0.3 A plotted over 10 cycles. The quiescent of the sensor at 18.5˚C can be seen to be 1547.49 nm. This is in agreement with Figure 10-6 to Figure 10-10.

As temperature increases, the wavelength of this point will also increase. Figure 10-16 illustrates this, by plotting the sensor response to an applied current of 0.3 A (zero-to-peak) at different temperatures.

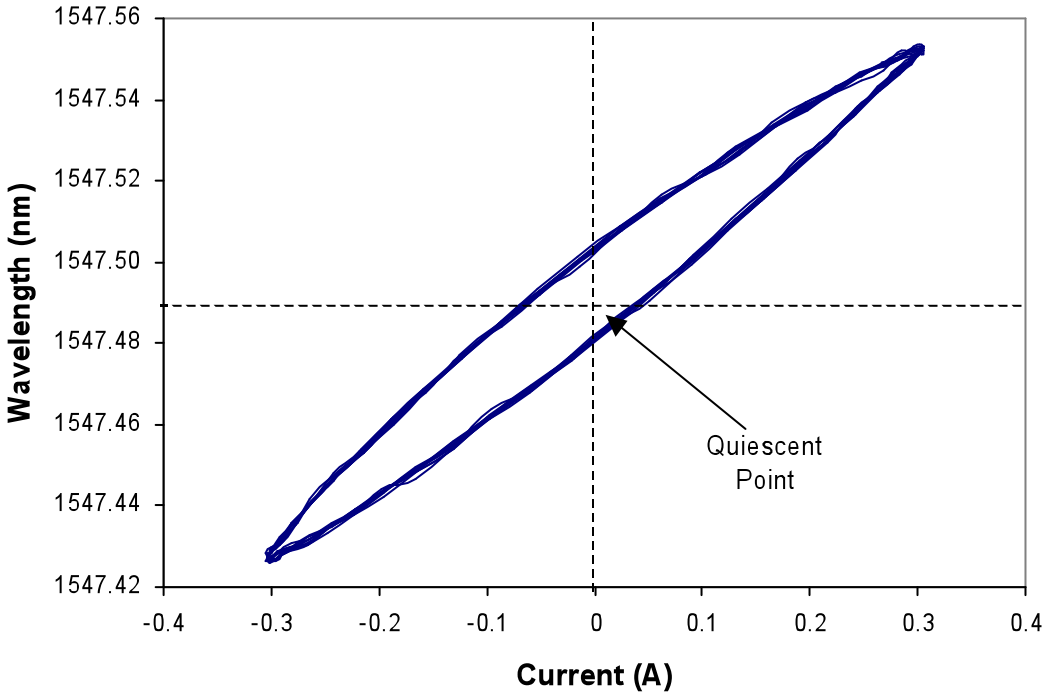


**Figure 10-14: Hysteresis loop for current measurement of 0.3 A at 18.5˚C**

In this research it is proposed that the quiescent point, and thus the temperature at the sensor head, can be determined by calculating the average wavelength in a single period. This process has been built into the custom-built interrogation system.

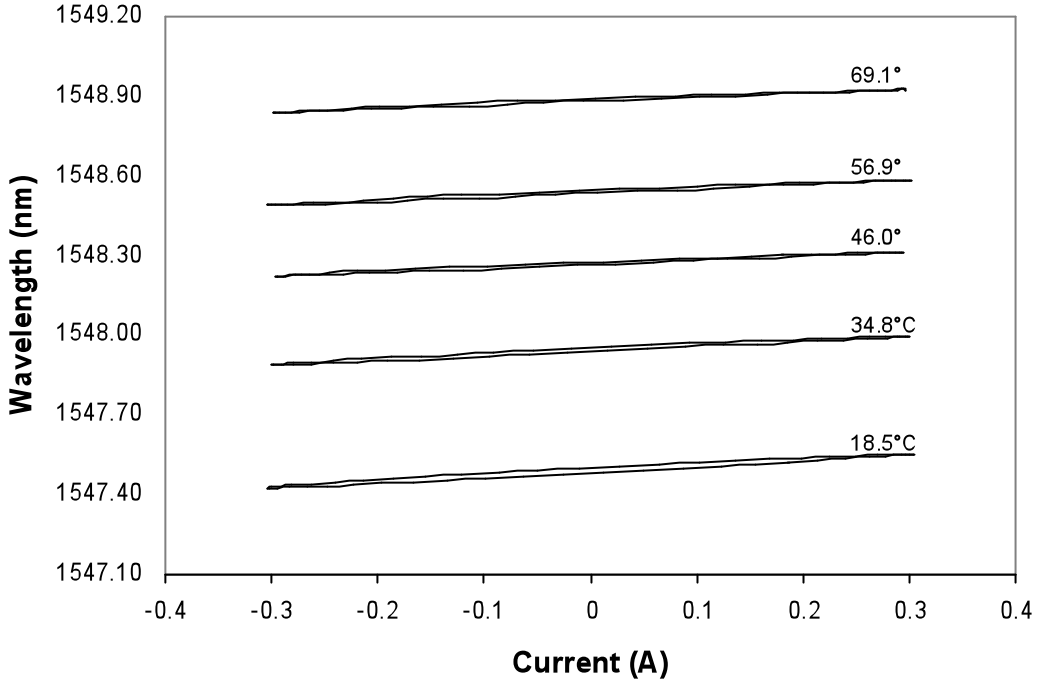


**Figure 10-16: 0.3 A Current measurement at various temperatures**

The relationship between temperature and average wavelength at 0.3 A is plotted in Figure 10-17, and can be seen to be linear, with $\Delta\lambda/\Delta T$ equal to 2.64 nm/100˚C.

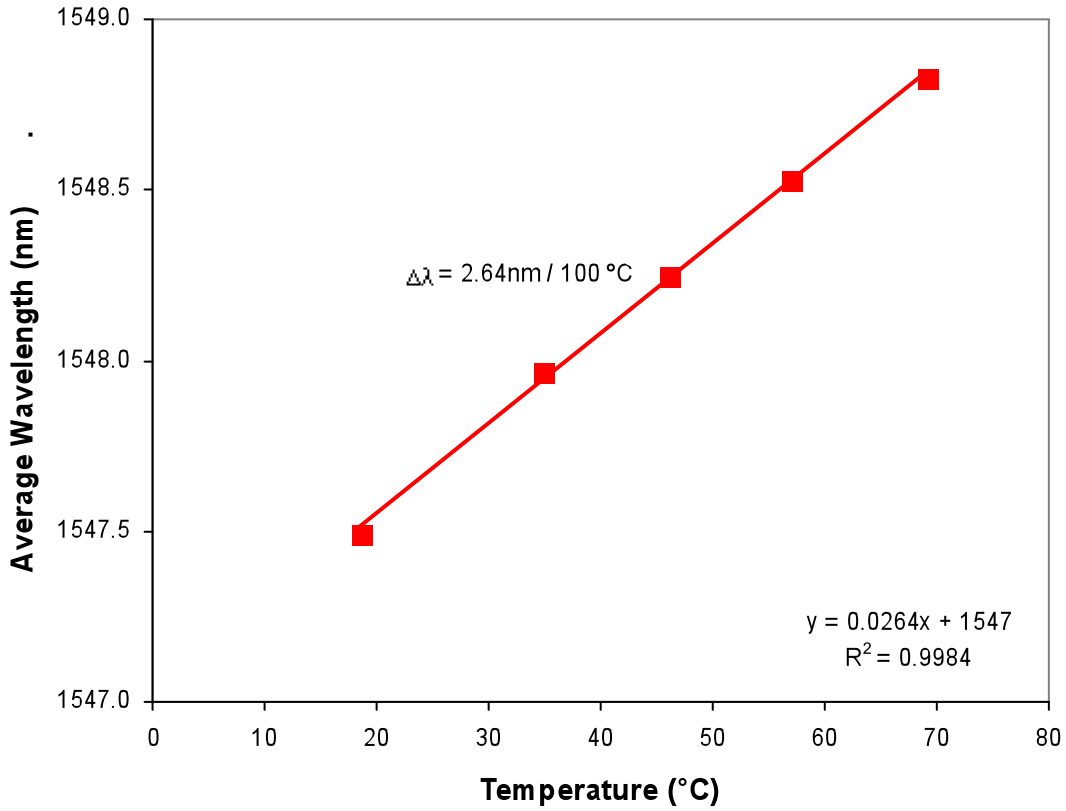


**Figure 10-17: Relationship between temperature and wavelength at 0.3 A measurements**

Therefore, for small currents it is possible to easily extract information pertaining to both current magnitude and temperature at the sensor head. However, difficulties arise when larger currents are measured. In the previous section in Figure 10-6 to Figure 10-10 it was discovered that the sensor is less sensitive to the positive part of the current than the negative part. Figure 10-11 illustrated the impact that this has on the relationship between peak-to-peak wavelength and applied current at 18.5˚C. Not only does this effect have an impact on the current measurement, it also distorts the temperature measurement. This impact can best be illustrated by looking in more detail at the experimental data discussed in the previous section.

Looking again at the sensor output at 0.3, 0.6, and 1.0 A at 18.5˚C, only this time plotting the sensor optical output along with the quiescent wavelength and average wavelength, the affect on the temperature measurement becomes more apparent.

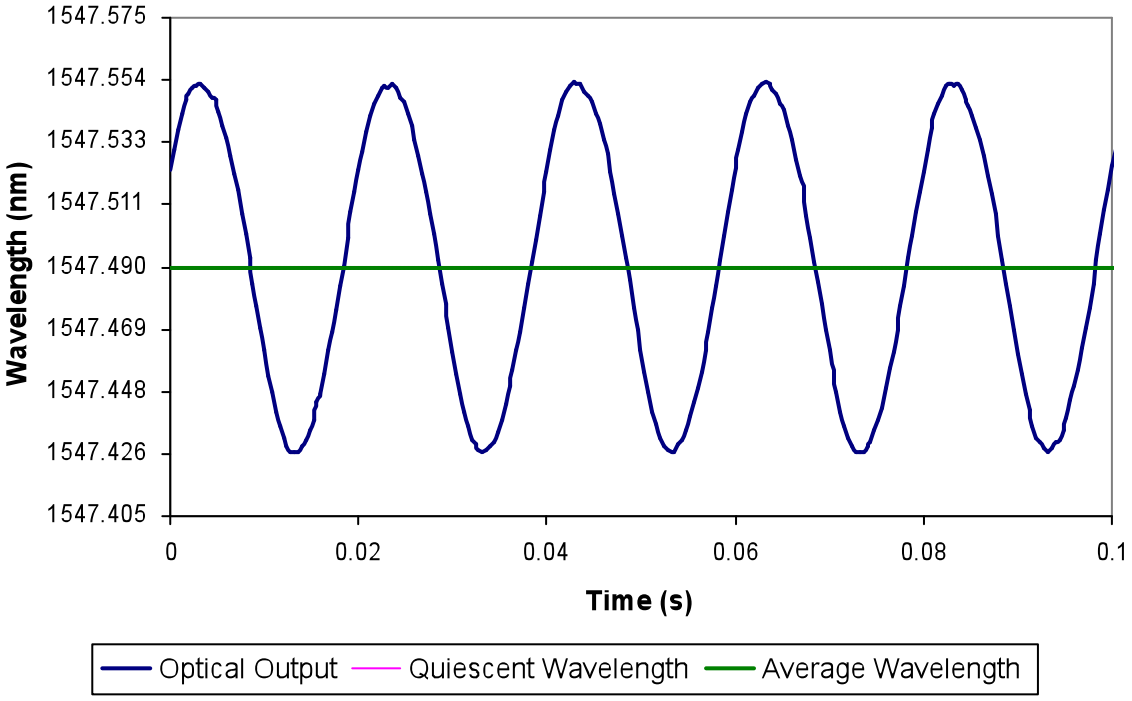


**Figure 10-18: Sensor optical output for 0.3 A at 18.5°C**

Figure 10-18 shows the sensor's optical output at 0.3 A. At this current rate, it can be seen that the average wavelength and the quiescent wavelength have the same value. Therefore at this current rate, the quiescent point, and thus the temperature at the sensor head, can be easily determined by calculating the average wavelength in a single period.

However, difficulties arise when larger currents are measured. In Figure 10-19 and Figure 10-20 the sensor's output at 0.6 A and 1.0 A are plotted along with the average wavelength and quiescent wavelength.

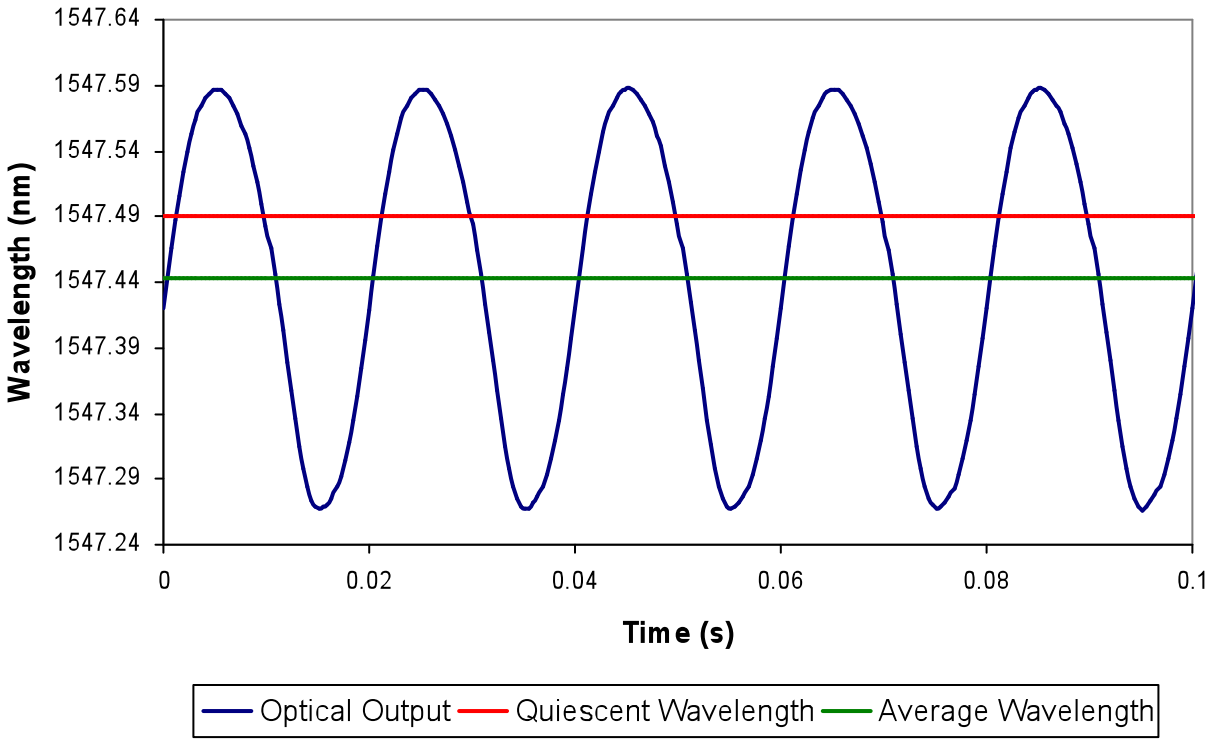


**Figure 10-19: Sensor output for 0.6 A at 18.5˚C**

As discussed earlier, at these higher current levels the sensor is less sensitive to the positive part of the current than the negative. Not only does this impact upon the current measurement by changing the peak-to-peak magnitude, it also distorts the temperature measurement, as the average wavelength of a period no longer coincides with the quiescent point of the sensor.

For 0.6 A (zero-to-peak), as shown in Figure 10-19 above, the quiescent point is located at 1547.49 nm because the experiment was conducted at 18.5˚C. However, unlike the graph for 0.3 A, at this higher current level the average wavelength no longer coincides with the quiescent wavelength. The average wavelength is now approximately 0.05 nm smaller than the quiescent wavelength at 1547.44 nm.

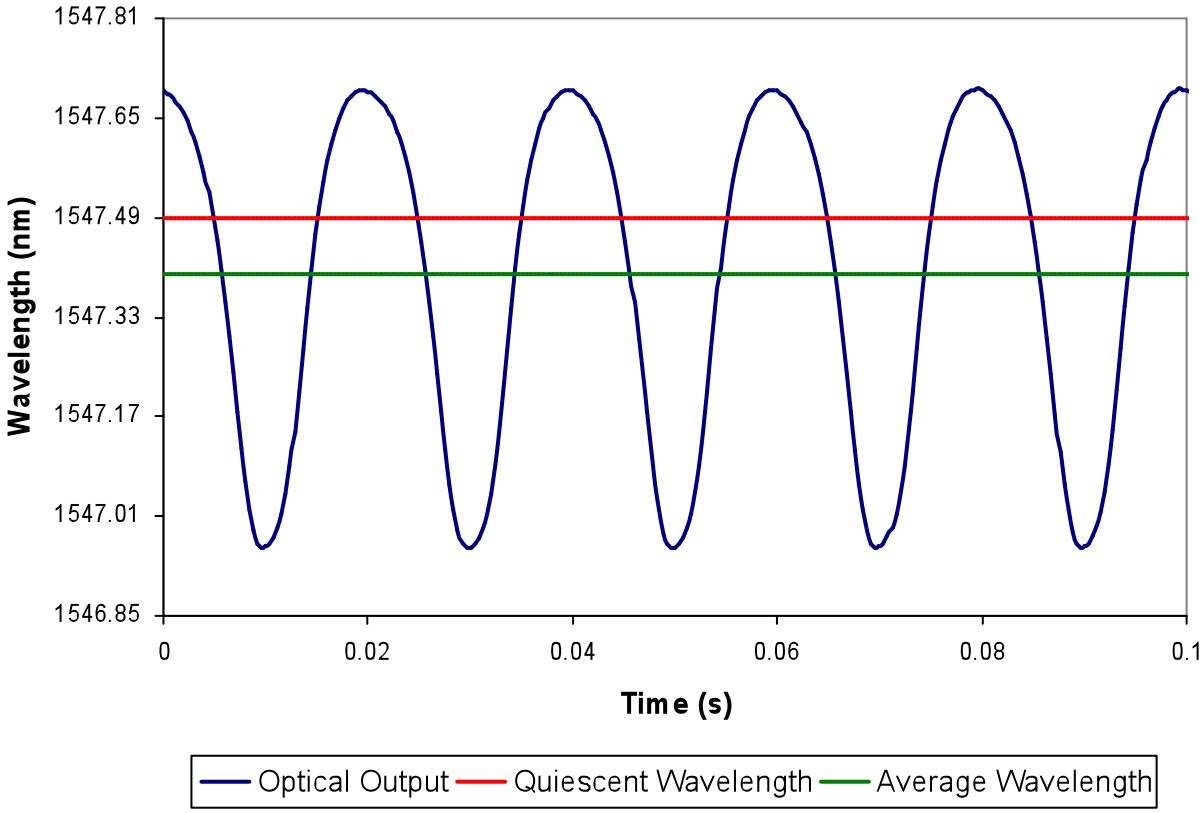


**Figure 10-20: Sensor output for 1.0 A at 18.5˚C**

The difference between the quiescent wavelength and the average wavelength at 1.0 A is even greater. While the quiescent wavelength remains the same at 1547.49 nm, the average wavelength is 1547.40 nm, 0.04 nm lower than at 0.6 A.

This demonstrates that, averaging the sensor output per period alone is not an accurate enough method of determining the quiescent point of the sensor and thus the temperature at the sensor head for the whole range of currents that the sensor is capable of measuring.

While the relationship between temperature and average wavelength, as shown in Figure 10-16 and 10-16, is only applicable at 0.3 A, a linear relationship between the two also exists at other current levels. At these higher current rates, the sensor's

output response also shifts further up the wavelength axis with increasing temperature.

The relationship between temperature and average wavelength at 0.6 A and 1.0 A is plotted in Figure 10-21 along with the previous results for 0.3 A. For all three current measurements this relationship can be seen to be linear with $\Delta\lambda/\Delta T$ equal to 2.76 nm/100°C, 2.78 nm/100°C and 2.86 nm/100°C respectively. A linear relationship between temperature and average wavelengths exists at all current levels within the sensor's range of 0.1 to 1.0 A.

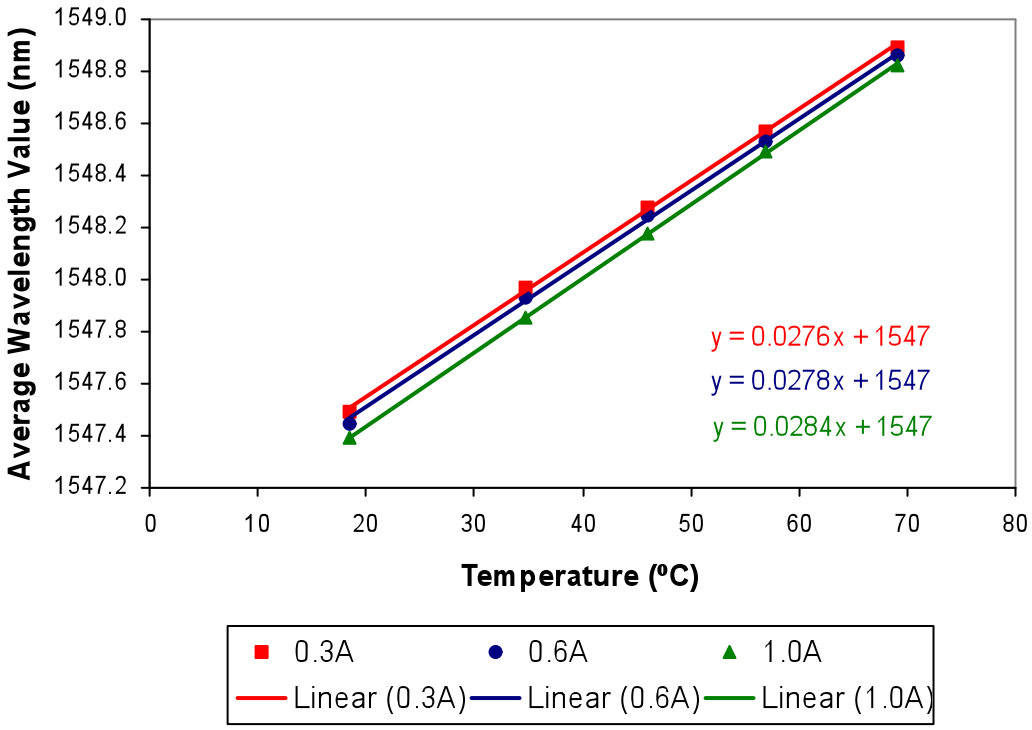


**Figure 10-21: Relationship between temperature and wavelength for 0.3 A, 0.6A and 1.0A measurements**

Furthermore, there is a temperature dependent relationship between the average wavelength, as determined by the interrogation system, and the applied current. This relationship can be clearly seen in Figure 10-22.

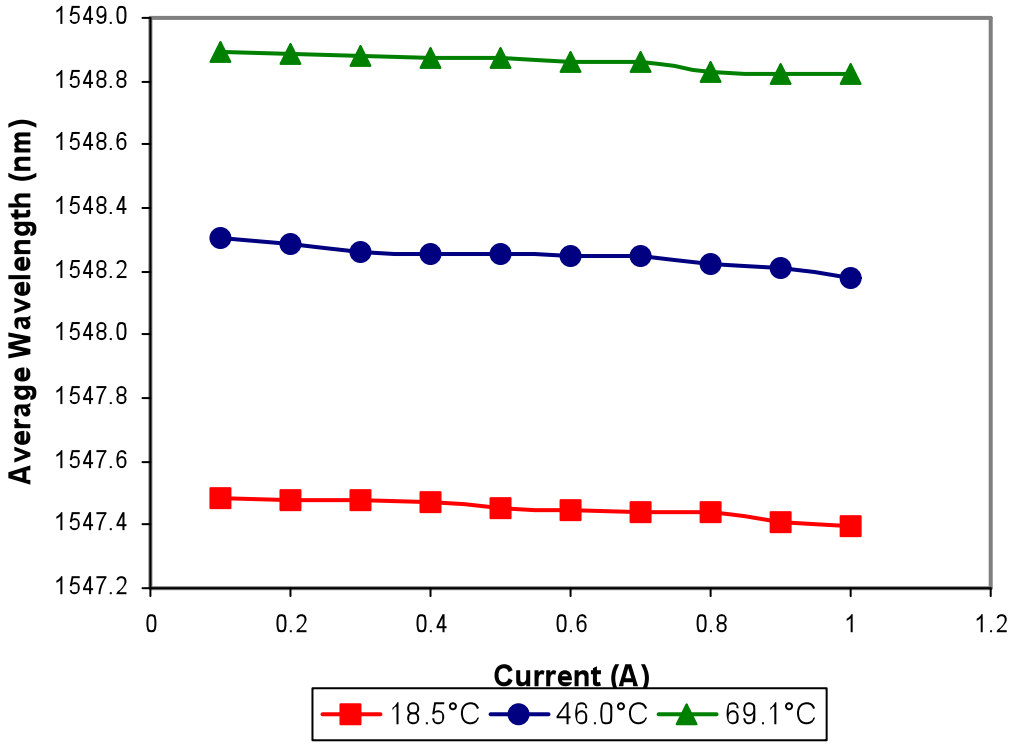


**Figure 10-22: Relationship between average wavelength and applied current**

In addition to the relationship between temperature and average wavelength, the sensor exhibits a temperature dependence of its instantaneous signal amplitude, as depicted in Figure 10-12.

Figure 10-23 shows a hysteresis loop for a 0.1 A (zero-to-peak) input plotted over 10 cycles; the hysteresis is inherent in the sensor design.

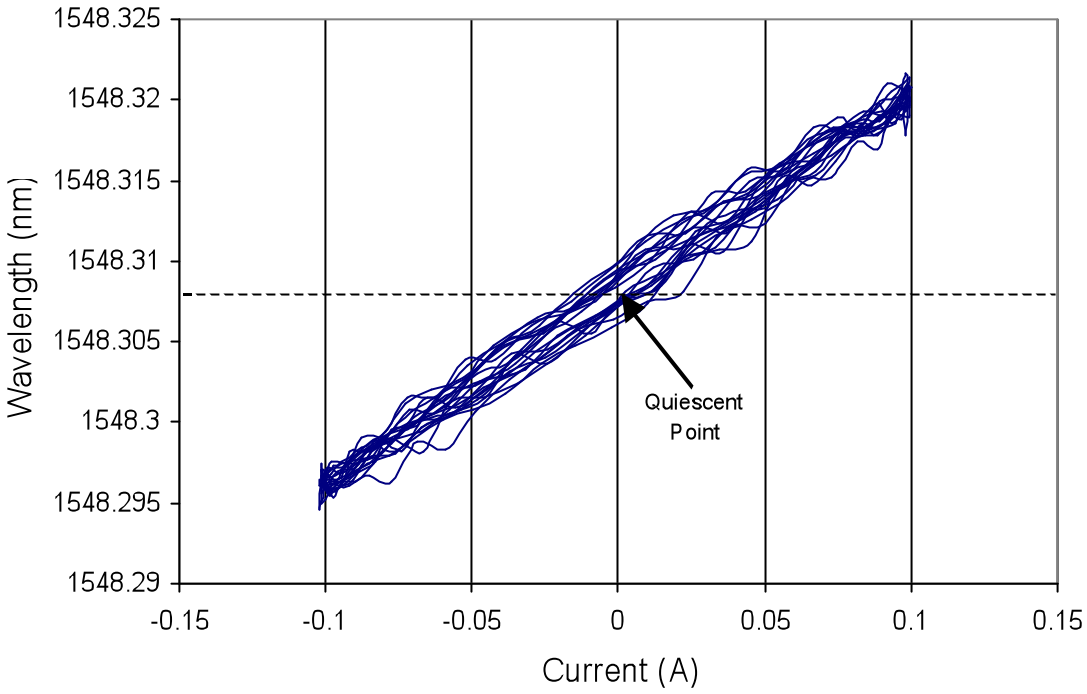


**Figure 10-23: Hysteresis loop for current measurement at 0.1 A**

It can be seen that at low current levels the magnitude of the positive and negative half of the waveform are still very similar. However, there is high level of noise in the signal.

Figure 10-24 shows the hysteresis loops for three current measurements, 0.3 A, 0.6 A and 1 A (zero-to-peak), taken at 18.5°C superimposed upon each other. The quiescent points are the same in each case due to the similar temperatures.

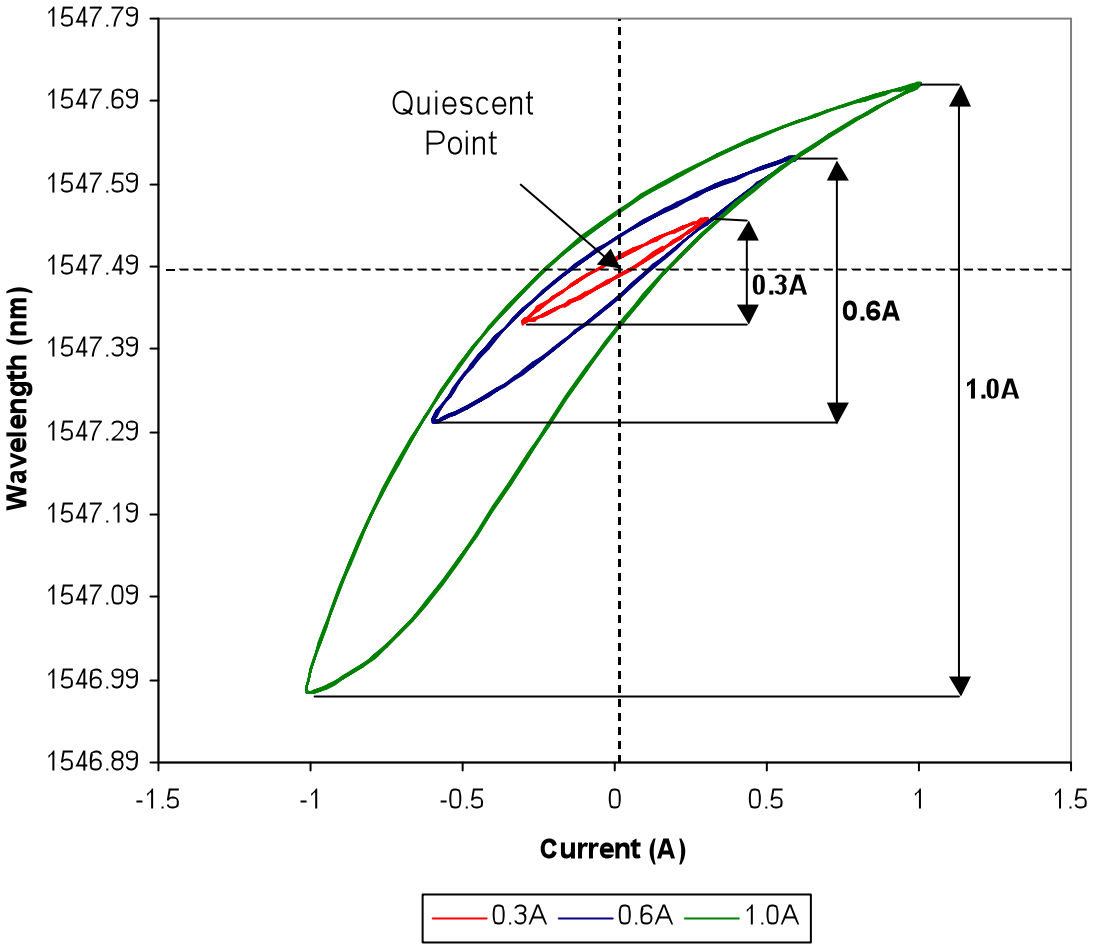


**Figure 10-24: Hysteresis loop for 0.3 A, 0.6 A and 1.0 A current measurement at 18.5˚C**

The difference in magnitudes between the positive and negative halves of the waveform is clearly in evidence, but so too is the nonlinear relationship between applied current and peak-to-peak wavelength. This is due to the shape of the magnetostrictive characteristic curve shown in Figure 5-2. This graph represents the left hand side of the butterfly hysteresis loop illustrated in Figure 6-2. Due to the applied magnetic bias to the sensor as illustrated in Figure 6-3, the sensor is capable of producing both positive and negative strains and thus operates on only one side of the butterfly loop. This enables the sensor to operate in the desired manner and produce an output single at 50 Hz.

It can also be seen from Figure 10-24 that by introducing a magnetic bias to the sensor, and thus moving the operating point, the width of the hysteresis loop is greater for the negative part than the positive part of the signal.

## 10.4 Recovery of Current and Temperature

From the sensor output signal, the two variables that can be derived are the peak-to-peak wavelength and the average wavelength. In this section it will be shown that by using these variables, current and temperature can be measured at the sensor head.

In the previous section the following relationships were found to be applicable to the sensor output signal:

- A relationship between the peak-to-peak magnitude of the sensor output signal and the applied current to the coil. This relationship was shown to be temperature dependent.
- A relationship between average wavelength and temperature at the sensor head. This relationship was shown to be current dependent.

Since neither of the relationships are fixed; the first temperature dependent and the second current dependent, they are not sufficient to derive both measurements from the sensor output signal.

However, the uncertainty in both measurements can be eliminated using the relationship between the average and peak-to-peak wavelength outputs. This relationship is plotted over the current range 0.1 to 1.0 A and temperature range 18.5 – 69.1˚C in Figure 10-25.

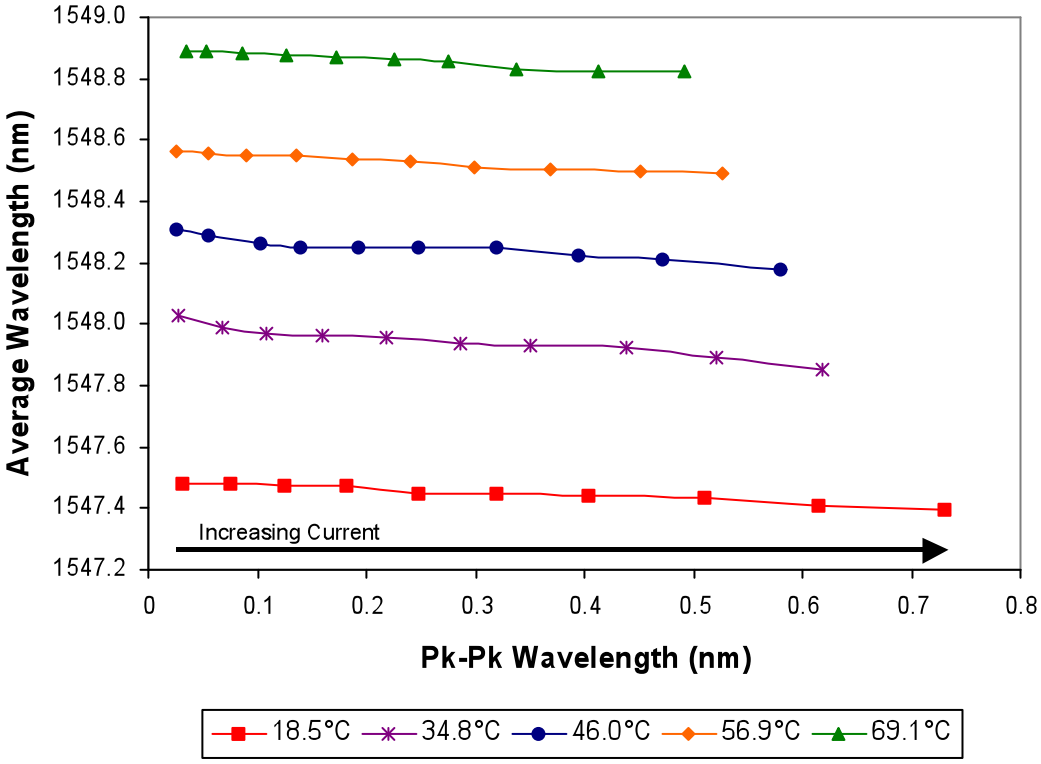


**Figure 10-25: Relationship between average and peak-to-peak wavelengths**

As can be seen, for any given peak-to-peak and average wavelength combination there is only one resulting current and temperature combination. Thus both current and temperature can be recovered through measurement of peak-to-peak and average wavelengths.

The data obtained from the experiments over the current range 0.1 to 1.0 A (zero-to-peak) in increments of 0.1 A and the temperature data obtained at 18.5, 34.8, 46.0, 56.9 and 69.1˚C was used to compute general linear models using the glm() function in the statistical package R, specified by giving a symbolic description of the linear predictor and a description of the error distribution statistics.. R is a programming language and free software environment for statistical computing and graphics [1].

The package generated the following two formulas:

$$\text{Current} = 0.11369 * \lambda_{Av} + 1.56114 * \lambda_{Pk\text{-}Pk} - 175.87547 \quad (17)$$

$$\text{Temperature} = 36.486 * \lambda_{Av} + 6.288 * \lambda_{Pk\text{-}Pk} - 56444 \quad (18)$$

Where

$\lambda_{Av}$ = Average wavelength

$\lambda_{Pk\text{-}Pk}$ = Peak-to-peak wavelength

Using these equations, current and temperature at the sensor head can be recovered through measurement of peak-to-peak and average wavelengths. The experimental data obtained from the experiments described in this section were entered into R. The generated output over the complete experimental range can be seen in Appendix D. The outputs for known input currents 0.3, 0.6 and 1.0A at 18.5, 46.0 and 69.1 ˚C are shown in Table 4.

| **Inputs** | | **Computed Values** | | | |
|---|---|---|---|---|---|
| Current (A) | Temp. (˚C) | Current (A) | Error (%) | Temp. (˚C) | Error (%) |
| 0.3 | 18.5 | 0.252 | -19.05 | 18.032 | -2.59 |
| 0.6 | 18.5 | 0.553 | -8.50 | 18.199 | -1.65 |
| 1.0 | 18.5 | 1.187 | 18.70 | 18.771 | 1.46 |
| 0.3 | 46.0 | 0.306 | 2.00 | 46.492 | 1.07 |
| 0.6 | 46.0 | 0.532 | -12.78 | 46.972 | 2.11 |
| 1.0 | 46.0 | 1.043 | 4.30 | 46.542 | 1.18 |
| 0.3 | 69.1 | 0.353 | 17.66 | 69.092 | -0.01 |
| 0.6 | 69.1 | 0.566 | -6.01 | 69.157 | 0.08 |
| 1.0 | 69.1 | 0.977 | -2.35 | 69.480 | 0.55 |

**Table 4: Computed current and temperature values and error percentages**

As can be seen, at 0.3 A the computed values of current were 0.252, 0.306 and 0.353 A at 18.5, 46.0 and 69.1˚C respectively. At 0.6 A they were 0.553, 0.532 and 0.566 A at 18.5, 46.0 and 69.1 ˚C respectively. While at 1.0 A the values were 1.187, 1.043 and 0.977 A.

The table also shows the computed temperature measurements at 0.3, 0.6 and 1.0 A respectively. At 18.5 ˚C the computed values of temperature were 18.032, 18.199 and 18.771˚C. At 46.0 ˚C they were 46.492, 46.972 and 46.542˚C. While at 69.1 ˚C they were 69.092, 69.157 and 69.480 ˚C.

Over the entire experimental data range, the deviance for current is never more than +0.187 A or -0.068 A. For temperature it is never more than +2.79˚C or -0.84˚C. The maximum error percentages were found to be +18.70% and -19.05% for current measurements and +2.11% and -2.59% for temperature measurements.

Equations (15) and (16) could be utilised in a computation routine, implemented in LabVIEW, allowing the process to take place on-line. Thus it could be easily incorporated into the existing data acquisition software.

The relationships outlined in this section are based on the sensor conditions as described within this thesis: with a magnetic bias of 40 kA/m and no applied prestress. The process would require to be repeated if either the magnetic bias point was altered or if a known prestress was applied to the sensor.

For more information on R the reader is referred to [1], [2].

## 10.5 Chapter References

[1] Hornick, K., "The R FAQ," 2010, ISBN: 3-900051-08-9, www.cran.r-project/doc/FAQ/R-FAQ.html

[2] The R Project for Statistical Computing website – www.r-project.org

# 11 Conclusions and Future Work

While this research project has successfully demonstrated the concept of simultaneously measuring low AC currents and temperature using a hybrid optical fibre sensor utilising a single FBG, so too has it uncovered many new areas of research which will require to be conducted before such a sensor can successfully be used to monitor an ESP or similar electrical equipment at extended step-out distances.

In this chapter the author draws conclusions concerning the research undertaken and its contributions to the field of OCSs. Areas of future work are also suggested as a means of taking the research forward to the ultimate goal of producing a sensor reliable and robust enough to eventually be integrated into an ESP system.

## 11.1 Conclusions

This thesis describes a sensor design and processing technique capable of simultaneously measuring ac current and temperature. The measurement of currents from 0.1 A to 1.0 A (zero-to-peak) at temperatures from approximately 18ºC to 70ºC have been successfully demonstrated.

The range of currents and temperatures in this laboratory demonstration were chosen in order to prove the sensor concept. The experimental range could be extended to achieve the desired sensor measurement range. Furthermore, the increments could be reduced in order to facilitate the required accuracy for the sensor.

The sensitivity and range of the sensor is dependent on the design of the coil. A greater number of turns will allow the sensor to measure smaller AC currents more accurately; the range however, will be smaller. The sensor could also be used without a coil to measure the large AC currents associated with ESPs. The maximum current that the sensor can measure is also dependent on the value of the sensor's saturation magnetostriction. The sensor does not facilitate the measurement of DC currents. This is because a DC current would offset the quiescent point of the sensor in a similar way to an increase in temperature.

The maximum temperature that the sensor is capable of measuring is dependent on the design of the housing and the materials used to construct the sensor. The type II FBG used in the sensor construction can operate up to 300°C without loosing its reflective properties due to grating "washing out". The epoxy used to bond the FBG to the magnetostrictive material is required to survive at high temperatures; Epotek 353ND is designed for operation of up to 300°C. Also the Curie point of the magnetostrictive material is 380~420°C. Therefore the sensor was designed to be capable of operating in the high temperatures of up to 150°C of ESPs. The maximum temperature the sensor was exposed to during these experiments was 100°C, after which it continued to operate normally.

The nonlinear effects introduced by the magnetostrictive material have been identified and a method for compensating these effects have been proposed and demonstrated over the experimental range. Various mathematical models of magnetostrictive hysteresis were preliminarily studied for the purpose of correcting the sensor output signal. They were found to be overly complicated for this application. Through the experiments conducted as part of this research, relationships were found that could facilitate the desired degree of correction through the use of general linear model statistical computation. Whilst the execution time and the accuracy would not necessarily be worse than if the mathematical models were implemented.

In summary then, the main contributions of the work described in this thesis include:

- The design and construction of a prototype current and temperature sensor.
- Laboratory demonstration of the sensor's capability to measure AC current up to 1 A (zero-to-peak) (2 A peak-to-peak) while simultaneously measuring temperature up to 70°C.
- Demonstration of a sensor capable of measuring current with an accuracy of +18.70% and -19.05%.
- Demonstration of a sensor capable of measuring temperature with an accuracy of +2.11% and -2.59%.

- Preliminary research into possible methods for more accurate determination of the contribution of the sensor's inherent hysteresis and nonlinearities from other sources on the sensor output, in order to aid with further research projects.
- The design and construction of a sensor housing which can facilitate the future application of a prestress, theoretically up to 65 MPa. For use in further research into the effects of prestress on the sensor characteristics.
- The compilation and demonstration of a signal processing technique based on general linear model statistical computation as a possible method of correcting for the sensor's nonlinearities.

## 11.2 Future Work

The sensor concept has been proven in the laboratory. However, further research is required before the sensor can be successfully used to monitor ESPs. The research and future work identified in this section are areas which, in the Author's opinion, will prove to be particularly beneficial in progressing the sensor package.

Therefore the proposed sensor should be evaluated experimentally over a wider range of currents and temperatures. These experiments should be conducted at smaller more regular increments using a set-up which allows the experiments to be more easily controlled and repeated. The data obtained from these experiments should be used to implement the signal processing technique, described in this thesis, over a wider range and greater resolution.

In addition to implementing the signal processing technique over a wider range and greater resolution, further research could be conducted into the behaviour of the magnetostrictive material.

Another area of further research concerns the sensor design in order to improve the sensor operation whilst prestress is applied. This stress may not necessarily be as large as the 65 MPa as the mathematical theory suggests since even a much smaller prestress would ensure that the magnetostrictive material would always return to a known "rest" state, thus making the process more repeatable.

At the time of the sensor design and construction, Terfenol-DH was not yet commercially available. Terfenol-DH has been shown in the literature to have lower hysteresis with only slightly lower magnetostriction. Therefore, it would be interesting to explore how this material could be used in a similar sensor, in order to determine if the resulting hysteresis would be significantly less than in the current design.

The sensor has been successfully demonstrated in the laboratory. However in its final location, on an ESP, the sensor will be subject to magnetic cross-talk from adjacent phases, pressure, vibration and stress, and will be located tens of kilometres from the monitoring equipment. Further research is required in order to determine if the sensor is adversely affected by these environmental factors. Any deterioration in the signal quality and accuracy due to these effects should be quantified and the errors associated with them determined. Methods for active compensation of the above factors using signal processing techniques should also be proposed and implemented.

# Appendix A

First of all it was necessary to determine the change in length that would be experience by the magnetostrictive material used in the sensor when placed under a 65 MPa prestress:

Young's Modulus, E for the sensor material falls into the range $(2.6 \sim 3.5)\times 10^{10}$ N/m2

Maximum compressive prestress applied to the material, σ65 is 65 MPa

$$E = \frac{\sigma}{\varepsilon}$$

$$\varepsilon_{65} = \frac{65\times 10^{6}}{(2.6 \sim 3.5)\times 10^{10}}$$

$$\varepsilon_{65} = 1857 \sim 2500\mu\varepsilon$$

$$\varepsilon = \frac{\Delta L}{L}$$

For $\varepsilon = 1857\mu\varepsilon$ :

$$\Delta L = 1857\times 10^{-6}\times 20\times 10^{-3}$$

$$\Delta L = 0.037mm$$

For $\varepsilon = 2500\mu\varepsilon$ :

$$\Delta L = 2500\times 10^{-6}\times 20\times 10^{-3}$$

$$\Delta L = 0.05mm$$

Therefore the change in length experienced by the sensor if placed under a 65 MPa prestress would be in the range $\Delta L = 0.04 - 0.05mm$

The following calculations were conducted in order to determine the necessary length of polycarbonate required to act as a spring in the prestress housing:

Maximum compressive strength of polycarbonate, $\varepsilon_{max}$

$\varepsilon_{\max} = 12000\,psi$

$1psi = 6895\ \text{N/m}^2$

$\varepsilon_{\max} = 12000 \times 6895 N/m^2 (Pa)$

$\varepsilon_{\max} = 83 MPa$

Young's Modulus, E

$E = 320{,}000\,psi$

$E = (320{,}000 \times 6895) N/m^2$

$E = 2{,}206{,}400{,}000 N/m^2 (Pa)$

$E = 2{,}206 MPa$

Maximum compressive strain, $\varepsilon_{max}$

$= \dfrac{82 \times 10^6}{2206 \times 10^6}$

$= \underline{0.37 m\varepsilon}$

Expected change in length, $\Delta L$ due to compression at maximum compressive strength for a range of polycarbonate lengths:

| L (mm) | ΔL (mm) |
|---|---|
| 20 | 0.74 |
| 25 | 0.93 |
| 30 | 1.11 |
| 35 | 1.30 |
| 40 | 1.48 |

65 MPa

$$\varepsilon_{65} = \frac{\sigma}{E}$$

$$\varepsilon_{65} = \frac{65 \times 10^6}{2206 \times 10^6}$$

$$\varepsilon_{65} = 29m\varepsilon$$

$$\varepsilon = \frac{\Delta L}{L}$$

| L (mm) | ΔL (mm) |
|---|---|
| 20 | 0.58 |
| 25 | 0.73 |
| 30 | 0.87 |
| 35 | 1.02 |
| 40 | 1.16 |

If the prestress housing was designed with a 35 mm long piece of polycarbonate to act as a spring for the sensor which comprises a 20 mm long piece of magnetostrictive material, the total length $\Delta L_{tot}$ experience on application of a 65 MPa prestress:

$$\Delta L_{tot} = 1.015 + 0.04$$
$$\Delta L_{tot} = 1.055mm$$

For a 35 mm length of polycarbonate:

Since the maximum compressive strength of polycarbonate, as calculated earlier, is $\varepsilon_{\max} = 83MPa$ which equates to:

$$\varepsilon_{\max} = \frac{\Delta L}{L}$$
$$\Delta L = 1.295mm$$

for a 35 mm length.

There is still $\Delta l = 1.295 - 1.055 = 0.24mm$ available to accommodate the elongation of the sensor when in operation.

# Appendix B

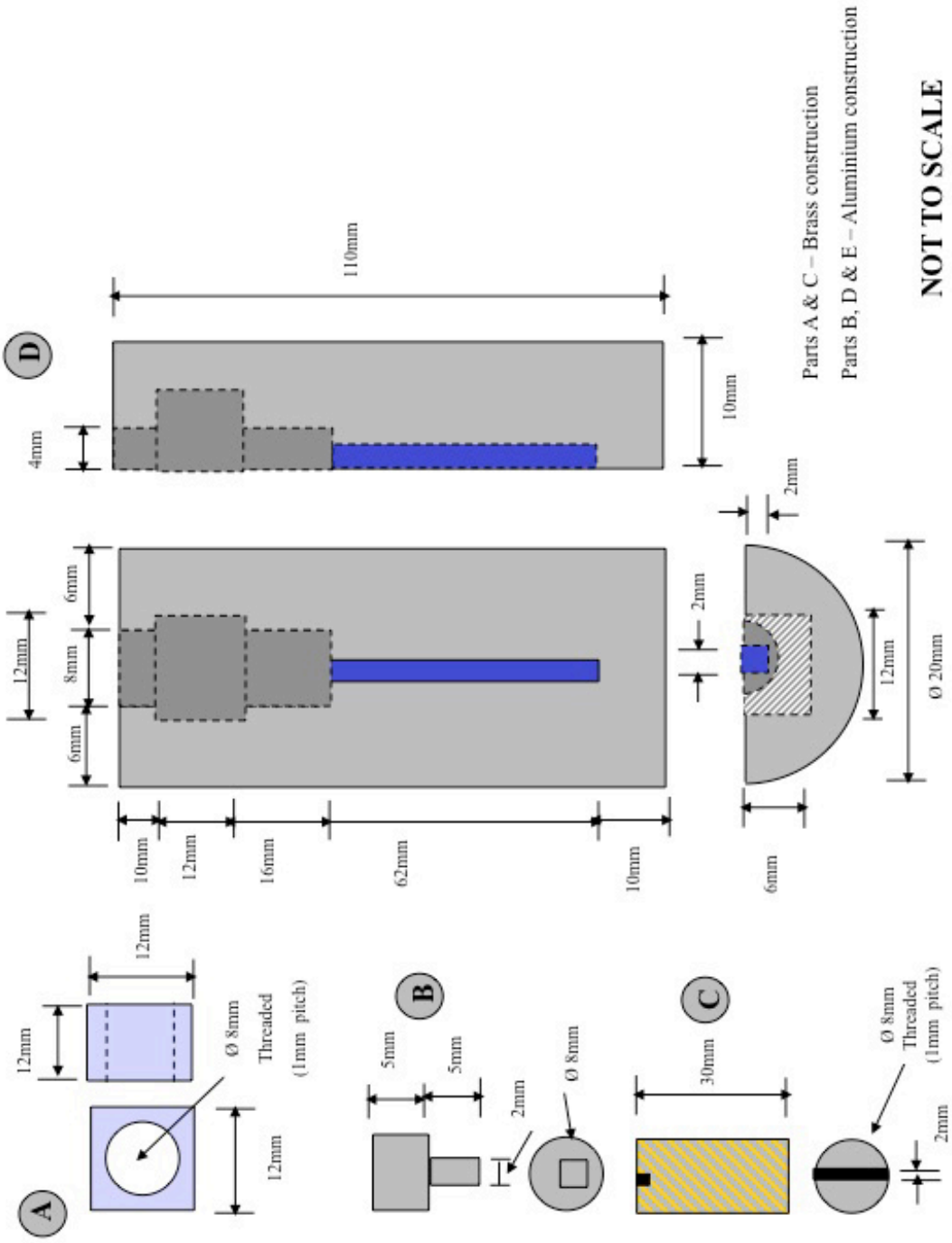
D
110mm
4mm
10mm
Parts A & C – Brass construction
Parts B, D & E – Aluminium construction
NOT TO SCALE
2mm
6mm
8mm
6mm
12mm
2mm
12mm
Ø 20mm
10mm
12mm
16mm
62mm
10mm
6mm
A
12mm
12mm
Ø 8mm
Threaded
(1mm pitch)
12mm
B
5mm
5mm
2mm
Ø 8mm
C
30mm
Ø 8mm
Threaded
(1mm pitch)
2mm

E

TOP SECTION

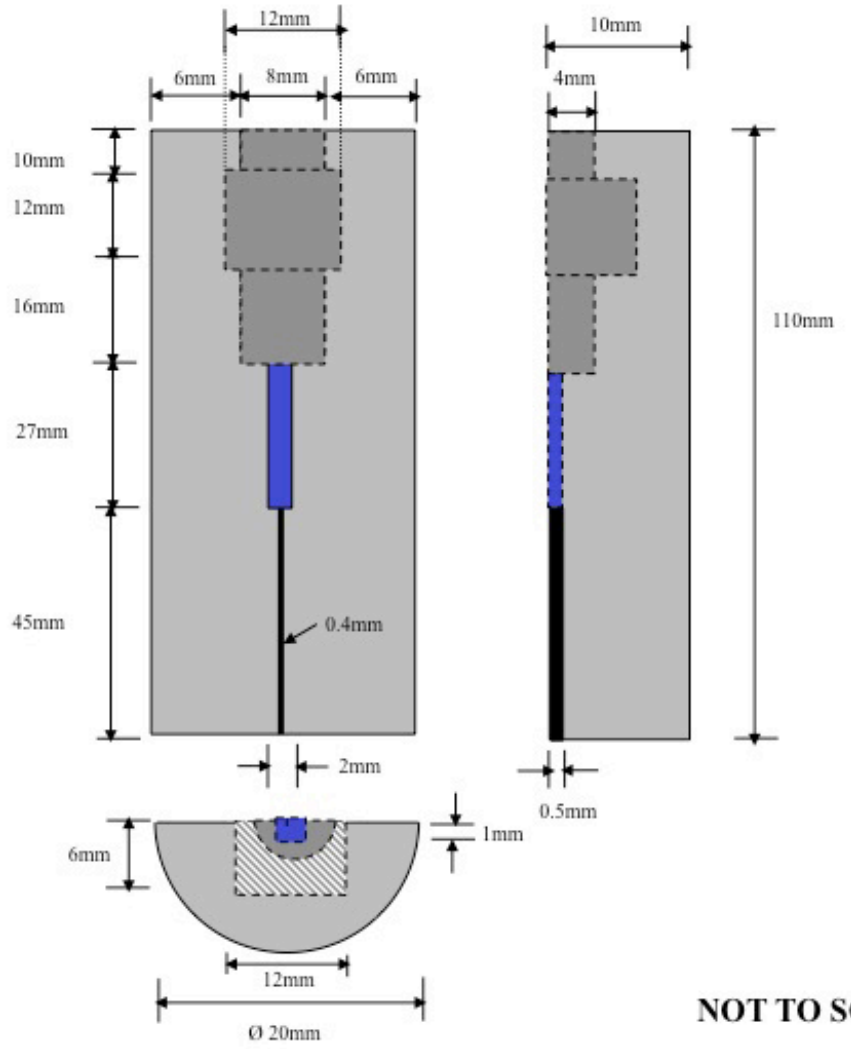


NOT TO SCALE

TOP SECTION
10mm
6mm
4mm
27mm
45mm
0.5mm
E
BOTTOM SECTION
D
10mm
12mm
16mm
62mm
10mm
110mm
2mm
4mm
6mm
10mm
SIDE VIEW
NOT TO SCALE

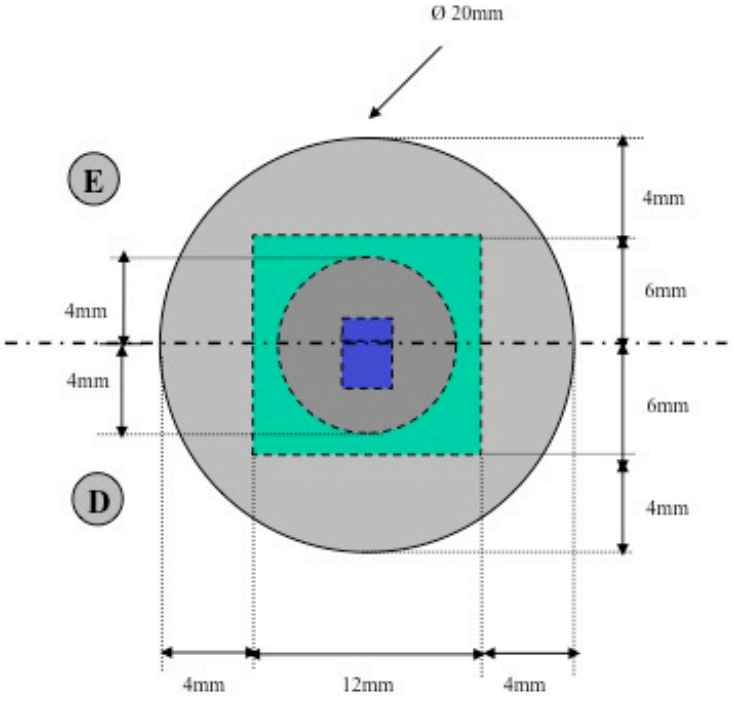


**FRONT VIEW**

**NOT TO SCALE**

NOT TO SCALE
B
Ø 8mm
2mm
3mm
2mm
3mm
5mm
5mm
2mm
2mm
2mm
4mm

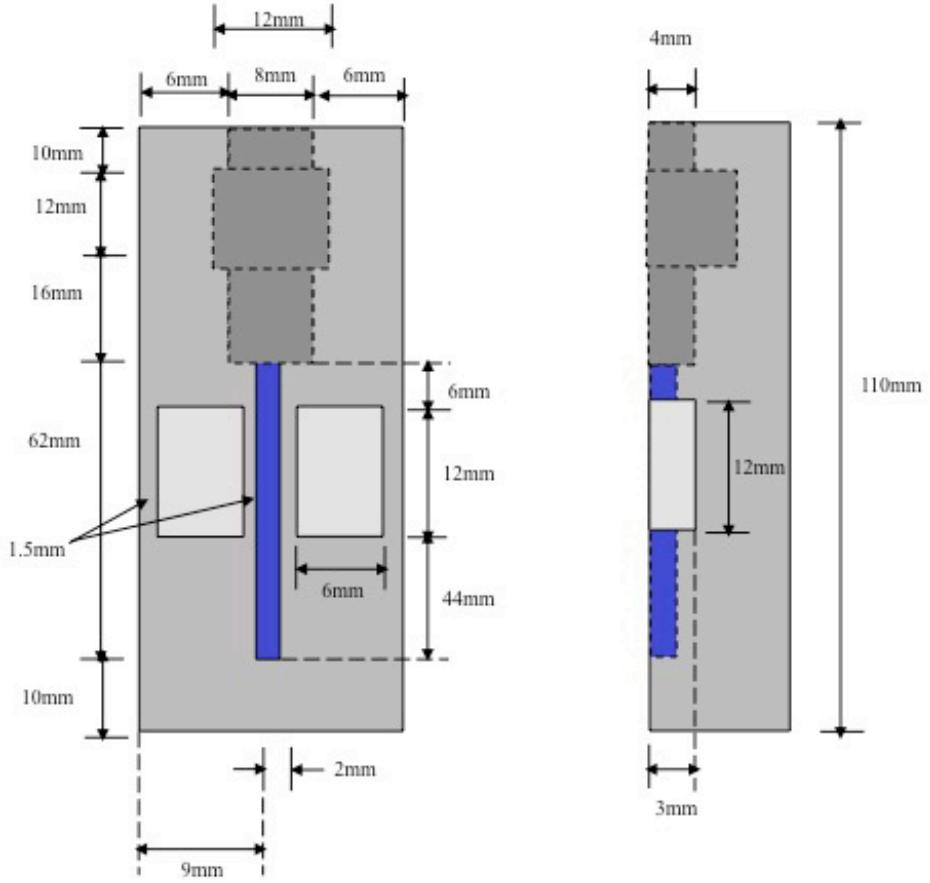
12mm
6mm
8mm
6mm
10mm
12mm
16mm
62mm
1.5mm
10mm
6mm
12mm
44mm
6mm
2mm
9mm
4mm
110mm
12mm
3mm

**NOT TO SCALE**

# Appendix C

| | | |
|---|---|---|
| Magnetic field: | | $H := 80000\frac{A}{m}$ |
| Current: | | $I := 5A$ |
| Wire diameter: | | $d := 1mm$ |
| Outer tube diameter: | | $a := 2.5cm$ |
| Tube length: | | $l := 8cm$ |
| Wire resistance per km: | | $R\_w := 22.63\frac{\Omega}{km}$ |
| Number of turns: | $n := \frac{H \cdot l}{I}$ | $n = 1280$ |
| Number of turns per layer: | $n\_w := \frac{l}{d}$ | $n\_w = 80$ |
| Number of layers: | $n\_l := \frac{n}{n\_w}$ | $n\_l = 16$ |
| Wire length: | $w\_l := 500mm + \sum_{i=1}^{n\_l} n\_w \cdot \pi \cdot (a + i \cdot d)$ | $w\_l = 135.21\,m$ |
| Wire resistance: | $R := R\_w \cdot w\_l$ | $R = 3.06\,\Omega$ |
| Average diameter: | $a\_d := \frac{2 \cdot n\_l \cdot d + 2a}{2}$ | $a\_d = 4.1\,cm$ |
| Radial thickness of the winding: | $c := n\_l \cdot d$ | $c = 1.6\,cm$ |
| Inductance: | $L := \frac{0.008\frac{mH}{m} \cdot a\_d^2 \cdot n^2}{3 \cdot a\_d + 9 \cdot l + 10 \cdot c}$ | $L = 21.97\,mH$ |
| Frequency: | $f := 50Hz$ | |
| Reactance: | $X := 2 \cdot \pi \cdot f \cdot L$ | $X = 6.9\,\Omega$ |
| Impedance: | $Z := \sqrt{R^2 + X^2}$ | $Z = 7.55\,\Omega$ |
| Voltage drop: | $\Delta U := I \cdot Z$ | $\Delta U = 37.75\,V$ |
| Wire mass: | $Mass := 8920\frac{kg}{m^3} \cdot \frac{\pi \cdot d^2 \cdot w\_l}{4}$ | $Mass = 0.95\,kg$ |

# Appendix D

| $\lambda_{Pk-Pk}$ (nm) | $\lambda_{Av}$ (nm) | I (A) | T (˚C) | Est. I (A) | I Error (A) | Est. T (˚C) | T Error (˚C) |
|---|---|---|---|---|---|---|---|
| 0.031 | 1547.483 | 0.1 | 18.5 | 0.106 | 0.006 | 17.660 | -0.840 |
| 0.075 | 1547.479 | 0.2 | 18.5 | 0.175 | -0.025 | 17.79 | -0.710 |
| 0.125 | 1547.477 | 0.3 | 18.5 | 0.252 | -0.048 | 18.032 | -0.468 |
| 0.181 | 1547.474 | 0.4 | 18.5 | 0.339 | -0.061 | 18.274 | -0.225 |
| 0.248 | 1547.451 | 0.5 | 18.5 | 0.441 | -0.059 | 17.857 | -0.643 |
| 0.320 | 1547.448 | 0.6 | 18.5 | 0.553 | -0.047 | 18.200 | -0.300 |
| 0.404 | 1547.441 | 0.7 | 18.5 | 0.684 | -0.016 | 18.473 | -0.027 |
| 0.511 | 1547.438 | 0.8 | 18.5 | 0.850 | 0.050 | 19.036 | 0.536 |
| 0.614 | 1547.406 | 0.9 | 18.5 | 1.008 | 0.108 | 18.516 | 0.016 |
| 0.730 | 1547.393 | 1.0 | 18.5 | 1.187 | 0.187 | 18.771 | 0.271 |
| 0.027 | 1548.030 | 0.1 | 34.8 | 0.162 | 0.062 | 37.592 | 2.792 |
| 0.067 | 1547.990 | 0.2 | 34.8 | 0.220 | 0.020 | 36.384 | 1.584 |
| 0.109 | 1547.970 | 0.3 | 34.8 | 0.283 | -0.017 | 35.919 | 1.118 |
| 0.159 | 1547.962 | 0.4 | 34.8 | 0.361 | -0.039 | 35.941 | 1.141 |
| 0.218 | 1547.957 | 0.5 | 34.8 | 0.452 | -0.048 | 36.130 | 1.329 |
| 0.287 | 1547.934 | 0.6 | 34.8 | 0.557 | -0.043 | 35.725 | 0.924 |
| 0.350 | 1547.930 | 0.7 | 34.8 | 0.655 | -0.045 | 35.975 | 1.174 |
| 0.439 | 1547.927 | 0.8 | 34.8 | 0.794 | -0.006 | 36.425 | 1.624 |
| 0.521 | 1547.893 | 0.9 | 34.8 | 0.918 | 0.018 | 35.700 | 0.900 |
| 0.619 | 1547.852 | 1.0 | 34.8 | 1.066 | 0.066 | 34.820 | 0.020 |
| 0.025 | 1548.307 | 0.1 | 46.0 | 0.191 | 0.091 | 47.686 | 1.686 |
| 0.055 | 1548.288 | 0.2 | 46.0 | 0.235 | 0.035 | 47.182 | 1.181 |
| 0.102 | 1548.261 | 0.3 | 46.0 | 0.306 | 0.006 | 46.492 | 0.492 |
| 0.139 | 1548.253 | 0.4 | 46.0 | 0.362 | -0.038 | 46.433 | 0.432 |
| 0.193 | 1548.252 | 0.5 | 46.0 | 0.447 | -0.053 | 46.736 | 0.736 |
| 0.248 | 1548.249 | 0.6 | 46.0 | 0.532 | -0.068 | 46.972 | 0.972 |
| 0.319 | 1548.247 | 0.7 | 46.0 | 0.643 | -0.057 | 47.346 | 1.345 |
| 0.395 | 1548.226 | 0.8 | 46.0 | 0.759 | -0.041 | 47.058 | 1.057 |
| 0.472 | 1548.212 | 0.9 | 46.0 | 0.878 | -0.022 | 47.031 | 1.030 |
| 0.580 | 1548.180 | 1.0 | 46.0 | 1.043 | 0.043 | 46.542 | 0.542 |
| 0.026 | 1548.561 | 0.1 | 56.9 | 0.221 | 0.121 | 56.960 | 0.060 |
| 0.055 | 1548.559 | 0.2 | 56.9 | 0.266 | 0.066 | 57.070 | 0.169 |
| 0.089 | 1548.549 | 0.3 | 56.9 | 0.318 | 0.018 | 56.918 | 0.018 |
| 0.136 | 1548.547 | 0.4 | 56.9 | 0.391 | -0.009 | 57.141 | 0.241 |
| 0.187 | 1548.538 | 0.5 | 56.9 | 0.470 | -0.030 | 57.133 | 0.233 |
| 0.240 | 1548.529 | 0.6 | 56.9 | 0.551 | -0.049 | 57.138 | 0.238 |
| 0.299 | 1548.513 | 0.7 | 56.9 | 0.642 | -0.058 | 56.925 | 0.025 |
| 0.369 | 1548.502 | 0.8 | 56.9 | 0.750 | -0.050 | 56.964 | 0.064 |
| 0.451 | 1548.497 | 0.9 | 56.9 | 0.877 | -0.023 | 57.297 | 0.397 |

| | | | | | | | |
|---|---|---|---|---|---|---|---|
| 0.526 | 1548.493 | 1.0 | 56.9 | 0.994 | -0.006 | 57.623 | 0.723 |
| 0.034 | 1548.891 | 0.1 | 69.1 | 0.271 | 0.171 | 69.051 | -0.049 |
| 0.054 | 1548.886 | 0.2 | 69.1 | 0.302 | 0.102 | 68.994 | -0.105 |
| 0.087 | 1548.883 | 0.3 | 69.1 | 0.353 | 0.053 | 69.092 | -0.007 |
| 0.126 | 1548.875 | 0.4 | 69.1 | 0.413 | 0.013 | 69.046 | -0.054 |
| 0.173 | 1548.872 | 0.5 | 69.1 | 0.486 | -0.014 | 69.232 | 0.131 |
| 0.225 | 1548.861 | 0.6 | 69.1 | 0.566 | -0.034 | 69.157 | 0.057 |
| 0.276 | 1548.859 | 0.7 | 69.1 | 0.645 | -0.055 | 69.405 | 0.304 |
| 0.338 | 1548.832 | 0.8 | 69.1 | 0.739 | -0.061 | 68.810 | -0.290 |
| 0.412 | 1548.825 | 0.9 | 69.1 | 0.854 | -0.046 | 69.020 | -0.080 |
| 0.491 | 1548.824 | 1.0 | 69.1 | 0.977 | -0.023 | 69.480 | 0.379 |